

**Laser manipulation of atoms
and nanofabrication**

ISBN 90-9014777-2

Laser manipulation of atoms and nanofabrication

een wetenschappelijke proeve op het gebied van
de Natuurwetenschappen, Wiskunde en Informatica

Proefschrift

ter verkrijging van de graad van doctor aan
de Katholieke Universiteit Nijmegen,
volgens besluit van het College van Decanen
in het openbaar te verdedigen op
dinsdag 19 juni 2001,
des namiddags om 3.30 uur precies

door

Erich Jurdík

geboren op 13 april 1974
te Bratislava, Tsjechoslowakije

Promotores: prof. dr. H. van Kempen
prof. dr. Th.H.M. Rasing
Co-promotor: dr. W.L. Meerts

Manuscriptcommissie:

prof. dr. D.H. Parker
dr. J.J. McClelland Electron Physics Group,
National Institute of Standards and Technology,
Gaithersburgh, Maryland, USA



Het werk beschreven in dit proefschrift maakt deel uit van het onderzoeksprogramma van de Stichting voor Fundamenteel Onderzoek der Materie (FOM) en is mede mogelijk gemaakt door financiële steun van de Nederlandse Organisatie voor Wetenschappelijk Onderzoek (NWO).

“We have a habit in writing articles published in scientific journals to make the work as finished as possible, to cover up all the tracks, to not worry about the blind alleys or describe how you had the wrong idea first, and so on. So there isn’t any place to publish, in a dignified manner, what you actually did in order to get to do the work.”

Richard Phillips Feynman, Nobel Lecture, 1966.

Preface

“Throughout much if not all of his existence, man has been motivated to build things. The very first objects built by man: weapons, shelters and tools, were certainly motivated by the need to survive. Man is not alone in this endeavor. Birds build nests. Beavers build dams. Chimpanzees build and use tools. The advance of man’s ability to build objects of increasing sophistication has enabled him to satisfy motivations beyond survival, motivations such as bettering the quality of life and expansion of knowledge. What I want to talk about today is the achievement of a milestone in man’s ability to build things. That milestone is the ability to build things using individual atoms as the building blocks; the ability to build things from the bottom up, by placing the atoms where we want them.”

Don Eigler,
From the Bottom Up: Building Things with Atoms.
In G.L. Timp, editor, *Nanotechnology*, Chap. 11, p. 425,
Springer-Verlag, Heidelberg, 1999.

The action of making small objects, consisting of several to several hundreds of atoms, is accomplished either *from the bottom up* by using individual atoms as the building blocks, or *from the top down* by manipulating macroscopic matter on the near-atomic level. The question is how big can things be made when built *from the bottom up* and how small when built *from the top down*. One is looking for new approaches to create intriguing patterns on a scale of several nanometers because existing techniques are reaching their limits. Besides the fact that developments in this branch of science are of key importance for modern technology, there are persisting fundamental problems that must be solved. And this is good because a scientist wants, most of all, to understand how the world is functioning on all its levels: from sub-atomic to the large scale of the Universe.

In this thesis I write about the past four years of my own research and development activities in this area. The goal my co-workers and I finally reached was to build an apparatus for laser-manipulated atomic deposition as an approach to *from the bottom up* nanotechnology. This technique makes use of fundamental interaction processes between atoms and photons to manipulate atoms and to place them where we want them. Laser-manipulated deposition is in its infancy and there are thus many important questions still waiting to be answered.

The journey undertaken began in an empty laboratory and finishes with a reliably working experimental facility. In Chap. 1 a brief review of nanotechnology and laser manipulation of atoms is provided. Then, concerning my own work I report on the following: modeling of atomic focusing in a laser standing wave and growth of laser-focused nanostructures (Chap. 2); design and development of the laser system and

the vacuum system (Chap. 3); and laser manipulation of an atomic beam and laser-focused nanofabrication (Chap. 4). Chromium atoms are the species used throughout this work.

What is the reason for using atom optics for nanostructure fabrication when, for example, interference lithography seems more versatile at the present time? My first answer is that laser manipulation of atoms is a clean approach and thus allows for exciting physics to be done in a clean, ultra-high vacuum environment with no need for post-processing such as chemical etching. The second answer is that laser manipulation of atoms is enjoyable by itself. And in fact this is enough for me to work on this project.

CONTENTS

Preface	vii
1 Introduction	1
1.1 Nanotechnology	1
1.2 Laser manipulation of atoms	3
1.2.1 Atom optics	3
1.2.2 Laser cooling	4
1.2.3 Laser focusing	9
1.3 Chromium	13
References	14
2 Modeling	19
2.1 Atom lens	19
2.1.1 Semiclassical model	20
2.1.2 Aberrations and channeling	24
2.1.3 Laser and atom beam parameters	27
2.1.4 Line shape	31
2.1.5 Towards realistic beams	32
2.2 Surface growth	35
2.2.1 Tamborenea-Das Sarma diffusion model	36
2.2.2 Ballistic deposition model	39
2.3 Conclusions	40
References	41
3 Apparatus	43
3.1 Outline	43
3.2 Optical part	45

3.2.1	Resonators	45
3.2.2	Single-frequency Ti:Sapphire laser	51
3.2.3	LBO-based doubling cavity	54
3.2.4	Michelson wavemeter	64
3.2.5	Absolute stabilization	70
3.3	Vacuum part	75
3.3.1	Main frame	75
3.3.2	<i>In vacuo</i> optics and manipulator	78
3.4	Conclusions	80
	References	81
4	Laser-focused atomic deposition	83
4.1	Optics for manipulation of atoms	83
4.2	Laser manipulation of chromium atoms	85
4.2.1	One-dimensional optical molasses	85
4.2.2	Channeling of atoms in a laser standing wave	91
4.3	Chromium nanostructures	92
4.3.1	Work carried out in Nijmegen	92
4.3.2	Work carried out at NIST (Gaithersburg, MD, USA)	98
4.4	Conclusions	102
	References	103
	Summary	105
	Samenvatting	107
	Dankwoord	109
	Curriculum vitae	110

Introduction

Nanotechnology, atom optics, laser cooling and trapping of atoms and laser-focused atomic deposition are all briefly reviewed here. Thereafter, the basic characteristics of chromium atoms are described. The aim of this chapter is to provide a basis for further discussion.

1.1 Nanotechnology

Nano, as inspired by the ancient Greek word “*νανος*”, meaning dwarf, stands for small or, more precisely, for one billionth ($= 10^{-9}$). While on a length-scale of several microns there would be several thousand atoms standing in a row, we would find only a few of them on a scale of several nanometers (nm). Thus, nanotechnology and nanoscience are branches of human activities devoted to the manipulation and control of matter on the near-atomic level.

About 40 years ago it seemed almost inconceivable to construct objects and devices only a few nanometers in size. Indeed, when Richard P. Feynman addressed the annual meeting of the American Physical Society in December 1959 (for a reprint of Feynman’s famous lecture, see [1]), the world of technology was still a big place with, for example, a computer occupying several rooms of a big building. However, it did not stop him from giving a visionary talk and stating: *“Ultimately, when our computers get faster and faster and more and more elaborate, we will have to make them smaller and smaller. But there is plenty of room (at the bottom) to make them smaller. There is nothing that I can see in the physical laws that says the computer elements cannot be made enormously smaller than they are now.”* Indeed, from that time on enormous advances have been made in physics and technology, pushing our dreams closer to reality.

Ultimately, it is desirable to have the ability to rapidly build any structures with atomic precision using any atomic species. In this respect, there is a great deal of progress still to be made. To date, no single approach to nanotechnology is meeting all our demands. Rather, there are a number of techniques, each of them possessing some advantages and, at the same time, having some drawbacks. For example, conventional optical lithography is diffraction limited to about 100 nm; charged particle (e.g., electron or ion) beam lithography still suffers from the serial nature of patterning and Coulomb repulsion; scanning probes, as they manipulate single atoms, are generally too slow; and self-assembled fabrication will require a better understanding to make any structure shapes one can think of. However, there are ways to overcome these obstacles. For example, optical lithography is being pushed towards the deep ultra-violet or even X-ray regions of the electromagnetic spectrum. Also, efforts to use charged particle beam or scanning probe methods for parallel patterning are being undertaken. These improvements will most likely result in massive industrial applications of the above mentioned techniques as they are thought to be a natural extension to the ones currently used in microelectronics and optoelectronics.

It is in the spirit of finding alternative tools for nanotechnology that nanofabrication via atom optics became a subject of investigation in recent years. Here, the atomic degrees of freedom (whether internal or external or even both) are controlled with nanoscale precision using external electromagnetic fields, allowing high resolution patterning of surfaces. As this approach makes use of neutral atoms, there are some advantages over existing techniques. The fundamental diffraction limit imposed on resolution can be very small for atoms due to their relatively large mass. Also, because neutral atoms are used, there are no Coulomb repulsion forces. For another thing, atom manipulation can be performed in a massively parallel way, allowing simultaneous patterning of a relatively large surface area. Furthermore, this technique offers the possibility of being used in both direct deposition or lithography regimes. In the former case, it is compatible with molecular beam epitaxy (MBE), allowing growth and subsequent investigation of nanostructures in a clean, ultra-high vacuum (UHV) environment. However, there are also some disadvantages of this method and it is worthwhile to mention at least a few of them at this point. To date, only very simple patterns have been demonstrated and only a few atomic species have been successfully manipulated. In addition, the technological infrastructure needed to carry out nanofabrication via atom optics is rather expensive, sophisticated and elaborate. An enormous effort has to be made to develop atom optics into a standard tool for nanofabrication.

For reviews on nanotechnology, see [2–5].

1.2 Laser manipulation of atoms

1.2.1 Atom optics

Atom optics refers to techniques to manipulate atomic trajectories and to exploit the wave-like properties of neutral atoms. Owing to the mathematical similarities between the Helmholtz equation of wave optics and the time independent Schrödinger equation for atoms moving in an external field $V(\mathbf{r})$ – both of them can be written in the standard form

$$[\nabla^2 + k^2(\mathbf{r})]\psi(\mathbf{r}) = 0, \quad (1.1)$$

with $\mathbf{k}(\mathbf{r})$ being the wave-vector and $\psi(\mathbf{r})$ being the wave-function – a question arises whether it is possible to construct $V(\mathbf{r})$ such that one would have an atom optical component resembling some optical counterpart. For the sake of clarity, it should be noted that there is an important physical difference between an atom and a photon. While the former has a finite mass M_a , the latter does not. This fact has important consequences in the physics of coherent phenomena and enters Eq. (1.1) via an expression for $\mathbf{k}(\mathbf{r})$. For a light wave propagating in a medium with an index of refraction $n(\mathbf{r})$ one has

$$\mathbf{k}(\mathbf{r}) = \frac{2\pi n(\mathbf{r})}{\lambda_0} \mathbf{k}^0, \quad (1.2)$$

where λ_0 is the vacuum wavelength and \mathbf{k}^0 is the unit vector pointing in the direction of the light phase gradient. In contrast, for an atom the following equation is derived

$$\mathbf{k}(\mathbf{r}) = \sqrt{\frac{2M_a}{\hbar^2} [E - V(\mathbf{r})]} \mathbf{k}^0. \quad (1.3)$$

Here, E is the total atomic energy, \hbar is Planck's constant divided by 2π and the unit vector \mathbf{k}^0 is now pointing in the direction of propagation. Formally, Eq. (1.3) can be collapsed into Eq. (1.2) by making use of the de Broglie relations and by introducing an effective index of refraction for atoms

$$n(\mathbf{r}) = \sqrt{1 - V(\mathbf{r})/E}. \quad (1.4)$$

Much of the recent work in the field of atom optics has concentrated on constructing electromagnetic fields such that the atoms could be focused, reflected, diffracted and interfered. In this way, one could manipulate atom beams in the same way as one does it with light. The dream of human kind is to have the ultimate control over matter (atoms) as it has over light. To achieve this objective, considerable work is still to be done. Some promising results have been obtained in the past. Here, we give a few examples.

As early as in 1978, the focusing of a sodium beam using a co-propagating, quasi-resonant laser beam detuned below the resonance was demonstrated [6]. Almost a

decade later, a two-point output of an oven (which produced the atoms) was imaged with an atom lens made of two counter-propagating Gaussian laser beams [7]. In 1992, a near-resonant standing wave detuned above the atomic resonance was used to grow sub-micron sodium lines [8]. Subsequently, a chromium beam was manipulated in the same way to grow high-resolution nanostructures [9]. Also, atomic mirrors have been constructed. For instance, in the first experimental observation a thermal sodium beam falling onto a blue detuned evanescent wave under grazing incidence was shown to reflect [10]. In 1990, a cooled cloud of atoms was released above an evanescent laser field and formed an atomic “trampoline” [11]. As early as in 1930, diffraction of hydrogen and helium atoms from a crystalline surface was observed [12]. Almost 60 years later, microfabricated transmission gratings were used as diffractive elements for atoms [13]. Also, optical standing wave potentials were used to diffract atoms [14]. Concerning atomic interferometers, substantial progress has been made. The first one used a microfabricated Young’s double-slit [15]. Later, interferometers based on three grating geometry [16], stimulated Raman transitions [17], optical Ramsey excitations [18], a static electric field [19] and a longitudinal Stern-Gerlach effect [20] were demonstrated.

The major obstacle of atom optics, when considering its possible applications as, for example, a standard nanolithography tool, is the requirement of atom beams that are slow at least in one direction. This has to be associated with the fact that all potentials $V(\mathbf{r})$ created to date are too weak when compared with the typical kinetic energies of thermal atoms.

1.2.2 Laser cooling

Probably the most amazing form the interaction of atoms with photons can take is the laser cooling of a cloud of atoms.¹ Incident laser beams, when properly tuned near an atomic resonance, exert pressure on atoms. Hereby, the velocity distribution of atoms can be narrowed and the temperature of the atomic ensemble can be dramatically reduced. Fast developments in the field of laser cooling of atoms gave rise to a wealth of new and exciting applications. A high precision atomic clock that is based on a laser cooled cesium fountain and that, if it had started at the birth of the Universe 15 billion years ago, would be off by less than 4 minutes today [21]; Bose-Einstein condensation as a new state of matter [22]; and the possibility of laser-manipulated nanofabrication [9] are only three examples demonstrating the incredible impact the laser cooling has on contemporary physics.

A two-level atom exposed to an electromagnetic field undergoes in general three fundamental radiative events (Fig. 1.1). Provided it is in the ground state, it can absorb a photon from the field and be excited into the upper state. In contrast, an

¹The 1997 Nobel prize for physics was awarded jointly to Steven Chu, Claude Cohen-Tannoudji and William D. Phillips for development of methods to cool and trap atoms with laser light.

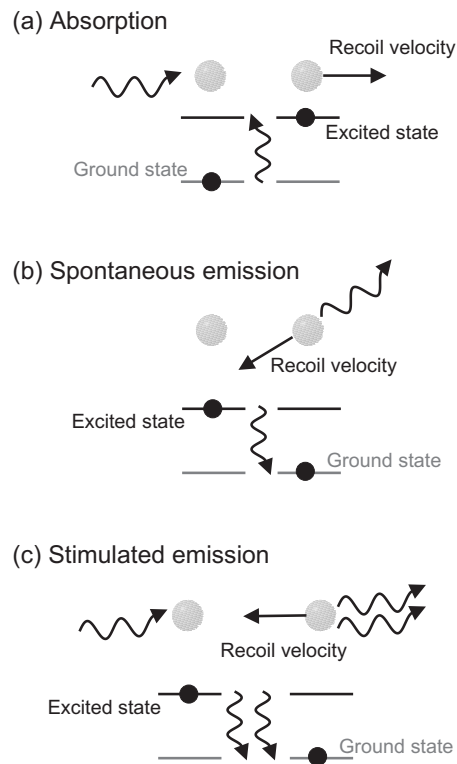


Figure 1.1: Fundamental interactions between atoms and photons: (a) absorption, (b) spontaneous emission, (c) stimulated emission.

excited atom can emit a photon both into the vacuum (spontaneous emission) or back into the excitation field itself (stimulated emission). Which of these processes dominates is dictated by the atomic properties and field parameters.

In January 1975 Hänsch and Schawlow published a paper entitled “Cooling of gases by laser radiation” [23]. In the abstract to this paper they say: “It is shown that a low density gas can be cooled by illuminating it with intense, quasi-monochromatic light confined to the lower-frequency half of a resonance line’s Doppler width. Translational energy can be transferred from the gas to the scattered light, until the atomic velocity is reduced by the ratio of the Doppler width to the natural line width.” The proposed cooling mechanism is today known as Doppler cooling. A two-level atom absorbing a photon from a laser beam [Fig. 1.1(a)] gains a recoil momentum $\hbar\mathbf{k}$, where \mathbf{k} is

the wave-vector of the laser photon. After being excited, the atom emits a photon by spontaneous emission [Fig. 1.1(b)] and gains again a recoil momentum. Now, however, the recoil is in an arbitrary direction. The result is that the atom “feels” a pressure in the direction of the laser beam, while the relaxation causes it to walk randomly in space – Brownian motion. Tuning the laser frequency below the atomic transition frequency, the atoms moving in the direction opposite the laser beam are more likely to absorb photons than the ones moving with the beam. This is due to the Doppler effect. Applying six laser beams along $\pm x$, y , and z directions, the atoms would experience pressure from each direction they try to move in. A cloud of atoms can thus be slowed down. The minimum achievable temperature T_D with Doppler cooling is [24]

$$k_B T_D = \hbar \Gamma / 2, \quad (1.5)$$

where Γ is the natural linewidth of the atomic transition and k_B is the Boltzmann constant. This result is obtained when the detuning from the resonance $\Delta = -\Gamma/2$. The velocity capture range of Doppler cooling Δv is determined by Γ ,

$$k \Delta v \sim \Gamma. \quad (1.6)$$

We note that in the six beam configuration the atoms remain in the region where the laser beams cross each other until they diffuse away due to the Brownian motion. The confinement times can be estimated from the Einstein random walk relation

$$\langle x^2 \rangle = 2Dt, \quad (1.7)$$

where t is the time and $D = k_B T / \alpha$ is the Einstein diffusion coefficient. For atoms moving with velocities such that $kv < \Gamma$, the radiation force is a damping force $F = -\alpha v$. The laser beams form a viscous medium called optical molasses.

In 1985 Chu *et al.* reported on “Three-dimensional viscous confinement and cooling of atoms by resonance radiation pressure” [25]. It was claimed that neutral sodium atoms were cooled to about 240 μK . For sodium atoms $\Gamma/2\pi = 10$ MHz at ${}^3S_{1/2} \rightarrow {}^3P_{3/2}^o$ and from Eq. (1.5) follows that $T_D = 240$ μK . What an amazing agreement! Steven Chu wrote about it in his Nobel lecture [26]: “Our first measurements showed a temperature of 185 μK ... We then made the cardinal mistake of experimental physics: instead of listening to Nature, we were overly influenced by theoretical expectations. By including a fudge factor to account for the way atoms filled the molasses region, we were able to bring our measurement into accord with our expectations.” In 1988 the group of Phillips from the National Institute of Standards and Technology (NIST) reported temperatures of a sodium cloud of 43 ± 20 μK [27], much lower than T_D . This result was unexpected but it did not take long until the processes that lead to these extremely low temperatures were identified and new cooling schemes were proposed.

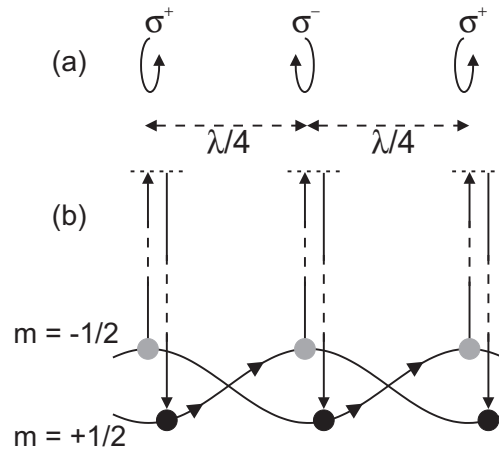


Figure 1.2: Sisyphus cooling. (a) Lin \perp lin polarization configuration. (b) Spatial modulation of the light shifts for an atom with two Zeeman sublevels ($m = \pm 1/2$) and of the optical pumping rates between them. (After [28].)

Thorough accounts of laser cooling below the Doppler limit were given in 1989 by two groups – Chu’s at Stanford [29] and Cohen-Tannoudji’s at Ecole Normale Supérieure [30]. Both these groups identified the strong cooling force acting on slow atoms in an optical molasses with the magnetic sublevel structure and the presence of polarization gradients. If polarization gradients were not present, the cooling force is simply the Doppler force (supposing low laser powers such that stimulated effects can be neglected). Dalibard and Cohen-Tannoudji treated this problem in a very elegant and simple way [30]. In a one-dimensional configuration they analyzed two polarization arrangements – (i) the two counter-propagating laser beams are linearly polarized and the polarizations are mutually orthogonal (lin \perp lin configuration) and (ii) both beams are circularly polarized, one right and the other one left ($\sigma^+ - \sigma^-$). In the lin \perp lin case the polarization state changes from linear to σ^- to orthogonal linear to σ^+ to linear across $\lambda/2$, where λ is the laser wavelength [Fig. 1.2(a)]. If $\sigma^+ - \sigma^-$ configuration is applied the polarization remains always linear but its direction is rotated by π across $\lambda/2$. The mechanisms leading to sub-Doppler temperatures are: (i) the ac-Stark light-shifts of the ground-state Zeeman sublevels are spatially modulated and optical pumping leads to dipole forces and to a Sisyphus effect (see below); (ii) the atomic motion produces a difference in the ground-state sublevel populations, herewith giving rise to an unbalanced radiation pressure.

Here, we briefly describe the Sisyphus effect. To this end we follow the discussion

presented in [28]. An atom with a ground state with an angular momentum $J = 1/2$ has two Zeeman sublevels $m = \pm 1/2$ that are degenerate in the absence of a magnetic field. This degeneracy is removed in the lin \perp lin laser field due to different light shifts the sublevels undergo. The energy diagram shows a spatial modulation of the Zeeman sublevels with a period $\lambda/2$ [Fig. 1.2(b)]. At the position with σ^+ laser polarization the atom is optically pumped into the $m = +1/2$ sublevel, while at the position with σ^- it is pumped into $m = -1/2$. Because the optical pumping time is finite, there is a time lag between internal and external variables. The atom climbs up the potential hill where the probability of transfer to the lower sublevel is the highest. The energy difference is carried away by a blue-shifted photon which is in expense of the atomic kinetic energy. The low temperature limit of the Sisyphus cooling T was derived in [30] in the limit $\Gamma \ll |\Delta|$ and is given by

$$k_B T \simeq \frac{\hbar \Omega^2}{8|\Delta|}, \quad (1.8)$$

where Ω is the Rabi frequency. It is defined by

$$\Omega = \frac{\mathbf{p} \cdot \mathbf{E}}{\hbar}, \quad (1.9)$$

with \mathbf{E} being the laser electric field and \mathbf{p} being the atomic dipole moment. The Rabi frequency is a measure for the coupling between the ground and the excited state mediated by \mathbf{E} . Under the influence of the laser field the atomic wave-function oscillates between the ground and the excited state at Ω . Now, it follows from Eqs. (1.8) and (1.9) that for a given Δ decreasing the laser power means decreasing T , while for a given laser power increased Δ results in lower T . There is a limit for the Sisyphus cooling scheme which is due to the recoil energy gained by the atom when absorbing or emitting a photon.

To overcome even the recoil limit schemes such as velocity-selective coherent population trapping (VSCPT) and Raman cooling were proposed. VSCPT uses destructive quantum interference between different absorption amplitudes. It was demonstrated as early as in 1988 by Aspect *et al.* [31]. A metastable helium beam was cooled in the transverse direction (one-dimensional molasses) to a temperature of $2 \mu\text{K}$, well below the recoil energy of $4 \mu\text{K}$. Raman cooling uses appropriate sequences of stimulated Raman transitions and optical pumping pulses to achieve energies below the recoil. Using this technique, Kasevich and Chu [32] reported on collimation of a sodium beam to an effective transverse temperature of 100 nK . The recoil energy for sodium is $1 \mu\text{K}$.

When laser cooling schemes are used in only one or two dimensions while in the main direction the atoms are undisturbed and remain fast, high collimation degrees can be achieved. At the same time, the flux of atoms is not reduced as it would be in the case of mechanical collimation.

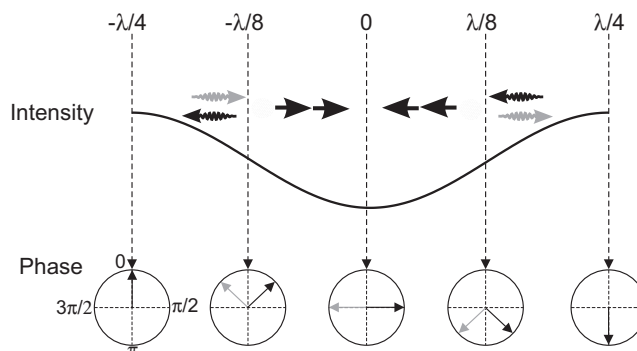


Figure 1.3: Stimulated force on atoms in a blue detuned laser standing wave.

1.2.3 Laser focusing

Besides the spontaneous (velocity-dependent) force, there is another form of interaction between light and atoms. We visualize this interaction using a simple picture. An atom in an intense laser standing wave (SW) created from two counter-propagating plane waves whose frequency is tuned far above the atomic resonance ($\Delta \gg \Gamma$) absorbs a photon from one wave and emits it into the other wave by stimulated emission. The atom behaves like a dipole oscillator driven far above its resonance frequency. Therefore, it responds out of phase to the stimulus. In Fig. 1.3 this process is depicted in terms of single photon events. The phases of the two laser waves are also shown. An atom at rest located on the left from the SW intensity minimum sees the photon traveling from the left to the right first (out of phase response) and absorbs it. Then, it is stimulated by the wave traveling from the right to the left back into its ground state. It thus gains two recoil momenta to the right and the cycle is repeated, until passing through the minimum. The role of the two traveling waves is reversed. The resulting motion of the atom is thus oscillatory around the minimum. For negative detunings ($\Delta \ll -\Gamma$), the atoms would oscillate around the intensity maxima (in phase response).

While the above visualization and also classical picture of this so-called dipole force give a qualitatively good impression, to correctly model the interaction a fully quantum treatment must be adopted. This was done first by Gordon and Ashkin [33]. Later, it was “revisited” by Dalibard and Tannoudji [34] who implemented the dressed-atom formalism to a two-level atom interacting with a monochromatic light field. The dipole force is derived from an optical potential $U(\mathbf{r})$ for the atoms given

by

$$U(\mathbf{r}) = \frac{\hbar\Delta}{2} \ln \left[1 + \frac{2\Omega^2(\mathbf{r})}{\Gamma^2 + 4\Delta^2} \right]. \quad (1.10)$$

In the limit $\Omega \ll |\Delta|$ and $\Gamma \ll |\Delta|$ the optical potential simplifies, it is proportional to the square of the Rabi frequency Ω ,

$$U(\mathbf{r}) = \frac{\hbar\Omega^2(\mathbf{r})}{4\Delta}. \quad (1.11)$$

In this approximation, $U(\mathbf{r})$ is linear in the laser intensity $I(\mathbf{r})$, $U(\mathbf{r}) \propto I(\mathbf{r})$. Eqs. (1.10) and (1.11) can be used to model the atomic behavior in a far-detuned laser field with a non-zero gradient in $I(\mathbf{r})$. We will use these equations in Sec. 2.1 for the analysis of the focusing properties of a SW atom lens. One should bear in mind, however, that the above conservative potential assumes no spontaneous emission and also adiabatic evolution of the dressed state populations.

Here, we point out that an atom moving across a blue-detuned laser SW entering the radiation field near the intensity minimum under a small angle – paraxial approximation – oscillates with a period that is independent of its initial transverse position (which is along the direction in which the SW is created). This can be seen from Eq. (1.11) which, for atoms located near the potential minimum, leads to a quadratic dependence on the transverse position. Such a potential is for atoms similar to what a lens is for photons. A laser SW can thus be used to focus atoms to a spot size of only several nanometers (the whole size of an atom lens is $\lambda/2$, where λ is the wavelength).

The first proposal of this potentially useful nanofabrication tool was made in 1987 by Balykin and Letokhov [35]. Later, McClelland analyzed “Atom-optical properties of a standing-wave light field” [36]. He has extensively used the analogy of atom optics with particle optics that he and Scheinfein implemented earlier on to an atom beam focused in a donut-type laser mode [37].

The idea of using light for direct writing with atoms has stimulated an interest in focusing of atoms in a laser SW. This approach is considered to form a promising tool for massively parallel patterning of surfaces with nanometer-scale resolution. By using atoms that stick well on surfaces, this method can be applied to write structures directly onto substrates. On the other hand, metastable rare gases or chemically aggressive atoms can be used in an indirect way: the pattern is first imaged onto a special resist and then transferred to the substrate using other methods, such as selective etching. The principles of laser-focused nanofabrication are schematically presented in Fig. 1.4. An atom beam exits a source, such as a Knudsen cell. Then, it is collimated in an optical molasses. Finally, it is transferred through a SW light “mask” onto a substrate.

The first demonstration of laser-focused atomic deposition dates back to 1992 when Timp *et al.* reported experiments with neutral sodium atoms [8]. Subsequently,

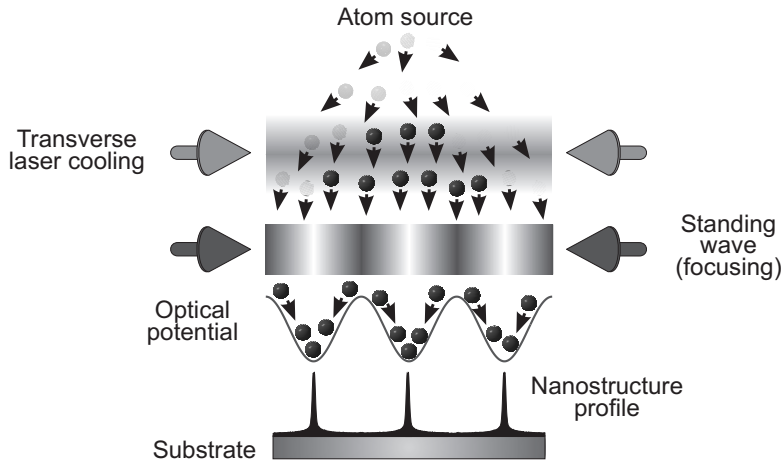


Figure 1.4: Basic principles of laser-focused atomic deposition.

the NIST group around McClelland produced nanometer-scale lines of chromium [9]. This experiment has initiated a new era in laser-focused deposition as it was the first demonstration of structures stable even at ambient conditions (Fig. 1.5). Later, the same group demonstrated that a square-lattice of equidistantly spaced features can be produced by super-imposing two laser SW's at a normal angle [38]. In a similar way, Mlynek's group at the University of Konstanz fabricated nanostructures with a hexagonal symmetry by crossing three laser beams at mutual angles of 120° [39]. Also, aluminum [40] in the direct deposition regime and cesium [41] in the lithography regime with a self-assembled monolayer as the resist were used for making nanolines. More complicated periodic patterns may be written by moving the substrate with a nanometer-scale accuracy or by using more complex laser field patterns. The latter approach has been adopted recently. In 1996 the NIST group reported on "Raman-induced avoided crossings in adiabatic optical potentials: Observation of $\lambda/8$ spatial frequency in the distribution of atoms" [42]. Working in $\text{lin}\perp\text{lin}$ polarization configuration, lines with a periodicity of $\lambda/8$ were grown. In 1999 the Konstanz group extended this polarization-gradient approach to laser-manipulated nanostructuring to two dimensions [43].

Using laser-focused deposition, a certain amount of unintended background is always present. For applications requiring separated nanostructures this can, in principle, be removed by some post-deposition processing. Background removal by reactive-etch plasma was demonstrated on laser-focused chromium nanostructures grown

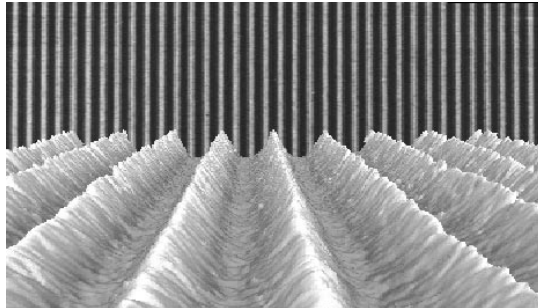


Figure 1.5: Chromium nanolines grown at the National Institute of Standards and Technology. The period of this structure is 213 nm. (*Courtesy of Jabez J. McClelland – NIST.*)

onto a silicon substrate, giving rise to an array of separated chromium wires as narrow as 68 nm [44]. Subsequent removal of chromium by a wet etch can then produce silicon nanostructures. Also, a replica of chromium features made by laser-focusing was molded using polymeric materials [45]. Further use of laser-focused chromium was demonstrated by using the nanolines as a shadow mask for an iron evaporator and thereby fabricating an array of iron magnetic nanowires [46].

Most recently, the efforts of the laser-focusing community have moved towards studies of the basic processes that lead to the structure formation. We will analyze some of the problems later in this thesis. Here, we make only a few remarks. Firstly, limitations on the resolution are imposed by the interaction of atoms with photons. To account for phenomena like spontaneous emission, atomic diffraction, saturation of the atomic transition, etc., a fully quantum treatment to an atom lens must be implemented. An attempt to do this was made by Lee [47] in his paper on “Quantum-mechanical analysis of atom lithography.” Secondly, surface diffusion and growth phenomena might also play a role in determining the achievable parameters with the laser-focusing process. The most direct experimental evidence that surface growth is an important effect to be considered was given by the NIST group [48]. Later, two theoretical studies by Bradley *et al.* [49] and our own [50] followed and have shown how different growth models influence the nanostructure shape and the ultimate resolution.

For reviews on laser manipulation of atoms, see [24, 26, 28, 51–57].

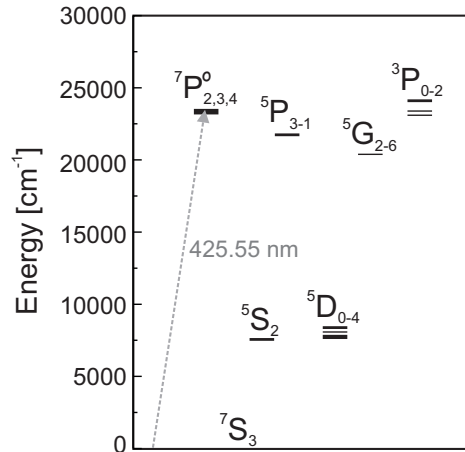


Figure 1.6: ^{52}Cr energy diagram.

1.3 Chromium

Chromium (Cr) atoms are used throughout this work. It is therefore useful to summarize their basic properties at this place.

Essentials [58]. The atomic number of Cr is 24. It is in the group 6, period 4, block d of the periodic table. Atomic weight of Cr is 51.9961(6) amu (atomic mass units). Cr is solid at room temperature and atmospheric pressure. It is a steel-gray, lustrous, hard and brittle metal.

Electronic configuration [59]. The ground state electronic configuration of Cr is $1s^2.2s^2.2p^6.3s^2.3p^6.3d^5.4s^1$. The term symbol of the ground state is $7S_3$. The energy level diagram of the dominant Cr isotope ^{52}Cr is shown in Fig. 1.6. The optical pumping transition $7S_3 \rightarrow 7P_4^\circ$ is at a vacuum wavelength of 425.55292 nm (blue, almost violet light). The natural linewidth of this resonance is $\Gamma/2\pi \simeq 5$ MHz. The other two (blue) transitions from the ground state – $7S_3 \rightarrow 7P_3^\circ$ and $7S_3 \rightarrow 7P_2^\circ$ – are at vacuum wavelengths of 427.59986 nm and 429.09228 nm, respectively. The natural linewidth of these transitions is also about 5 MHz.

Thermal properties. The melting point of Cr is 1842 ± 20 °C [60] and the boiling point is 2671 °C [58]. For fast growth (high flux) of thin Cr films a high-temperature effusion cell is usually employed.

Crystal structure [58]. The crystal structure of solid Cr is bcc with the cell parameter $a = 2.91$ Å.

Naturally occurring isotopes [58]. Naturally occurring Cr isotopes are: ^{50}Cr

(abundance 4.345%, mass 49.946 amu), ^{52}Cr (83.789%, 51.941 amu), ^{53}Cr (9.501%, 52.941 amu), and ^{54}Cr (2.365%, 53.939 amu). Only the ^{53}Cr isotope has a non-zero nuclear spin $3/2$.

Atom optics with chromium. As Cr atoms are excited to the $^7P_4^o$ state, they occasionally decay to either the 5D_3 or 5D_4 metastable states via an inter-combination transition. These leaks limit the resonant laser cooling and trapping interaction time to a few ms. This time can be extended by repumping the atoms back into the $^7P_3^o$ state using vacuum wavelengths of 653.97 nm (5D_3) and 663.18 nm (5D_4) [61].

Cr atoms were used for laser manipulation by two groups in the past – McClelland’s at NIST and Mlynek’s at the University of Konstanz. A thermal beam of chromium atoms was collimated down to a divergence of 0.16 mrad full-width at half maximum (FWHM) [62]. Furthermore, this species was used in laser-focused deposition studies [9]. Also, magneto-optical trapping (MOT) of Cr was reported very recently [61]. Over 10^6 atoms were trapped at average densities over 10^{16} m^{-3} .

For our purposes, chromium is an ideal candidate to start with. For laser manipulation, it is relatively easy to access with known laser sources. Furthermore, when deposited, it sticks well on surfaces and forms stable films. At ambient, the uppermost layers of chromium oxidize leading to stabilization of the surface. Chromium and its oxides are frequently used as a protective-layer for other, more reactive materials.

References

- [1] R.P. Feynman. There’s plenty of room at the bottom. In A.J.G. Hey, editor, *Feynman and Computation*, chapter 7, pages 63–76. Perseus Books, Reading, 1999.
- [2] H.S Nalwa, editor. *Handbook of Nanostructured Materials and Nanotechnology*. Academic Press, San Diego, 2000.
- [3] G.L. Timp, editor. *Nanotechnology*. Springer-Verlag, Heidelberg, 1999.
- [4] K.E. Drexler. *Nanosystems: Molecular Machinery, Manufacturing, and Computation*. John Wiley & Sons, New York, 1992.
- [5] A. ten Wolde, editor. *Nanotechnology, Towards a Molecular Construction Kit*. Netherlands Study Center for Technology Trends, The Hague, 1998.
- [6] E. Bjorkholm, R.R. Freeman, A. Ashkin, and D.B. Pearson. Observation of focusing of neutral atoms by the dipole forces of resonance-radiation pressure. *Phys. Rev. Lett.*, 41:1361–1364, 1978.
- [7] V.I. Balykin, V.S. Letokhov, and A.I. Sidorov. Focusing atomic beams by the dissipative radiation-pressure force of laser light. *JETP Lett.*, 43:217–220, 1986.

-
- [8] G. Timp, R. E. Behringer, D. M. Tennant, J. E. Cunningham, M. Prentiss, and K. K. Berggren. Using light as a lens for submicron, neutral-atom lithography. *Phys. Rev. Lett.*, 69:1636–1639, 1992.
- [9] J.J. McClelland, R.E. Scholten, E.C. Palm, and R.J. Celotta. Laser-focused atomic deposition. *Science*, 262:877–880, 1993.
- [10] V.I. Balykin, V.S. Letokhov, Yu.B. Ovchinnikov, and A.I. Sidorov. Quantum state selective mirror reflection of atoms by laser light. *Phys. Rev. Lett.*, 60:2137–2140, 1988.
- [11] M.A. Kasevich, D.S. Weiss, and S. Chu. Normal-incidence reflection of slow atoms from an optical evanescent wave. *Opt. Lett.*, 15:607–609, 1990.
- [12] I. Estermann and O. Stern. Beugung von Molekularstrahlen. *Z. Phys.*, 61:95–125, 1930.
- [13] D.W. Keith, M.L. Schattenburg, H.I. Smith, and D.E. Pritchard. Diffraction of atoms by a transmission grating. *Phys. Rev. Lett.*, 61:1580–1583, 1988.
- [14] P.J. Martin, P.L. Gould, B.G. Oldaker, A.H. Miklich, and D.E. Pritchard. Diffraction of atoms moving through a standing light wave. *Phys. Rev. A*, 36:2495–2498, 1987.
- [15] O. Carnal and J. Mlynek. Young’s double-slit experiment with atoms: A simple atom interferometer. *Phys. Rev. Lett.*, 66:2689–2692, 1991.
- [16] D.W. Keith, C.R. Ekstrom, Q.A. Turchette, and D.E. Pritchard. An interferometer for atoms. *Phys. Rev. Lett.*, 66:2693–2696, 1991.
- [17] M.A. Kasevich and S. Chu. Atomic interferometry using stimulated Raman transitions. *Phys. Rev. Lett.*, 67:181–184, 1991.
- [18] F. Riehle, Th. Kisters, A. Witte, J. Helmcke, and Ch.J. Bordé. Optical Ramsey spectroscopy in a rotating frame: Sagnac effect in a matter-wave interferometer. *Phys. Rev. Lett.*, 67:177–180, 1991.
- [19] Yu.L. Sokolov and V.P. Yakovlev. Measurement of the Lamb shift in the hydrogen atom ($n=2$). *JETP Lett.*, 56:7–17, 1982.
- [20] Ch. Miniatura, J. Robert, O. Gorceix, V. Lorent, S. Le Boiteux, J. Reinhardt, and J. Baudon. Atomic interferences and the topological phase. *Phys. Rev. Lett.*, 69:261–264, 1992.
- [21] S. Ghezali, Ph. Laurent, S.N. Lea, and A. Clairon. An experimental study of the spin-exchange frequency shift in a laser-cooled cesium fountain frequency standard. *Europhys. Lett.*, 36:25–30, 1996.

-
- [22] M.H. Anderson, J.R. Ensher, M.R. Matthews, C.E. Wieman, and E.A. Cornell. Observation of Bose-Einstein condensation in a dilute atomic vapor. *Science*, 269:5221, 1995.
- [23] T.W. Hänsch and A.L. Schawlow. Cooling of gases by laser radiation. *Opt. Comm.*, 13:68–69, 1975.
- [24] C. Cohen-Tannoudji and W.D. Phillips. New mechanisms for laser cooling. *Physics Today*, 43:33–40, 1990.
- [25] S. Chu, L. Hollberg, J.E. Bjorkholm, A. Cable, and A. Ashkin. Three-dimensional viscous confinement and cooling of atoms by resonance radiation pressure. *Phys. Rev. Lett.*, 55:48–51, 1985.
- [26] S. Chu. The manipulation of neutral particles. *Rev. Mod. Phys.*, 70:685–706, 1998.
- [27] P.D. Lett, R.N. Watts, C.I. Westbrook, W.D. Phillips, P.L. Gould, and H.J. Metcalf. Observation of atoms laser cooled below the Doppler limit. *Phys. Rev. Lett.*, 61:169–172, 1988.
- [28] C. Cohen-Tannoudji. Manipulating atoms with photons. *Rev. Mod. Phys.*, 70:707–720, 1998.
- [29] P.J. Ungar, D.S. Weiss, E. Riis, and S. Chu. Optical molasses and multilevel atoms: theory. *J. Opt. Soc. Am. B*, 6:2058–2071, 1989.
- [30] J. Dalibard and C. Cohen-Tannoudji. Laser cooling below the Doppler limit by polarization gradients: simple theoretical models. *J. Opt. Soc. Am. B*, 6:2023–2045, 1989.
- [31] A. Aspect, E. Arimondo, R. Kaiser, N. Vansteenkiste, and C. Cohen-Tannoudji. Laser cooling below the one-photon recoil energy by velocity-selective coherent population trapping. *Phys. Rev. Lett.*, 61:826–829, 1988.
- [32] M. Kasevich and S. Chu. Laser cooling below a photon recoil with three level atoms. *Phys. Rev. Lett.*, 69:1741–1744, 1992.
- [33] J.P. Gordon and A. Ashkin. Motion of atoms in a radiation trap. *Phys. Rev. A*, 21:1606–1617, 1980.
- [34] J. Dalibard and C. Cohen-Tannoudji. Dressed-atom approach to atomic motion in laser light: the dipole force revisited. *J. Opt. Soc. Am.*, 2:1707–1720, 1985.
- [35] V.I. Balykin and V.S. Letokhov. The possibility of deep laser focusing of an atomic beam into the Å-region. *Opt. Comm.*, 64:151–156, 1987.

-
- [36] J.J. McClelland. Atom optical properties of a standing-wave light field. *J. Opt. Soc. Am. B*, 12:1761–1768, 1995.
- [37] J.J. McClelland and M.R. Scheinfein. Laser focusing of atoms: a particle optics approach. *J. Opt. Soc. Am. B*, 8:1974–1986, 1991.
- [38] R. Gupta, J.J. McClelland, Z.J. Jabbour, and R.J. Celotta. Nanofabrication of a two-dimensional array using laser-focused atomic deposition. *Appl. Phys. Lett.*, 67:1378–1380, 1995.
- [39] U. Drodofsky, J. Stuhler, Th. Schulze, M. Drewsen, B. Brezger, T. Pfau, and J. Mlynek. Hexagonal nanostructures generated by light mask for neutral atoms. *Appl. Phys. B*, 65:755–759, 1997.
- [40] R.W. McGowan, D.M. Giltner, and S.A. Lee. Light force cooling, focusing, and nanometer-scale deposition of aluminum atoms. *Opt. Lett.*, 20:2535–2537, 1995.
- [41] F. Lison, H.-J. Adams, D. Haubrich, M. Kreis, S. Nowak, D. Meschede. Nanoscale atomic lithography with a cesium atom beam. *Appl. Phys. B*, 65:419–421, 1997.
- [42] R. Gupta, J.J. McClelland, P. Marte, and R.J. Celotta. Raman-induced avoided crossings in adiabatic optical potentials: Observation of $\lambda/8$ spatial frequency in the distribution of atoms. *Appl. Phys. Lett.*, 67:1378–1380, 1995.
- [43] B. Brezger, Th. Schulze, P.O. Schmidt, R. Mertens, T. Pfau, and J. Mlynek. Polarization gradient light masks in atom lithography. *Europhys. Lett.*, 46:148–153, 1999.
- [44] J.J. McClelland, R. Gupta, Z.J. Jabbour, R.J. Celotta, and G.A. Porkolab. Nanostructure fabrication by reactive-ion etching of laser-focused chromium on silicon. *Appl. Phys. B*, 66:95–98, 1998.
- [45] Y.N. Xia, J.J. McClelland, R. Gupta, D. Qin, X.M. Zhao, L.L. Sohn, R.J. Celotta, G.M. Whitesides. Replica molding using polymeric materials: A practical step toward nanomanufacturing. *Adv. Mater.*, 9:147–149, 1997.
- [46] D.A. Tulchinsky, M.H. Kelley, J.J. McClelland, R. Gupta, and R.J. Celotta. Fabrication and domain imaging of iron magnetic nanowire arrays. *J. Vac. Sci. Technol. A*, 16:1817–1819, 1998.
- [47] C.J. Lee. Quantum-mechanical analysis of atom lithography. *Phys. Rev. A*, 61,063604:1–9, 2000.
- [48] W.R. Anderson, C.C. Bradley, J.J. McClelland, and R.J. Celotta. Minimizing feature width in atom optically fabricated nanostructures. *Phys. Rev. A*, 59:2476–2485, 1999.

-
- [49] R.M. Bradley, A. Eschmann, and S.A. Lee. Theory of feature broadening in direct-write optical lithography. *J. Appl. Phys.*, 88:3316–3322, 2000.
- [50] E. Jurdik, Th. Rasing, H. van Kempen, C.C. Bradley, and J.J. McClelland. Surface growth in laser-focused atomic deposition. *Phys. Rev. B*, 60:1543–1546, 1999.
- [51] S. Chu and C. Wieman, editors. Laser cooling and trapping of atoms. *J. Opt. Soc. Am.*, B6:2020–2278, 1989.
- [52] C.S. Adams, M. Sigel, and J. Mlynek. Atom optics. *Phys. Rep.*, 240:143–210, 1994.
- [53] A. Aspect, R. Kaiser, N. Vansteenkiste, and C.I. Westbrook. Laser manipulation of neutral atoms. *Phys. Scripta*, T58:69–77, 1995.
- [54] C.C. Bradley and R.G. Hulet. Laser cooling and trapping of neutral atoms. In F.B. Dunning and R.G. Hulet, editors, *Experimental Methods in the Physical Sciences*, volume 29B, chapter 8, pages 129–144. Academic Press, San Diego, 1996.
- [55] W.D. Phillips. Laser cooling and trapping of neutral atoms. *Rev. Mod. Phys.*, 70:721–742, 1998.
- [56] H.J. Metcalf and P. van der Straten. *Laser Cooling and Trapping*. Springer-Verlag, Berlin, 1999.
- [57] V.I. Balykin, V.G. Minogin, and V.S. Letokhov. Electromagnetic trapping of cold atoms. *Rep. Prog. Phys.*, 63:1429–1510, 2000.
- [58] M. Winter. WebElements Periodic Table: the periodic table on the World-Wide Web. <http://www.webelements.com>.
- [59] National Institute of Standards and Technology. NIST Atomic Spectra Database. <http://physics.nist.gov/AtData/display.ksh>.
- [60] D. Josell, D. Basak, J.L. McClure, U.R. Kattner, M.E. Williams, and W.J. Boettinger. Moving the pulsed heating technique beyond monolithic specimens: Experiments with coated wires. Submitted to *J. Mater. Res.*
- [61] C.C. Bradley, J.J. McClelland, W.R. Anderson, and R.J. Celotta. Magneto-optical trapping of chromium atoms. *Phys. Rev. A*, 61,053407:1–6, 2000.
- [62] R.E. Scholten, R. Gupta, J.J. McClelland, and R.J. Celotta. Laser collimation of a chromium beam. *Phys. Rev. A*, 55:1331–1338, 1997.

Modeling

In this chapter the aim is to gain more insight into the laser-focused deposition process. First, we calculate the chromium flux distribution in a laser standing wave within a semiclassical trajectory tracing method. Then, the nanostructure growth is studied using three atomistic models of adsorption and diffusion of adatoms on substrates. We show that theoretical predictions of the structure's profile depend sensitively on the parameters chosen within the models.

2.1 Atom lens

One period of a laser standing wave (SW) that is detuned far enough from the atomic resonance can be considered to form an atom lens. This atom lens is due to the fundamental interaction processes between atoms and photons. To account for all properties of such an atom-optical component, a fully quantum treatment is necessary. We do not follow here this most rigorous way. Instead, we work in the semiclassical approximation. In this way, we lose slightly on the general validity of our approach but we gain more insight. A thorough understanding of atom flux distribution is the very first step when considering applications of laser-focused deposition to quantitative surface science and nanostructure research.

Similar approaches to a laser SW atom lens have been used in the past. Berggren *et al.* [1] presented a time-dependent integration method. McClelland [2] eliminated the time from the equation of motion and based his treatment on an extensive analogy with particle optics in the paraxial approximation. Both these works presented a useful analysis of the aberrations of an atom lens and served as a guide for high resolution focusing efforts. Our model is a further generalization allowing for extraction of the atom flux at any position for any set of experimental parameters. This is

essential for a good understanding of the laser focusing process.

2.1.1 Semiclassical model

Description of the model

In the semiclassical approximation (that is, only the mean values of physical observables are of interest), the force acting on an atom moving in a laser field contains both velocity dependent and independent terms [3]. The former terms are nonconservative and demonstrate themselves as damping or accelerating forces. In contrast, the latter terms are conservative in nature. Classically, the conservative force can be thought of as the interaction between the induced atomic dipole with the gradient in the laser electric field. It is therefore often referred to as the dipole force. First, we consider only this dipole force. The (first-order) velocity dependent correction to the atomic motion is added for completeness later on.

The mean dipole force on a two-level atom in a SW laser field is here derived from an optical potential $U(x, y, z)$ [see Eq. (1.10)],

$$U(x, y, z) = \frac{\hbar\Delta}{2} \ln \left[1 + \frac{I(x, y, z)}{I_S} \frac{\Gamma^2}{\Gamma^2 + 4\Delta^2} \right], \quad (2.1)$$

where $\Delta = \omega_L - \omega_0$ is the detuning of the laser frequency ω_L from the atomic resonance frequency ω_0 , Γ is the natural linewidth of the transition, $I(x, y, z)$ is the laser intensity and \hbar is Planck's constant divided by 2π . The saturation intensity of the atomic transition I_S is given by

$$I_S = c\epsilon_0 \left(\frac{\hbar\Gamma}{\mathbf{p} \cdot \mathbf{2}} \right)^2, \quad (2.2)$$

with ϵ_0 being the permittivity of the vacuum, c being the *in vacuo* speed of light and \mathbf{p} being the projection of the atomic dipole moment in the direction of the laser electric field. Concerning geometry we note that the SW created along the x direction focuses atoms deposited along the surface normal z .

The choice of the above interaction potential is motivated by the fact that it includes the effects of saturation which may occur for higher laser intensities and/or smaller detunings. For the purpose of this work it is thus more appropriate than the simpler large detuning approximation.¹ It should be emphasized that this treatment does not take into account the effect of spontaneous emission. However, there is a reason that allows us to neglect this effect. The atomic population approaches its steady state after a time $\sim 1/\Gamma$ and the atoms move fast enough through the spatially varying laser field. Therefore, only a few fluorescence events can take place. The semiclassical approach is supported also by the fact that realistic laser transverse intensity profiles

¹The condition $\Delta \gg (I_0/I_S)^{1/2}\Gamma$ linearizes the dipole potential in $I(x, y, z)$ [see Eq. (1.11)].

do not turn on instantaneously. The optical fields (e.g., Gauss-Hermitian) gradually increase and the atomic state population is driven nearly adiabatically.

Using Eq. (2.1), the atomic trajectory is calculated by numerical integration of the Newton equation of motion which, for computational convenience, is here written as

$$\frac{d^2 X}{dZ^2} = -\frac{1}{2\pi} \frac{aG(X, Y, Z)}{1 + p_0 G(X, Y, Z)} \tan(2\pi X). \quad (2.3)$$

The excitation and saturation parameters a and p_0 ,

$$a = \frac{\hbar\Delta}{2E_0} p_0 k^2 W_0^2, \quad (2.4)$$

and

$$p_0 = \frac{4I_0}{I_S} \frac{\Gamma^2}{\Gamma^2 + 4\Delta^2}, \quad (2.5)$$

respectively, are the only two parameters which control the atomic motion in a SW. Here, E_0 is the total energy of the atom, I_0 is the maximum intensity of one of the two counter-propagating traveling laser waves and $G(X, Y, Z)$ is a dimensionless function describing the laser beam shape. The two transverse positions X and Y , respectively, are measured relative to the laser wavelength $\lambda = 2\pi/k$ ($X = x/\lambda$, $Y = y/\lambda$). The longitudinal position Z is given in units of W_0 ($Z = z/W_0$). Note that the forces acting along Z and Y are neglected. This is a justified assumption. The gradients of the light intensity along Y and Z are much smaller than along X .

In Fig. 2.1 the semiclassical trajectory tracing approach is illustrated for a Gaussian SW. An atom with appropriate initial transverse and longitudinal velocities $v_x = v_x^{(i)}$ and $v_z = v_z^{(i)}$, respectively, and at an initial transverse position $X = X^{(i)}$ is generated in front of the laser beam. Then, it oscillates between the potential walls until reaching the final longitudinal position $Z = Z^{(f)}$. The classical atomic trajectory is actually calculated employing an adaptive step size, fourth-order Runge-Kutta type algorithm [4].

Qualitative analysis

For a step-like laser beam² and $p_0 \ll 1$ and $X^{(i)} \ll 1$, Eq. (2.3) reduces to that of a simple harmonic oscillator. This means that an atom with an initial transverse velocity $v_x^{(i)} = 0$ would oscillate around the maxima ($\Delta < 0$) or minima ($\Delta > 0$) of the laser intensity, independent of its initial position, with a period τ given by

$$\tau = \frac{\lambda}{\Gamma} \sqrt{\frac{\Delta M_a I_S}{\hbar I_0}}, \quad (2.6)$$

² $G(X, Y, Z) = \theta(Z) \sin^2(2\pi X)$, where $\theta(Z)$ is the Heaviside function.

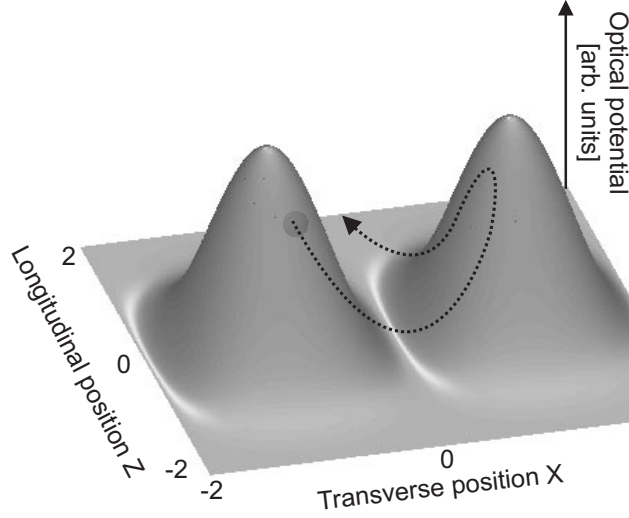


Figure 2.1: Schematic illustration of the semiclassical trajectory tracing method.

where M_a is the atomic mass. A SW atom lens is thus in some sense similar to an optical immersion lens. To place the first focus of this lens at a distance $Z^{(f)} = 1$ from the point where the laser intensity turns on instantaneously requires $a = \pi^2/4 \simeq 2.47$. The focal length can thus be controlled by adjusting the laser parameters I_0 and Δ , which are related to a via Eqs. (2.4) and (2.5). In the non-paraxial regime, an analytical solution to Eq. (2.3) no longer exists. Deviations from the paraxial solution can then be treated as aberrations, akin to conventional optics.

In order to account for a more realistic experimental case, the focusing properties of a Gaussian SW are investigated in the following. Such a beam is characterized by

$$I_0 = \frac{2}{\pi} \frac{P}{W_0^2}, \quad (2.7)$$

and

$$G(X, Y, Z) = \exp[-2(Z^2 + Y^2)] \sin^2(2\pi X), \quad (2.8)$$

where P is the incident traveling laser power and W_0 is the $1/e^2$ beam radius. Setting $p_0 = 0$, $v_x^{(i)} = 0$ and $X^{(i)} \ll 1$, paraxial properties in the large detuning regime are evaluated. In Fig. 2.2(a) the location of the first paraxial focus (in the plane $Y = 0$) is shown as a function of a . For increasing a , this focus moves towards the atom source and crosses the laser beam center at $a \simeq 5.37$. The latter statement is best illustrated

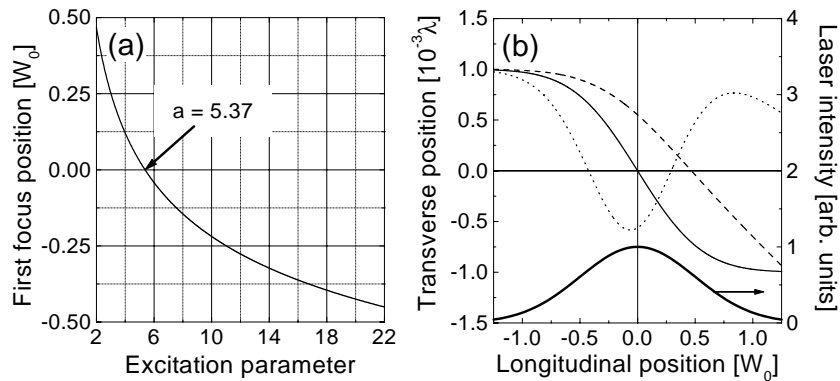


Figure 2.2: Paraxial approximation to a Gaussian laser SW atom lens. (a) Calculated first focus position as a function of the excitation parameter a . (b) Atomic trajectories for $a = 2$ (dashed line), 5.37 (solid line) and 20 (dotted line). The Gaussian laser intensity profile is also shown (thick solid line).

by plotting atomic trajectories for, say, $a = 2.0$, 5.37 and 20.0. These are shown in Fig. 2.2(b) as the dashed, solid and dotted lines, respectively, for $X^{(i)} = 10^{-3}$.

Initial conditions

Let us now turn to a particular case of chromium atoms. In the following, the laser frequency is detuned from the ${}^7S_3 \rightarrow {}^7P_4^o$ ${}^{52}\text{Cr}$ transition at $\lambda = 425.55$ nm, for which $\Gamma/2\pi = 5$ MHz and $I_S = 85$ Wm^{-2} , by $\Delta/2\pi = 500$ MHz. The $1/e^2$ laser beam radius W_0 is set to 60 μm .³ The laser-focused atom flux $f(X, Y, Z)$ for given Y and Z is calculated by tracing classical trajectories of 250,000 (random) atoms. The initial transverse positions $X^{(i)}$ are generated from a flat distribution (that is, all positions are equally likely). Only one period of the SW is taken into account because the assumed focusing geometry ensures an intrinsic periodicity (periodic boundary conditions). The atom flux at a final longitudinal position $Z^{(f)}$ is then determined by calculating a histogram of final transverse positions $X^{(f)}$ at a grid consisting of 855 intervals (the ratio between the SW period 212.775 nm and the nearest neighbor distance in the chromium lattice 0.249 nm).

Whenever a thermal chromium beam is considered throughout this work, the initial longitudinal velocities $v_z^{(i)}$ obey the Maxwell-Boltzmann statistics. Note that

³The numerical values of $\Delta/2\pi = 500$ MHz and $W_0 = 60$ μm correspond to the experiments carried out at the National Institute of Standards and Technology (NIST) in Gaithersburg (MD, USA). These experiments are reported on in Sec. 4.3.2.

only the number of atoms (with a given $v_z^{(i)}$) crossing a unit area in the plane $Z = \text{const}$ above the SW is of interest here. Thus, $v_z^{(i)}$ should follow the distribution $\rho_o(v_z)$,

$$\rho_o(v_z) = \frac{1}{2} \left(\frac{M_a}{k_B T_o} \right)^2 v_z^3 \exp \left(- \frac{M_a v_z^2}{2k_B T_o} \right), \quad (2.9)$$

where k_B is the Boltzmann constant. The oven temperature T_o is set to 1900 K. The most probable $v_z^{(i)} \simeq 955 \text{ ms}^{-1}$. The $a \simeq 5.37$ rule then requires only a fairly moderate focusing laser power of 7.8 mW.

The initial transverse velocities $v_x^{(i)}$ are assumed to exhibit a Gaussian spread with the corresponding distribution $\rho_c(v_x)$ given by

$$\rho_c(v_x) = \sqrt{\frac{M_a}{2\pi k_B T_c}} \exp \left(- \frac{M_a v_x^2}{2k_B T_c} \right). \quad (2.10)$$

T_c is the transverse temperature of the atom beam. We relate T_c to the full-width at half maximum (FWHM) collimation angle α_0 , a readily measurable quantity in an experiment, via (see Sec. 4.2.1 and [2, 5])

$$T_c = T_o \frac{\alpha_0^2}{4(\sqrt{2} - 1)}. \quad (2.11)$$

Even though the choice of the above distributions is essentially arbitrary, they nevertheless reflect conditions typically encountered in an experiment. Any other statistics can be incorporated into the code in a straightforward way.

Characterization of the atom flux

To characterize the flux fully, one either needs its real-space profile or amplitudes of its spatial Fourier series. Nevertheless, it is useful to introduce two descriptive parameters, the width w and the contrast ζ . The former is here defined as the structure FWHM (above the background), while the latter is the ratio of the height (above the background) to the background.

2.1.2 Aberrations and channeling

Spherical aberration

Let us now consider a chromium beam that contains atoms with only one longitudinal velocity and that does not exhibit a spread in transverse velocities ($\alpha_0 = 0$). We set the calculation parameters to: $v_z^{(i)} = 955 \text{ ms}^{-1}$, $v_x^{(i)} = 0$, $P = 7.8 \text{ mW}$, $\Delta/2\pi = 500 \text{ MHz}$ and $W_0 = 60 \text{ }\mu\text{m}$. The resulting atom flux distribution $f(X, 0, 0)$ is shown in Fig. 2.3(a). For demonstration, 21 atomic trajectories with uniformly spaced initial

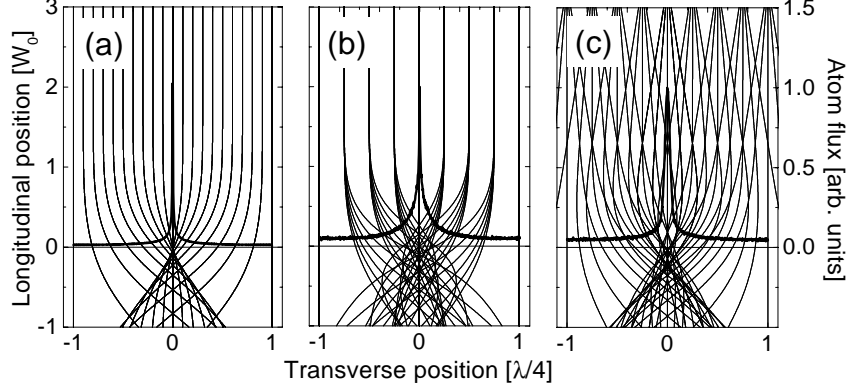


Figure 2.3: Calculated chromium trajectories (thin lines) and densities (thick lines) at the center ($Z = 0$, $Y = 0$) of a Gaussian laser SW. $P = 7.8$ mW, $W_0 = 60$ μm and $\Delta/2\pi = 500$ MHz. (a) $v_z^{(i)} = 955$ ms^{-1} , $v_x^{(i)} = 0$. (b) $T_o = 1900$ K, $v_x^{(i)} = 0$. (c) $v_z^{(i)} = 955$ ms^{-1} , $\alpha_0 = 0.16$ mrad.

transverse positions are also shown. The atoms which enter the SW lens far from its axis experience higher order terms in the expansion of $U(X, Y, Z)$ in X . Consequently, their trajectories significantly deviate from simple paraxial behavior. The atom flux is broadened by the presence of spherical aberration. The width and the contrast evaluate to $w \simeq 1$ nm and $\zeta \simeq 71$, respectively.

Chromatic aberration

In reality, however, monoenergetic and non-divergent atom beams are still not feasible. This means that further structure broadening arises due to a spread in velocities of thermal atoms. Supposing $v_x^{(i)} = 0$ and $v_z^{(i)}$ satisfying Eq. (2.9), the effect of chromatic aberration further smears the feature as seen in Fig. 2.3(b). This is because atoms from different regions of the Maxwell-Boltzmann distribution have different interaction times with the SW field. The flux characteristics are $w \simeq 4.5$ nm and $\zeta \simeq 13.6$.

Atom beam divergence

By setting $v_z^{(i)} = 955$ ms^{-1} and generating $v_x^{(i)}$ according to the Gaussian distribution from Eq. (2.10), the effect of atom beam divergence is studied. In Fig. 2.3(c) the resulting flux is shown for $\alpha_0 = 0.16$ mrad, corresponding to the smallest divergence ever reported for a laser-collimated chromium beam [5]. The rays (trajectories) with

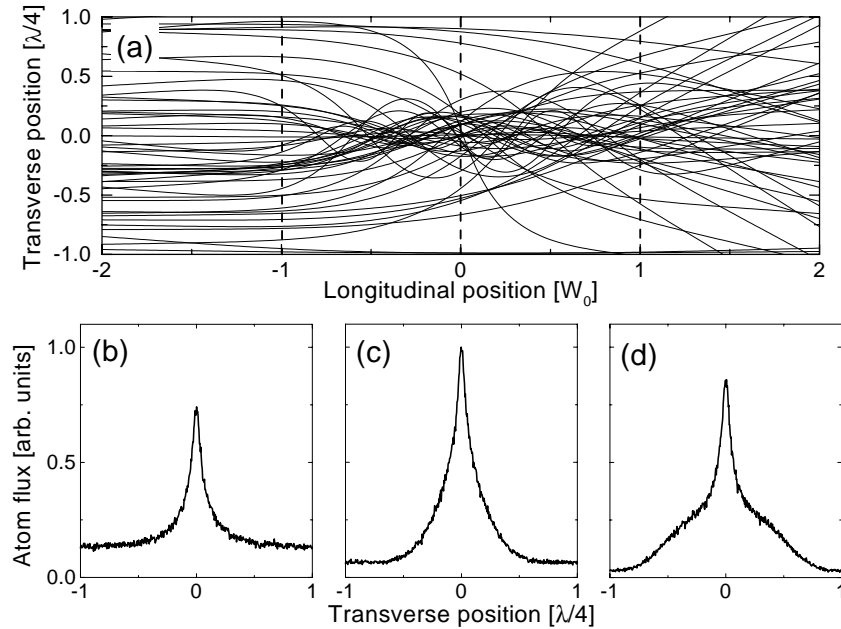


Figure 2.4: Channeling of a chromium beam in a Gaussian laser SW. $P = 30$ mW, $W_0 = 60 \mu\text{m}$ and $\Delta/2\pi = 500$ MHz. (a) 50 calculated atomic trajectories with random initial conditions ($T_o = 1900$ K, $\alpha_0 = 0.16$ mrad) and the resulting atom flux distributions at (b) $Z = -1$, (c) $Z = 0$ and (d) $Z = 1$.

a large inclination angle to the lens axis also violate the paraxial approximation. The focal distribution is hence blurred. The width and the contrast are $w \simeq 6.7$ nm and $\zeta \simeq 19.6$, respectively.

Channeling

An important issue concerns the stability of the atom flux distribution with respect to the longitudinal position Z . This gives a hint of how sensitive the feature shape is to any possible Z misalignment of the sample manipulation system. Since the atomic velocity distributions are fairly broad, there will always be a higher trajectory density near the axis of the SW lens than anywhere else. This fact is referred to as the channeling effect. It is demonstrated in Fig. 2.4(a) in which 50 random trajectories are seen to concentrate near the SW axis ($P = 30$ mW) across a relatively large Z interval. The calculated flux distributions at three different positions, $Z = -1$, 0 and

1, are shown in Figs. 2.4(b), (c) and (d), respectively. Even though the flux profile changes quite dramatically across the laser beam, the Z positioning of the substrate is not extremely critical in order to achieve a nanostructured surface.

2.1.3 Laser and atom beam parameters

Analytical approximation

To study the effect of the laser parameters – the laser power P , the detuning Δ and the beam waist W_0 – on the achievable atom flux widths, we first go back to a more general discussion on the atom-optical properties of a SW light field as presented by McClelland [2]. We note that in an experiment Δ and W_0 are more difficult to change than P . Therefore, explicit calculations are carried out only for different values of P . The choice of Δ and W_0 is motivated by giving general, but approximative, arguments.

For the saturation parameter $p_0 \ll 1$ (large Δ and/or small I_0), the optical potential $U(x, y, z)$ from Eq. (2.1) is approximated by [see Eq. (1.11)]

$$U(x, y, z) = \frac{\hbar\Gamma^2}{8\Delta} \frac{I(x, y, z)}{I_S}. \quad (2.12)$$

Using this simplification, the paraxial focus location f of a thin Gaussian SW atom lens is evaluated to

$$f = \frac{1}{2\pi^2\sqrt{2\pi}} \frac{\lambda^2 E_0}{W_0 U_0} \quad (\text{thin lens}). \quad (2.13)$$

In the immersion lens regime an analytical solution for a Gaussian SW no longer exists. A numerical approach should be adopted. For a step-like laser beam, however, Eq. (2.6) can be used to derive the focal length of an immersion lens,

$$f = \frac{\lambda}{4} \sqrt{\frac{E_0}{U_0}} \quad (\text{immersion lens}). \quad (2.14)$$

The contribution of the chromatic aberration to the atom flux width w can be estimated using a simple argument. As discussed above, this effect arises due to a spread in the longitudinal velocities v_z and thus in the total energies E_0 and, consequently, in the saturation parameter a . The focal distribution is blurred due to the trajectory error δw which arises because of a variation in the focal length δf . Therefore,

$$\delta w \simeq \phi \delta f = -2\phi a \frac{df}{da} \frac{\delta v_z}{v_z}, \quad (2.15)$$

where ϕ is the inclination angle of the trajectory at the focus position.

The effect of the atom beam divergence α_0 on the resulting flux width can be estimated based on an analogy with optical imaging. An object at a position z_o in

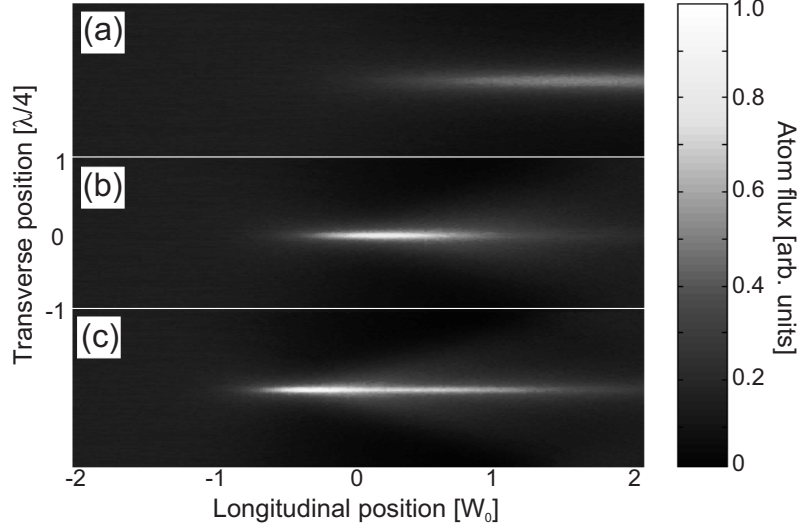


Figure 2.5: Simulated atom flux distributions for (a) $P = 2$ mW, (b) $P = 7.8$ mW and (c) $P = 30$ mW. $\Delta/2\pi = 500$ MHz, $W_0 = 60$ μm , $T_o = 1900$ K, and $\alpha_0 = 0.16$ mrad.

the object plane is imaged by a positive lens with a focal length f nearly at the focal plane, provided $z_o \gg f$. The apparent size of this object is $\simeq z_o \alpha_0$. The image is demagnified by a factor f/z_o . The flux width w is thus additionally smeared by

$$\delta w \simeq f \alpha_0. \quad (2.16)$$

It is now possible to study qualitatively the feature broadening δw in terms of the laser parameters P , Δ and W_0 . While for a thin lens $\delta w \propto W_0 \Delta / P$, for an immersion lens $\delta w \propto W_0 \sqrt{\Delta / P}$. The conclusion for both these regimes is that the better the focusing of the laser beam the narrower the feature. Also, the higher the laser power P the smaller the minimum atom flux width. Considering the detuning Δ we note that the larger it is, the more Eqs. (2.1) and (2.12) tend to be alike. In addition, the structure width is increased for a larger Δ . To compensate for this, P can be increased. Some restrictions apply due to the experimental geometry and available laser powers. Therefore, in practice a compromise has to be reached when choosing appropriate Δ and W_0 . The choice of $\Delta/2\pi = 500$ MHz and $W_0 = 60$ μm made above is very reasonable.

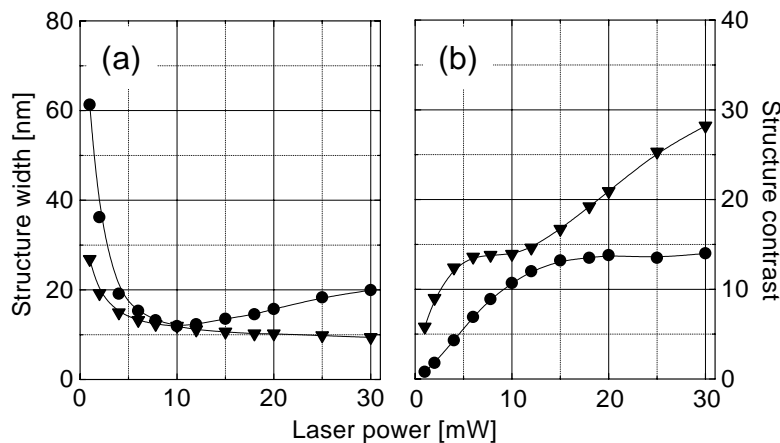


Figure 2.6: Structure width (a) and contrast (b) as functions of the laser power for all other simulation parameters identical with those of Fig. 2.5. The minimum value of the width and the maximum value of the contrast (triangles) as well as their values at $Z = 0$ (circles) are shown.

Explicit calculations

To model the atomic behavior in a Gaussian laser SW more accurately, explicit simulations were performed in order to determine the influence of P on the structure quality. In Figs. 2.5(a), (b) and (c) the calculated flux distributions are presented for $P = 2$ mW, 7.8 mW and 30 mW, respectively, and $\alpha_0 = 0.16$ mrad. It is seen that with increasing P the SW focus moves towards the atom beam source and the minimum flux width decreases. In addition, the higher the laser power the more pronounced the channeling effect.

The atom beam is partially insensitive to the initial conditions due to the channeling. Still, the flux width and/or the contrast can strikingly depend on the position across the SW. Since a very fine focus is the main goal in almost all laser-focused atomic deposition efforts, the question is what laser power to use to minimize the width w and/or to maximize the contrast ζ . These parameters are shown in Figs. 2.6(a) and (b), respectively, as functions of P (from 1 mW to 30 mW). The circles represent these quantities measured at $Z = 0$. The triangles show their overall “ideal” values – minimum w and maximum ζ , at appropriate longitudinal positions (which need not coincide). The “ideal” width and contrast improve with increasing P , though the former almost saturates. Moreover, it is not feasible to move the focus out of the beam (lower P) and to enter the thin lens regime. Both w and ζ degrade substantially and the focal distribution smears out for very low laser powers. In con-

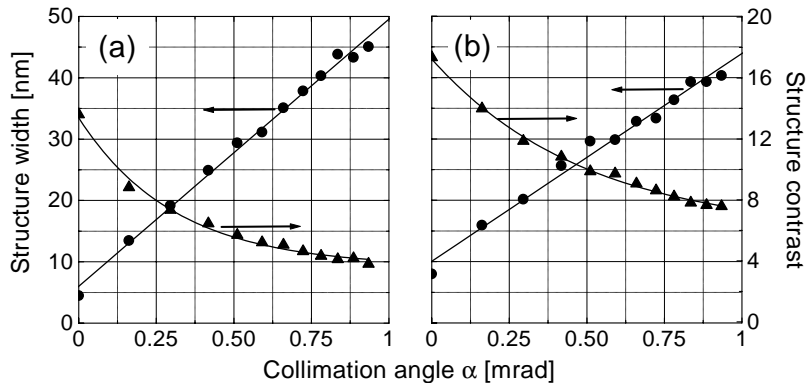


Figure 2.7: Structure width (circles) and contrast (triangles) as functions of the transverse collimation angle α_0 for $\Delta/2\pi = 500$ MHz, $W_0 = 60$ μm , $T_o = 1900$ K, and for (a) $P = 7.8$ mW and (b) $P = 20$ mW. The widths are fitted to a line and the contrasts to an exponential decay.

trast, these quantities measured at the laser beam center exhibit different trends. Initially, for increasing P the width rapidly decreases to its minimum value of 12 nm at 10 mW. Note that, when compared with the paraxial approximation, a slight over-focusing is required to achieve the narrowest focal distribution. For $P > 10$ mW, w slowly increases, the focus is broadened. On the other hand, the contrast increases with increasing P , reaching a value of 10 at 10 mW. For powers higher than 20 mW it saturates at $\zeta \simeq 14$.

The importance of a high degree of collimation of atom beams for laser-focused deposition is the most limiting requirement from the point of view of possible applications of this technique. Even a relatively small residual divergence smears the focal distribution quite considerably. To show this, the atom flux distribution at the laser beam center was explicitly calculated for collimation angles α_0 ranging from 0 to 0.95 mrad. The resulting flux widths and contrasts are presented in Figs. 2.7(a) and (b) for laser powers $P = 7.8$ mW and 20 mW, respectively. It is seen that the dependence of w on α_0 qualitatively resembles Eq. (2.16). The atom flux at the laser beam center is blurred for $P = 20$ mW as the paraxial focal plane is in the front of the image plane. The slope of the linear fit to the calculated widths from Fig. 2.7 is larger for $P = 7.8$ mW than for $P = 20$ mW. At the same time, for $\alpha_0 < 0.25$ mrad the focusing is better when $P = 7.8$ mW. For larger α_0 , it is better to use 20 mW. This is due to the channeling phenomenon. In addition, the contrasts for $P = 20$ mW are better than for $P = 7.8$ mW. The origin of these observations becomes clearer when confronting also Figs. 2.5 and 2.6.

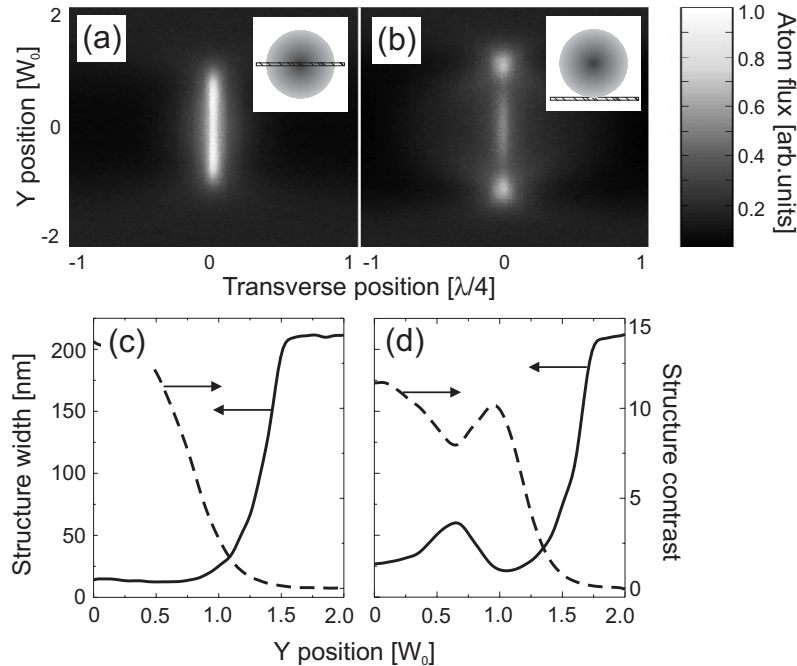


Figure 2.8: Chromium line profiles for $P = 20$ mW, $\Delta/2\pi = 500$ MHz, $W_0 = 60$ μm , $T_o = 1900$ K and $\alpha_0 = 0.16$ mrad at (a) $Z = 0$ and (b) $Z = 1$. The structure width (solid lines) and contrast (dashed lines) are shown as functions of Y at (c) $Z = 0$ and (d) $Z = 1$. The insets show alignment of the laser beam with respect to the substrate surface.

2.1.4 Line shape

All simulations presented so far were calculated in the plane $Y = 0$ where the Gaussian laser intensity reaches its maximum. Moving away from this plane to either negative or positive Y values would clearly affect the calculated atom flux profiles $f(X, Y, Z)$. Effectively, the farther away from the laser beam center the atoms are, the lower the optical intensity they are exposed to. Studying the flux shape as a function of Y is therefore equivalent to examining the role played by the laser intensity.

At $Z = 0$ and $Y = 0$ the smallest width for $W_0 = 60$ μm and $\Delta/2\pi = 500$ MHz was seen at $P = 10$ mW [Fig. 2.6(a)]. This corresponds to a laser intensity $I_0 \simeq 7.1 \times 10^6$ Wm^{-2} . Therefore, for an incident traveling laser power $P = 20$ mW the narrowest atom flux at $Z = 0$ should be located at $Y \simeq -0.6$ and 0.6 , and not at $Y = 0$. This is due to the fact that Eq. (2.1) includes only $I_0 \propto P/W_0^2$, and not

P and/or W_0 separately. Thus, the atom flux can be modulated quite substantially along Y .

Figs. 2.8(a) and (b) show the atomic distributions calculated at final longitudinal positions $Z^{(f)} = 0$ and 1, respectively, for $P = 20$ mW and Y ranging from -2 to 2. The contrast and width (as functions of Y) corresponding to these two cases are presented in Figs. 2.8(c) and (d), respectively. It is seen that the atom flux is more uniform for $Z^{(f)} = 0$ than for $Z^{(f)} = 1$. While at $Z^{(f)} = 0$ the atoms are trapped in the SW potential within a relatively large Y interval, at $Z^{(f)} = 1$ the atoms moving off the laser beam axis do not experience a considerable force after reaching a certain longitudinal position Z . At large distances Y the calculated flux widths saturate at about 213 nm ($\simeq \lambda/2$). This is due to the periodic boundary conditions applied in the simulations. The atom flux modulation was no longer detected.

We note that behavior similar to what is seen in Fig. 2.8 was already reported in experimental chromium studies which were in qualitative agreement with the semi-classical calculations [6]. For applications of laser-focused deposition it is essential to know how uniform the nanostructured array is along Y and how the results of, for example, *in vacuo* far field optical measurements (that have an access to only large scale average properties) might be affected. Probably the most straightforward recipe which allows for an increase of the uniformity scale along Y makes use of elliptical laser beams where the $1/e^2$ radius in the Y direction can be made considerably larger than the one along Z .

2.1.5 Towards realistic beams

An atom beam consisting of only two-level atoms moving in a conservative Gaussian SW optical potential was assumed above. The obtained results are indeed illustrative and the presented reasoning allows for a fast estimation of what can be expected in a particular parameter configuration. However, to get an even better agreement with reality, more details should be incorporated into the model. Here, we consider only the problems that can be treated within the semiclassical approach. These are: velocity-dependence of the dipole force, magnetic sublevel structure in the ground state of ^{52}Cr , presence of other chromium isotopes not affected by the laser SW, diffraction of the laser beam on the substrate surface.

Velocity-dependent force

The first-order velocity-dependent term $F_D(\mathbf{R})$ [7],

$$F_D(\mathbf{R}) = \frac{ap_0G(\mathbf{R})}{W_0} \sqrt{\frac{2E_0}{M_a}} \times \frac{I_S/I_0[1 - p_0G(\mathbf{R})] - 2p_0G^2(\mathbf{R})}{\Gamma[1 + p_0G(\mathbf{R})]^3} \tan^2(2\pi X) \frac{dX}{dZ}, \quad (2.17)$$

where $\mathbf{R} = (X, Y, Z)$, is added to the right hand side of Eq. (2.3). This term accounts for the dissipative nature of the atom-optical interaction. We note that $F_D(\mathbf{R})$ from Eq. (2.17) is expressed in transformed units in order to achieve compatibility with Eq. (2.3). $F_D(\mathbf{R})$ changes sign when switching from positive to negative values of a ($\propto \Delta$). In addition, $F_D(\mathbf{R})$ is a heating force at some locations in the laser beam and a cooling force at other ones. For conditions typically encountered in laser-focused atomic deposition $F_D(\mathbf{R})$ is only a small correction to the dominating conservative force.

Magnetic sublevel structure

The fact that chromium atoms exhibit a magnetic sublevel structure in their ground state ($J = 3$, $m = 0, \pm 1, \pm 2, \pm 3$) should also be taken into consideration. These sublevels have different interaction strengths with the SW field and also different occupation numbers. An approximate way to treating this problem relies on calculations of the atom flux distribution for each sublevel [6]. Then, to obtain the resulting chromium flux these individual distributions have to be averaged with weighting factors equal to the sublevel populations. How a particular sublevel couples to an electromagnetic field is given by the square of the Clebsch-Gordan coefficient $C_{m_1 m_2}$ for the associated $\Delta m = m_1 - m_2$ transition (1 – ground state, 2 – excited state). Assuming a SW created from two co-linearly polarized traveling waves, the only allowed transitions are those with $\Delta m = 0$. In this case, the strengths are $4/7$ for $m = 0$, $15/28$ for $m = \pm 1$, $3/7$ for $m = \pm 2$ and $1/4$ for $m = \pm 3$. To simulate the atomic trajectories for atoms in a given m -sublevel, the only required adjustment is the transformation $I_0 \rightarrow |C_{mm}|^2 I_0$ in Eq. (1.4).

The problem is to choose the sublevel populations. There is not much known about the population of different sublevels for chromium atoms leaving a laser molasses beam. The choice is thus essentially arbitrary. We follow Anderson *et al.* [6]. The probability that a chromium atom leaves the molasses beam in a particular sublevel is 0.2083 for $m = 0$ and $m = \pm 1$, 0.1459 for $m = \pm 2$, and 0.0417 for $m = \pm 3$. For this distribution in the ground state, we can estimate the best focusing power P for a substrate located at the laser beam center and for the laser beam parameters left unchanged ($\Delta/2\pi = 500$ MHz and $W_0 = 60 \mu\text{m}$). The fact that the most populated sublevels couple to the SW field with a strength of roughly 0.5 indicates that $P \simeq 2 \times 10 \text{ mW} = 20 \text{ mW}$ [see Fig. 2.6(a)] is required to minimize the atom flux width.

Isotopic contribution

The chromium beam contains 16.2% isotopes which do not couple to the molasses laser (see Sec. 1.3). It depends on the experimental geometry on what fraction of these

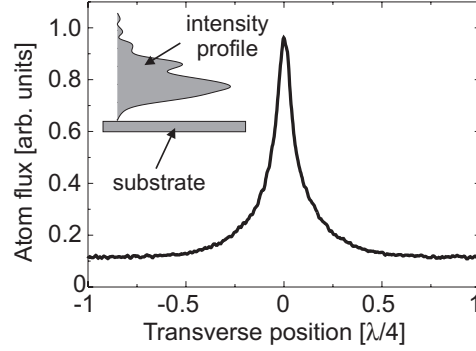


Figure 2.9: Generalized chromium flux. $P = 20$ mW, $\Delta/2\pi = 500$ MHz, $W_0 = 60$ μm , $T_o = 1900$ K, and $\alpha_0 = 0.16$ mrad. The inset shows the laser beam profile diffracted on the substrate surface. This was calculated by C.C. Bradley at NIST (for more details, see [6]).

isotopes contributes to the uniform background. In the worst case scenario all of them will. This happens when the distance between the laser cooling and focusing beams is short, so that the high angular divergence of these isotopes does not separate them from the dominant isotope ^{52}Cr . If this distance is long, however, the background flux can be reduced considerably. We accept here the worst case of 16.2% of isotopic background.

Laser beam diffraction

Another effect that has to be taken into account concerns possible diffraction of the Gaussian laser beam on the substrate surface. The transverse laser intensity profile depends on the dielectric permittivity of the sample material. This can change even during the deposition when the chromium film thickness increases. The diffraction phenomenon influences the feature shape only slightly. This was checked in our simulations by using higher order Gauss-Hermitian laser beams (TEM_{01} , TEM_{02} , and TEM_{03}) with both the laser power P and the beam radius W_0 kept constant. Nevertheless, in the following a totally reflecting surface is assumed. The calculated diffracted intensity profile is shown in the inset of Fig. 2.9 for an incident Gaussian laser beam with $W_0 = 60$ μm .

Laser-focused chromium flux

Including all the above mentioned contributions, the chromium flux as calculated for $P = 20$ mW, $\Delta/2\pi = 500$ MHz, $W_0 = 60$ μm , $T_o = 1900$ K, and $\alpha_0 = 0.16$ mrad is

shown in Fig. 2.9. Since this profile represents the initial flux of atoms striking the surface, its width and contrast dictate the “ultimate” values achievable in a process with the given laser parameters, provided the surface atoms do not interact with each other. In our case, Fig. 2.9 shows these “ultimate” values to be a width $w = 13$ nm and a contrast $\zeta = 7$.

2.2 Surface growth

The nanolines observed in all experimental studies with chromium to date (see Sec. 4.3 and [6, 8–10]) have always been considerably broader than the theoretically predicted shapes, in spite of the fact that the substrate positioning and the laser parameters can both be controlled very well in an experiment. This suggests that surface growth phenomena play a significant role in these studies.

The problem of surface growth in MBE has attracted considerable research interest during the past two decades [11–14]. The motivation for these studies originates from their importance for both fundamental research and technological applications. The latter requires growth of high quality thin films or high contrast, high resolution, sub-micron structures that are used in nanoelectronic, optoelectronic and high density magnetic storage devices. The key issue in the physics of MBE is the determination of what processes control the growth of material during and after deposition. Adsorption, diffusion, detachment and desorption all generally can play a role in a given situation. The task is to ascertain which of these dominate, as this governs the growth mode and hence the quality of an epitaxially grown material. The important growth processes can be studied experimentally using several techniques [12–14]. For example, the motion of individual adatoms can be studied using a field ion microscope (FIM) or a scanning tunneling microscope (STM). Furthermore, surface growth kinetics can be measured with techniques such as low-energy electron diffraction (LEED) or reflection high-energy electron diffraction (RHEED).

In theoretical studies of surface growth, two different approaches have been developed [11]. The continuous approach relies on a solution to a partial differential growth equation. It sees the surface on a coarse-grained scale larger than the typical inter-atomic distance. Atomistic growth models, on the other hand, rely on Monte Carlo calculations of atom-by-atom deposition onto a fixed lattice of atom sites that are filled or left vacant according to a set of rules for bond formation and breaking. Separability of individual atomic-scale processes involved in the surface growth is the main advantage of this approach.

To elucidate the underlying physical processes that govern the shape of laser-focused nanostructures, their evolution can be studied theoretically during and after the deposition. The same framework as in MBE growth can be applied; however, *the unique property of a controlled, non-uniform atom flux distribution adds a new dimension to the problem.* In typical theoretical studies of MBE, statistical quantities

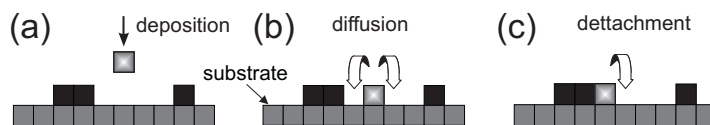


Figure 2.10: Schematic illustration of the TDS surface diffusion model. After each deposition event (a) the surface is allowed to relax via diffusion of single atoms (b) and/or via step-edge detachment (c).

(for example, surface roughness or island size distribution) are compared with corresponding measured quantities [11–14]. For growth of laser-focused nanostructures, the shape of the nanostructure itself depends on the growth properties, and comparison can be made between theory and experiment on this more readily measurable quantity. Thus studies can be carried out akin to earlier research in which corrugated surfaces were allowed to relax [15], with the added capability that the patterning and growth are combined into a single, ultra-high vacuum (UHV) compatible process.

In this section, calculations of the growth of a laser-focused nanostructure are presented. The goal is to examine the effects of growth and diffusion phenomena. Starting with the laser-focused atom flux calculated within the semiclassical trajectory tracing approach (Fig. 2.9), three different atomistic diffusion and growth models are applied and the resulting profiles are examined. It is demonstrated that within the models used, the nanostructure shape is strikingly sensitive to the kinetic parameters and the deposition time. These results suggest that growth studies of laser-focused nanostructures under UHV conditions will show strong dependence on deposition rates and surface temperatures. While ideally these results should be compared with experimental results, all experimental studies to date have been carried out in high-vacuum conditions ($\sim 10^{-6}$ Pa [10^{-8} mbar]), and so measured profiles are very likely to be influenced by contamination such as oxidation. Such comparisons will have to await future experiments conducted in UHV.

2.2.1 Tamborenea-Das Sarma diffusion model

The first surface growth model applied here to laser-focused atomic deposition was introduced by Tamborenea and Das Sarma (TDS) [16]. It is schematically demonstrated in Fig. 2.10. In this model, the atoms are randomly deposited onto a one-dimensional substrate and stick only to the tops of already existing surface atoms. After each deposition event, the atoms having at maximum two nearest neighbors are allowed to break their bonds by a thermally activated process. After breaking its bonds, the atom hops to neighboring columns, provided that the initial site is as high as or higher than the final one. The diffusion ($n = 1$) and the step-edge detachment ($n = 2$) rates

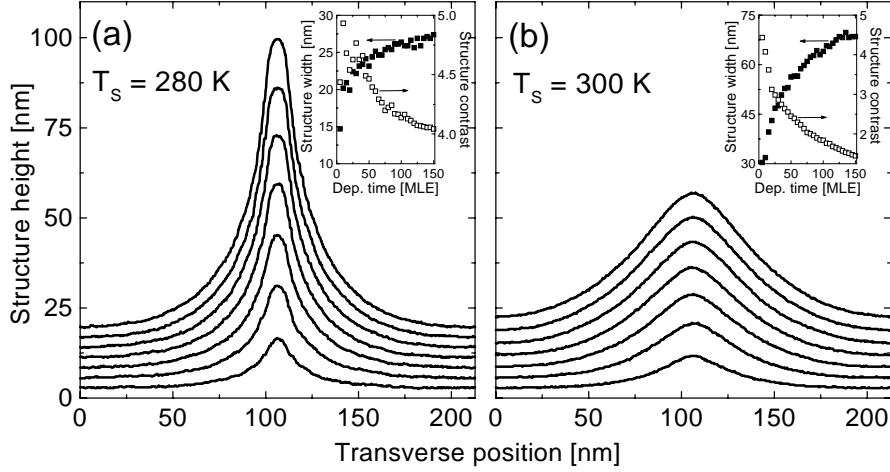


Figure 2.11: Calculated TDS diffusion profiles for successive deposition times from 20 MLE to 140 MLE at 20 MLE intervals. (a) Substrate temperature $T_S = 280$ K; (b) Substrate temperature $T_S = 300$ K. The evolution of the structure FWHM (solid squares) and contrast (open squares) with deposition times from 5 MLE to 150 MLE at 5 MLE intervals is shown in the insets.

$R_{n=1,2}$ follow an Arrhenius behavior characterized by a system-dependent activation energy, and are given by [16]

$$R_n = \frac{1}{R_d} \frac{k_B T_S}{\pi \hbar} \exp \left[-\frac{E_A + n E_B}{k_B T_S} \right], \quad (2.18)$$

where R_d is the deposition rate, T_S is the surface temperature, E_A is the “free atom” activation energy, E_B is the bond breaking energy and n is the number of nearest neighbors.

To examine the behavior of the TDS surface diffusion model deposition simulations have been performed for a wide range of values of R_1 and R_2 , assuming an incident flux with an average deposition rate of 0.02 monolayers (ML) per second, distributed according to the profile shown in Fig. 2.9. The shape of the resulting profile is examined after total average coverages ranging from 5 ML to 150 ML. Periodic boundary conditions are used, as justified by the intrinsic periodicity of the laser focusing process.

After examining a number of cases, the following qualitative observations are made. For $R_1 = 0$ and $R_2 = 0$, simple random deposition applies. The shape of the nanostructure mirrors exactly the atom flux distribution for any amount of total

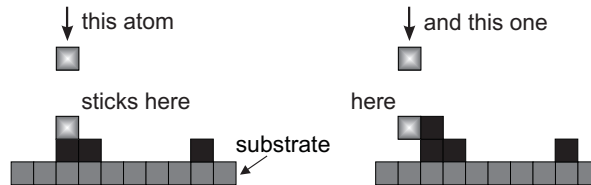


Figure 2.12: Schematic illustration of the BD surface growth model. Adsorption of atoms dominates the growth.

coverage. If R_1 is set to a large number ($\gg 1$) and R_2 equals 0, a flat terrace develops on top of the structure. The size of this terrace is dependent on the magnitude of R_1 . However, considerable profile broadening is not observed in this regime. A significant increase in the structure FWHM and a decrease in the contrast with increasing average coverage takes place only for $R_2 \gg 1$.

In Fig. 2.11 the nanostructure evolution is shown for a situation that might be typical for experiments with chromium atoms. We set $E_A = 0.55$ eV and $E_B = 0.1$ eV,⁴ the lattice spacing to 0.249 nm, and examine two different temperatures. Fig. 2.11(a) contains results for $T_S = 280$ K ($R_1 = 1154$, $R_2 = 18$), and Fig. 2.11(b) shows the behavior for $T_S = 300$ K ($R_1 = 7456$, $R_2 = 156$). In each figure, profiles are shown for total average coverage ranging from 20 ML to 140 ML, at 20 ML intervals. In the insets the evolution of the structure width and contrast from 5 ML to 150 ML is presented at 5 ML intervals. Comparing Figs. 2.11(a) and (b), we see that an increase of T_S by just 20 K causes a very pronounced change in the structure's resolution and contrast. Recalling Eq. (2.18), we see that small changes in activation energies for diffusion and detachment would also result in a similarly strong effect.

This striking sensitivity to temperature and activation energy illustrates that within the framework of the TDS model, growth phenomena can have a dramatic effect on the shape of laser-focused nanostructures. Such sensitivity suggests not only that schemes for nanofabrication must take this into account, but also that laser-focused deposition studies can be used to reveal important information about surface diffusion kinetic parameters. Since there is no diffusion at low temperature (< 250 K), measurements of the structure shape in this regime can be used to determine the incident flux. For higher temperatures, any measured change in the structure shape can be attributed to surface diffusion effects, allowing an in-depth investigation of these.

⁴The values chosen for E_A and E_B are essentially arbitrary, though they are not unreasonable for metal-on-metal homoepitaxy. The choice of the specific values used here was motivated by an attempt to model existing experiments. At temperatures near the experimental conditions these energies give a broadening of the profile that roughly matches the width seen in the experiments.

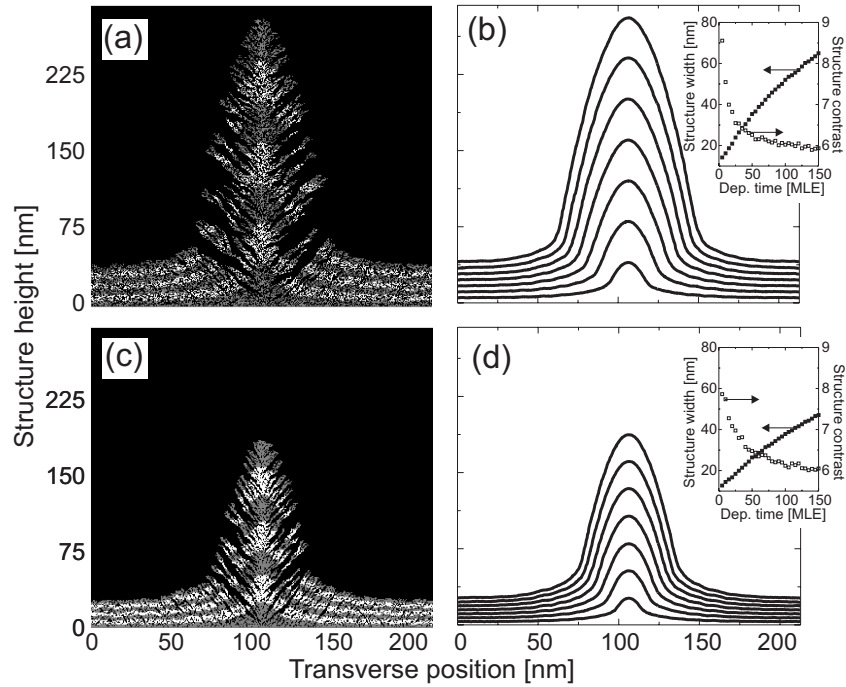


Figure 2.13: Calculated nanostructure shapes for (a) one BD run, (b) average of 100 BD runs, (c) one BDR run and (d) average of 100 BDR runs. Shown are successive deposition times from 20 MLE to 140 MLE at 20 MLE intervals. The insets in (b) and (d) present the evolution of the structure width and contrast with deposition times from 5 MLE to 150 MLE at 5 MLE intervals.

2.2.2 Ballistic deposition model

The second and third models implemented in these simulations are ballistic deposition models [11]. Once again, one-dimensional, simple cubic substrate geometry is assumed. In simple ballistic deposition (BD) the incident atom sticks to the first occupied site encountered, either directly below or laterally adjacent to it, and is subsequently not allowed to move (Fig. 2.12). In ballistic deposition with relaxation (BDR), the atom is allowed to relax to its nearest or next-nearest sites, the probability of movement being higher, the larger the coordination number of the new site. It should be noted that BD and BDR may not be realistic for describing MBE as they generally give rise to an unreasonably large number of voids and vacancies (especially for BD) [11]. Nonetheless, it is useful to study this type of growth because a

certain number of these defects do occur in some systems, particularly for rough surfaces or for growth with high flux rates and/or a significant concentration of surface impurities.

The results of BD and BDR simulations are shown in Fig. 2.13. As in Fig. 2.11, the nanostructure evolution during the deposition is shown for deposition times of 20 ML equivalents (MLE) to 140 MLE at 20 MLE intervals. The BD and BDR data in Figs. 2.13(a) and (c) are a result of a single simulation run, while averaging along 100 independent statistical runs was performed in order to obtain smooth curves as shown in Figs. 2.13(b) and (d). Comparing BD and BDR shapes with those of Fig. 2.11, it is clearly seen that the atomic growth mechanisms invoked in our simulations are reflected in the structure profile. Indeed, a significant difference is expected, because the two growth models belong to different universality classes [11]. TDS is a linear surface diffusion model [16], while BD and BDR belong to the Kardar-Parisi-Zhang (KPZ) universality class [17], with second order nonlinearity present in continuum versions of the model.

While the calculated structures for BD and BDR are similar, the average film thickness is different due to a different fractional volume of voids. In BDR atoms are allowed to move to their nearest or next-nearest sites to maximize the number of nearest neighbors. Allowing them to move more than once would result in a further collapse of voids and vacancies. The insets in both Figs. 2.13(b) and (d) show that the structure width increases as a function of the deposition time for both BD and BDR due to the strong lateral interaction between the atoms. This increase is faster for BD than for BDR. On the other hand, the contrast decreases with increasing deposition time, with both cases exhibiting the same trend. For low coverages (< 5 ML) the width measured for both of these models resembles the value of 13 nm from calculations of the atom flux. However, the low coverage contrast of about 8 is larger than the “ultimate” value of 7 derived from the atom-optically calculated flux. This increased contrast, which arises from a higher concentration of voids in the thicker part of the deposition, suggests that the real ultimate width and contrast might not only be dictated by the atom flux but also by surface growth effects. Such phenomena may play a crucial role in direct fabrication of nanostructures via atom optics.

2.3 Conclusions

Focusing properties of a SW atom lens were modeled in this chapter. The role of the laser and atom beam parameters was analyzed. Herein, we have learned what a successful experiment with chromium atoms requires. The model we have developed will serve as a valuable guide in our experimental endeavor.

We have also applied three different atomistic growth models to study the formation of a laser-focused nanostructure. We have shown that, within the models ex-

amined, the nanostructure profile depends strongly on the kinetic parameters and on the deposition time in our simulations. This suggests that laser-focused nanofabrication experiments performed in UHV will be useful in discriminating between different growth models.

As this work progresses a more thorough knowledge of the processes involved in laser-focused nanostructure fabrication will be gained, allowing growth of high resolution, high contrast, periodic nanostructures with a possible impact on a number of key technologies.

References

- [1] G.L. Timp K.K. Berggren, M. Prentiss and R.E. Behringer. Calculation of atomic position in nanometer-scale direct-write optical lithography with an optical standing wave. *J. Opt. Soc. Am. B*, 11:1166–1176, 1994.
- [2] J.J. McClelland. Atom optical properties of a standing-wave light field. *J. Opt. Soc. Am. B*, 12:1761–1768, 1995.
- [3] C. Cohen-Tannoudji. Atomic motion in laser light. In J.-M. Raimond J. Dalibard and J. Zinn-Justin, editors, *Fundamental Systems in Quantum Optics, Les Houches Lectures, Session LIII*, chapter 1, pages 1–164. North Holland, Amsterdam, 1990.
- [4] W.H. Press, B.P. Flannery, S.A. Teukolsky, W.D. Vetterling. *Numerical recipes in C*. Cambridge University Press, Cambridge, 1988.
- [5] R.E. Scholten, R. Gupta, J.J. McClelland, and R.J. Celotta. Laser collimation of a chromium beam. *Phys. Rev. A*, 55:1331–1338, 1997.
- [6] W.R. Anderson, C.C. Bradley, J.J. McClelland, and R.J. Celotta. Minimizing feature width in atom optically fabricated nanostructures. *Phys. Rev. A*, 59:2476–2485, 1999.
- [7] J.P. Gordon and A. Ashkin. Motion of atoms in a radiation trap. *Phys. Rev. A*, 21:1606–1617, 1980.
- [8] J.J. McClelland, R.E. Scholten, E.C. Palm, and R.J. Celotta. Laser-focused atomic deposition. *Science*, 262:877–880, 1993.
- [9] J.J. McClelland, R. Gupta, Z.J. Jabbour, and R.J. Celotta. Laser focusing of atoms for nanostructure fabrication. *Aust. J. Phys.*, 49:555–565, 1996.
- [10] U. Drodofsky, J. Stuhler, B. Brezger, Th. Schulze, M. Drewsen, T. Pfau, and J. Mlynek. Nanometerscale lithography with chromium atoms using light forces. *Microelectronic Engineering*, 35:285–288, 1995.

-
- [11] A.L. Barabási and H.E. Stanley. *Fractal Concepts in Surface Growth, 1st Edition*. Cambridge University Press, Cambridge, 1995.
 - [12] E.G. Seebauer and C.E. Allen. Estimating surface diffusion coefficients. *Progr. Surf. Sci.*, 49:265–330, 1995.
 - [13] S.-L. Chang and P.A. Thiel. Atomic-scale mechanisms of metal-on-metal growth. *Crit. Rev. Surf. Chem.*, 3:239–296, 1994.
 - [14] L.T. Wille, C.P. Burnester, K. Terakura, G. Comsa, and E.D. Williams, editor. *Mechanisms and Principles of Epitaxial Growth in Metallic Systems*, volume 528 of *Mat. Res. Soc. Symp. Proc.*, 1998.
 - [15] J.M. Blakely and H. Mykura. Surface self diffusion and surface energy measurements on platinum by the multiple scratch method. *Acta Metall.*, 10:565–572, 1962.
 - [16] P.I. Tamborenea and S. Das Sarma. Surface-diffusion-driven kinetic growth on one-dimensional substrates. *Phys. Rev. E*, 48:2575–2594, 1993.
 - [17] M. Kardar, G. Parisi, Y.-C. Zhang. Dynamic scaling of growing interfaces. *Phys. Rev. Lett.*, 56:889–892, 1985.

Apparatus

In this chapter we describe the design and construction of our apparatus for laser-manipulated deposition with chromium atoms. We base the constraints on the performance of our system on the modeling results obtained in the previous chapter.

3.1 Outline

Required performance

A laser power of at least a few tens of mW is required for efficient laser collimation of a thermal chromium beam and a similar amount for laser focusing. Therefore, considering the losses on different optical components, our laser system should deliver at least 100 mW. We must also be able to tune the laser frequency near the ${}^7S_3 \rightarrow {}^7P_4^o$ ${}^{52}\text{Cr}$ resonance at 425.55 nm. Moreover, we require the laser linewidth (including the frequency jitter) to be narrower than the natural linewidth of the resonance $\Gamma/2\pi \simeq 5$ MHz.

The deposition should eventually take place in a clean environment to achieve the aim of combining atom optics with surface science. Our vacuum system should thus be UHV-compatible. As we work on nanometer scale, we have to assure that the sample manipulation system and also the optics stay stable during the deposition process which might take anything from a few seconds to a few hours, depending on the average chromium film thickness required.

Experimental setup

Schematically, our apparatus is set up as shown in Fig. 3.1. A Spectra-Physics Millennia X – a diode-pumped Nd:YVO₄ (neodymium-doped yttrium vanadate) laser

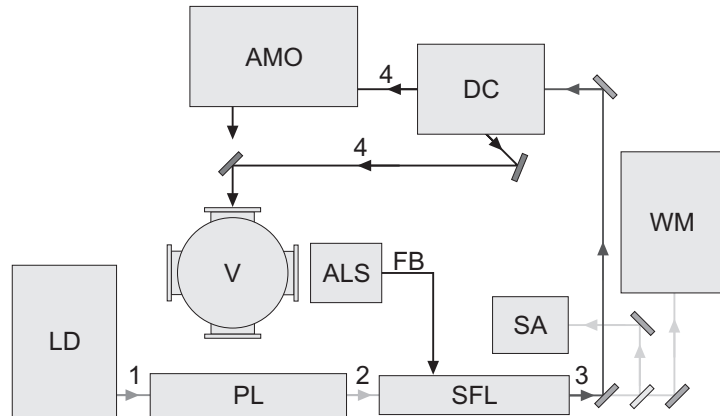


Figure 3.1: Schematic of our apparatus. LD – laser diodes and PL – pump laser (Millennia X). SFL – Ti:Sapph. single-frequency laser; SA – spectrum analyzer; WM – wavemeter; DC – doubling cavity; AMO – atom manipulation optics; V – vacuum system; ALS – system for atomic line stabilization; FB – feed-back signal for laser stabilization onto an atomic resonance. Laser beams: 1 – 800 nm; 2 – 532 nm; 3 – tunable around 850 nm; 4 – second harmonic generation of 3.

that is intra-cavity doubled with an LBO (lithium tri-borate) crystal – serves as a pump for a single-frequency Ti:Sapph. (titanium-doped sapphire) laser. This laser produces output in the near-infrared region of the optical spectrum at around 850 nm. The infrared laser beam is split into three beams. The first one is directed towards an LBO-based external enhancement doubling cavity. The second and third ones are respectively used to monitor the laser mode with a spectrum analyzer and the wavelength with a wavemeter. There are two blue beams (425 nm) exiting the doubling cavity. One of them is used for laser manipulation of atoms. The other one for stabilization of the laser frequency onto the chromium transition and monitoring the atom beam. Both these beams are directed onto the chromium beam inside the vacuum system.

Because of high stability requirements all parts of our system are rigidly connected to an optical table (Melles-Griot, 1.5×3 m, 4 pneumatic legs with three point leveling adjustment) and protected against dust with plastic sheets mounted on a frame. This frame supports a laminar flow box (Interflow) which is running continuously and keeps the system in a dust-free environment. The laboratory is air-conditioned at 20 °C.

In Sec. 3.2 we describe the optical part and in Sec. 3.3 the vacuum part of our system.

3.2 Optical part

In Sec. 3.2.1 a short review of optical resonators is provided. Then, we describe the Ti:Sapph. laser (Sec. 3.2.2), the doubling cavity (Sec. 3.2.3), the wavelength measurement system (Sec. 3.2.4) and the absolute stabilization of the laser onto the ${}^7S_3 \rightarrow {}^7P_4$ ${}^{52}\text{Cr}$ resonance (Sec. 3.2.5).

3.2.1 Resonators

An optical resonator is a device which allows light with only a distinct set of well-defined frequencies, or modes, to oscillate. This fact has important consequences in optics. For example, laser action is possible only due to this very idea.

We define a resonator at optical frequencies as a region of space restricted by two or more reflecting surfaces – mirrors. The resonator properties are dictated by the mirror characteristics and also by the chosen geometry. There are two classes of optical resonators: the so-called linear and ring cavities. In a linear cavity light back-reflects from the last mirror through all intermediate mirrors to the first mirror and a light SW builds up. In a ring light circulates across a closed optical path and no SW is created. The resonator length L is here defined as the distance of one round-trip to avoid writing different expressions for ring and linear cavities.

Free spectral range

The frequency interval between two adjacent supported longitudinal modes is called the free-spectral-range (FSR) and is given by

$$FSR = \frac{c}{L}, \quad (3.1)$$

where c is the *in vacuo* speed of light. Thus, $FSR \simeq 0.3$ GHz for a resonator with a length of 1 m. If a single-frequency wave with a wavelength λ and a frequency $\nu = c/\lambda$ is incident on a resonator it comes to resonance each FSR . The ratio $N = L/\lambda = \nu/FSR$ tells how many times a wavelength fits into the resonator. To change the resonance frequency by $\delta\nu$, the cavity length has to be changed by $\delta L = -\lambda\delta\nu/FSR$. Now, consider the following example: How stable should the length of a resonator ($L \simeq 1$ m) be in order to achieve a frequency stability of ± 0.5 MHz at 425 nm? The answer is $\delta L \simeq \pm 0.7$ Å. In a real system such a stability can be assured almost routinely.

Stability criterium

A resonator is called stable when paraxial optical rays stay confined in it forever. It is customary to evaluate the stability criterium on the basis of geometrical optics. For

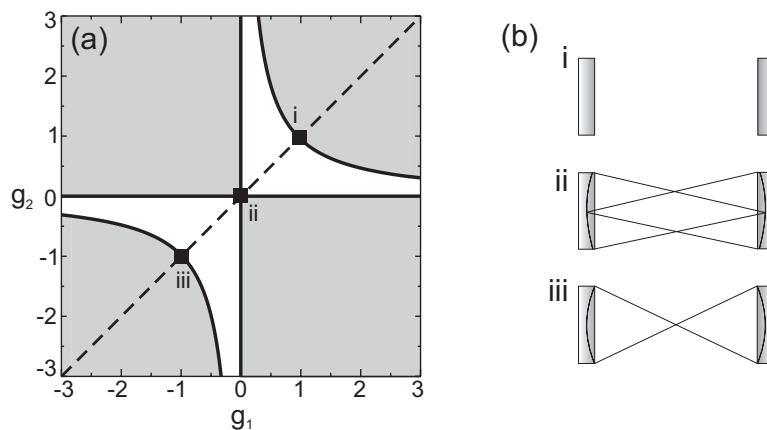


Figure 3.2: (a) Resonator stability diagram. Unshaded region represents stable resonators. All symmetrical resonators lie along the dashed line $g_1 = g_2$. (b) Symmetrical resonators: i. planar, ii. symmetrical confocal, iii. symmetrical concentric.

each linear system (such as a paraxial optical device) the output depends linearly on the input. In paraxial optics we choose the input and output to be two-dimensional ray vectors, \mathbf{v}_i and \mathbf{v}_o , respectively. The components of these vectors are the position and the angle of the ray at chosen input and output planes. These input and output vectors are related via a 2×2 matrix \mathbf{M} – the transfer matrix,

$$\mathbf{v}_o = \mathbf{M}\mathbf{v}_i = \begin{pmatrix} A & B \\ C & D \end{pmatrix} \mathbf{v}_i. \quad (3.2)$$

For an infinite system, such as a resonator, the input and output planes overlap. The rays stay confined forever when $|A + D|/2 \leq 1$ (provided $\det \mathbf{M} = 1$). This stability criterium is illustrated in Fig. 3.2(a) for two-mirror resonators for which the so-called g -factors are introduced; $g_1 = 1 + L/4r_1$ and $g_2 = 1 + L/4r_2$, where r_1 and r_2 are radii of curvature of the two mirrors, respectively. The resonators falling into the unshaded region of Fig. 3.2(a) are stable. The shaded region represents the resonators which are unstable. The resonators at the boundary between these two regions are conditionally stable. Any small deviation of the parameters can make them unstable. The stability criterium in fact means that the rays inside a resonator retrace themselves after an integer number of round trips. Interestingly, in all stable cases, more than one round-trip is needed. In Fig. 3.2(b) three examples of conditionally stable resonators are presented. These are the planar ($r_1 = r_2 = \infty$), symmetrical confocal ($r_1 = r_2 = -L/2$), and symmetrical concentric ($r_1 = r_2 = -L/4$) resonators, respectively.

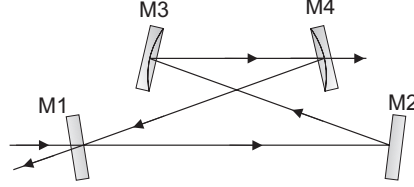


Figure 3.3: A four-mirror ring cavity.

Longitudinal modes

A wave inside a resonator is supported because of constructive interference; it is in phase with itself after successive round-trips. It is thus possible to enhance the electric field amplitude of an optical wave inside a cavity. Consider now a four-mirror ring resonator as shown in Fig. 3.3. Mirrors M1 and M4 are here used as input and output couplers, respectively. In order to be able to couple a wave into this resonator through M1, M1 has to have a non-zero intensity transmission $T_1 = 1 - R_1$. All other round-trip losses are associated with M2, M3 and M4, with possible misalignment and, eventually, with some intra-cavity elements such as a crystal, an etalon, a dust particle, etc. These other losses are here jointly expressed as a reflectivity R .

In the plane wave approximation the steady-state intra-cavity field E_i at the position of the M1 mirror is given by

$$E_i = i\sqrt{T_1} \left[\sum_{n=0}^{\infty} \rho^{n/2} \exp(-in\phi) \right] E_0 = i\sqrt{T_1} \frac{1}{1 - \sqrt{\rho} \exp(-i\phi)} E_0, \quad (3.3)$$

where E_0 is the incident field, ϕ is the phase-shift acquired by the cavity field in one round-trip and $\rho = R_1 R$. The field E_r that is reflected from the input coupler M1 then evaluates to

$$E_r = -\sqrt{R_1} E_0 - i\sqrt{T_1 R} \exp(-i\phi) E_i. \quad (3.4)$$

The optical intensities associated with E_i and E_r are respectively given by

$$I_i = T_1 \frac{1}{1 + \rho - 2\sqrt{\rho} \cos(\phi)} I_0, \quad (3.5)$$

and

$$I_r = \left[R_1 - 2T_1 \sqrt{\rho} \frac{\cos(\phi) - \sqrt{\rho} \cos(2\phi)}{1 + \sqrt{\rho} - 2\sqrt{\rho} \cos(\phi)} \right] I_0 + T_1 R I_i, \quad (3.6)$$

where I_0 is the incident intensity.

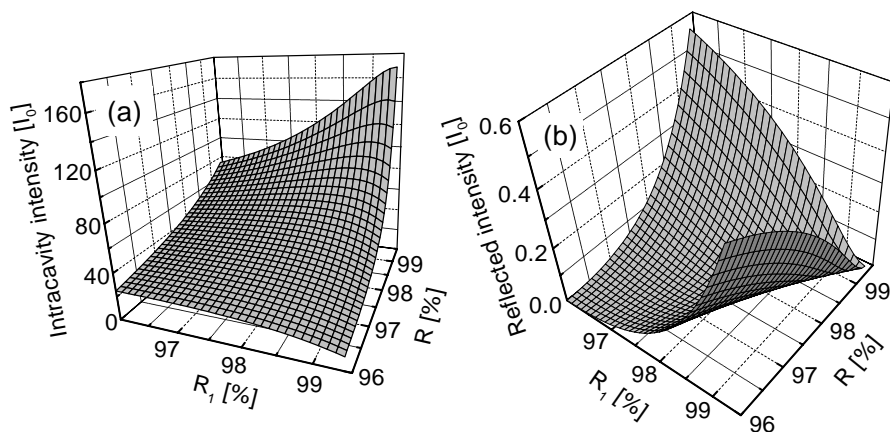


Figure 3.4: Calculated on-resonance intra-cavity (a) and reflected (b) intensities as functions of the input coupler reflectivity R_1 and the reflectivity associated with other intra-cavity losses R .

On-resonance intensities

In Figs. 3.4(a) and (b) the calculated on-resonance ($\phi = 0$) intra-cavity and reflected intensities, I_i and I_r , respectively, are shown as functions of R_1 and R . We see that the intra-cavity intensity can reach very high values, more than hundred times the intensity of the incident monochromatic wave I_0 , even for relatively modest values of R and R_1 . An important observation is that, for a given R , I_i first smoothly increases with R_1 . At $R_1 = R$ it reaches a maximum and, thereafter, starts to decrease. The physical reason for this behavior is that the gain that is due to the in-coupling cannot compete with the intra-cavity losses anymore. For $R = 100\%$, I_i is not a smooth function of R_1 and a singularity jump to $I_i = 0$ occurs at $R_1 = 100\%$. Considering I_r , it first decreases with increasing R_1 and then, after reaching $I_r = 0$, increases. Now, at a given R_1 , I_i is monotonic and increases with increasing R . In contrast, I_r first decreases, reaches $I_r = 0$ and then increases.

For a given input coupler, the cavity cannot be aligned properly by trying to minimize I_r . Of course, the cavity will be optimal when $I_r = 0$, but to this end R_1 should be selected properly and that is not an easy task.

Stabilization

It is often desirable to lock the length of a resonator to the frequency of the incident light wave or to the length of a reference cavity. An active control of the resonator

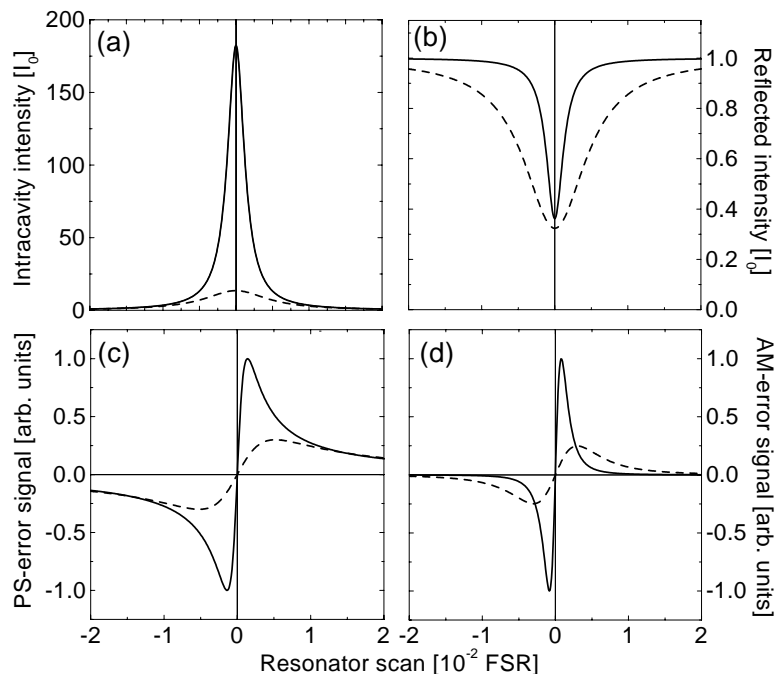


Figure 3.5: Calculated intra-cavity intensity (a), reflected intensity (b), PS-error signal (c), frequency derivative of (b) – AM-error signal (d) as functions of the resonator scan. $R_1 = 98.6\%$, $R = 99.65\%$ (solid line) and $R_1 = 98.6\%$, $R = 95\%$ (dashed line).

length is then required because mechanical and thermal instabilities cannot be avoided completely. In both cases, signals measured on the output or in the reflection are used. We show here what can be done.

Calculated I_i and I_r as functions of the cavity detuning are shown in Figs. 3.5 (a) and (b) for $R_1 = 98.6\%$ and $R = 99.65\%$ (solid line) and $R = 95\%$ (dashed line), respectively. Both I_i and I_r have a finite frequency width. To stabilize the resonator I_i or the intensity transmitted through the output coupler I_t can be kept at the maximum value by an active servo-control. Alternatively, I_r can be kept at its minimum value. However, the problem with such an approach is that when the cavity moves slightly off resonance, one cannot say whether it became shorter or longer. A method that results in a bi-polar signal which changes sign at resonance is required.

First, one might compromise and stabilize at the side of a fringe [1]. Also, the phase of the reflected electric field changes sign at resonance. If a Brewster plate was put into the cavity then only p -polarization of the electric field can become resonant.

Having an s -polarized reference in reflection, the reflected wave changes its polarization state (ellipticity) around the resonance. This ellipticity can be analyzed leading to a dispersion signal which crosses zero at resonance. This method is called polarization spectroscopy (PS) and is due to Hänsch and Couillaud [2]. The calculated PS dispersion curves for $R_1 = 98.6\%$ and $R = 99.65\%$ (solid line) and $R = 99.5\%$ (dashed line) are presented in Fig. 3.5(c).¹ The third method to getting a stabilization signal relies on taking a frequency derivative of I_r . This is possible when the incident wave is frequency modulated. The amplitude modulation (AM) signal is then monitored on I_r with a phase-sensitive detector resulting in curves as shown in Fig. 3.5(d). This approach is due to White [3]. The last method we mention here is called frequency-modulation (FM) spectroscopy. It was proposed by Pound [4] for microwave oscillators and extended to optical frequencies by Drewer *et al.* [5]. FM spectroscopy is a method capable of measuring absorption and dispersion features by detecting the heterodyne beat signal that occurs when the FM optical spectrum of the probe wave is distorted by the spectral feature which is in this case the cavity resonance.

We note that in our experiment the laser frequency is stabilized onto the side of a fringe of a reference cavity. The doubling cavity is held at resonance with the laser frequency using the PS-spectroscopy scheme.

Transverse eigen-modes

The final issue to be discussed in this section concerns the transverse eigenmodes of an optical resonator. Maxwell's equations can be solved with appropriate boundary conditions at the mirror surfaces. The result is that the transverse electric field profile of a supported mode can always be expressed as a linear combination of Hermite-Gaussian modes – the so-called transverse electro-magnetic modes (TEM). The lowest order mode TEM_{00} is a Gaussian beam, the next two ones are donut-type beams TEM_{01} or TEM_{10} , etc. The resonator geometry dictates the properties of the supported beam. If one would like to amplify the light intensity inside a resonator, one must mode-match the incident beam to the resonator mode. Furthermore, it should be mentioned that different TEM modes are resonant at different longitudinal resonator frequencies. This fact can be used when aligning a resonator such that only TEM_{00} survives.

Conclusions

We have briefly discussed optical resonators and some of their properties. To get the highest possible resonator performance it is important to understand the physics

¹The s -polarized reference field was in our calculations adjusted such that the PS-error signal [solid line in Fig. 3.5(c)] fits the experiment shown in Fig. 3.11(c).

behind these devices. When one attempts to use a resonator as a laser or an enhancement cavity or as a spectrum analyzer, the resonator must be carefully aligned. One should also take care that, if an excitation beam from outside is used, it must be reasonably well matched to the resonator geometry. For information complementary to our treatment of optical resonators and for more details about physics of these devices we refer to [6–11].

3.2.2 Single-frequency Ti:Sapphire laser

Laser physics

Light amplification by stimulated emission of radiation is commonly known as the lasing process. Any laser consists of three main components: a pump as the energy source; an active laser medium; and a feed-back system which is a resonator with an output coupler through which a small part of the intra-cavity radiation is transmitted. The active medium amplifies some of the cavity longitudinal modes. Having a cavity with $L = 1$ m and assuming a gain curve with a width of $\delta \simeq 1.5$ GHz (neon line broadening in a helium-neon laser), the number of modes which are supported is estimated to $\delta/FSR \simeq 5$. Some media, such as dyes or crystals like Ti:Sapph., can support many more modes. This fact is used in pulsed laser systems. A broad frequency spectrum corresponds to a short pulse in the time domain. A gain curve with $\delta = 15$ THz results in 5×10^4 longitudinal modes. Fixing the mutual phases of these modes by some mode-locking technique, very narrow pulses can be generated. For other applications, such as for our laser-focused chromium deposition experiments, a single frequency mode is required. All other modes must then be suppressed. Additional Fabry-Perot etalons (resonators) are put into the laser cavity. The general rule of thumb is that the thinnest resonator determines the FSR , while the resonator with the narrowest mode dictates the frequency width of the generated laser line. For more details on laser physics, see [6–10].

Schematic design

A schematic of our single-frequency laser is presented in Fig. 3.6. It consists of a four-mirror ring resonator and a Ti:Sapph. crystal as the active medium. The pump laser is a diode-pumped, frequency-doubled Nd:YVO₄ laser at 532 nm with up to 10.5 W output power (Spectra Physics Millennia X). A ring geometry is chosen because of two reasons. First of all, when the pump power is increased the laser power does not saturate as fast as in the linear geometry. Spatial hole burning is prevented because a SW does not build up in the cavity. Uni-directional operation is enforced by placing an optical diode (a Faraday rotator and a quarter wave-plate) into the cavity. Secondly, a ring is intrinsically more resistant to mode-hops. To ensure a stable single-frequency operation, a thin etalon and a thick etalon are both mounted

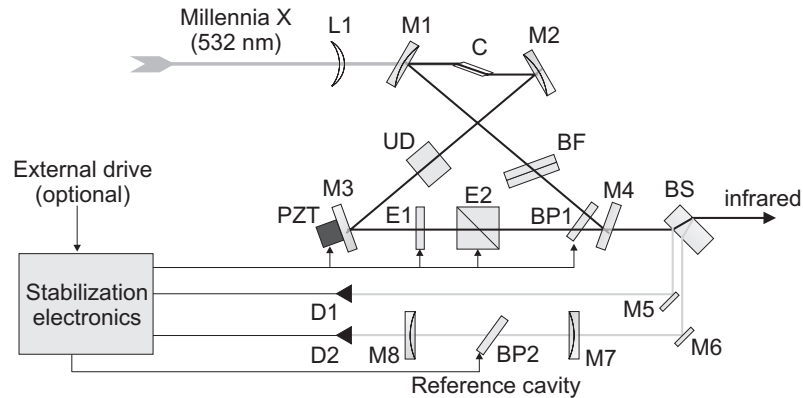


Figure 3.6: Schematic design of our single-frequency, tunable Ti:Sapph. laser. L1 – lens; M1, M2, M3 – high reflective dielectric cavity mirrors; M4 – output coupler; C – Ti:Sapph. crystal; UD – optical diode; E1 – thin etalon; E2 – thick etalon; BP1, BP2 – galvo-driven Brewster plates; BF – birefringent filter; PZT – piezo-electric transducer; BS – beam splitter; M5, M6 – folding mirrors; M7, M8 – reference cavity mirrors; D1 – normalization detector; D2 – reference detector.

into the laser. When properly aligned, they select only one frequency. A birefringent (Liot) filter is used to tune the laser wavelength. This intra-cavity element acts as a polarization rotator for all wavelength regions but one, for which it forms exactly a full-wave plate. Thus, by rotating it, one can tune the wavelength. This happens in relatively large steps. In our case 0.4 nm jumps take place. A better wavelength adjustment can be done by tuning the thin etalon. Each mode-hop of this etalon corresponds to 0.02 nm. Only ten such mode-hops can be carried out electronically (≈ 0.2 nm). It is therefore sometimes necessary to tune mechanically the thin etalon to approach certain wavelength regions. The last intra-cavity element is a galvo-driven Brewster-plate. Continuous scans up to 30 GHz are possible by simply rotating this plate inside the cavity. 30 GHz corresponds to roughly 0.07 nm at 850 nm. All etalons (including the Liot filter) must be aligned such that their modes overlap with each other and with the cavity mode. Only then an optimum operation of this laser is assured.

After our laser was built, a decision was made to upgrade a commercial laser (Coherent 899-01) to its single-frequency version (Coherent 899-21).²

²In the following, we do not report on our home-built laser. Its performance, however, is not worse than the performance of the 899-21 laser, though the cavity geometry is different. We did not actively stabilize this laser yet. Single-frequency operation was achieved by placing passive etalons into the cavity.

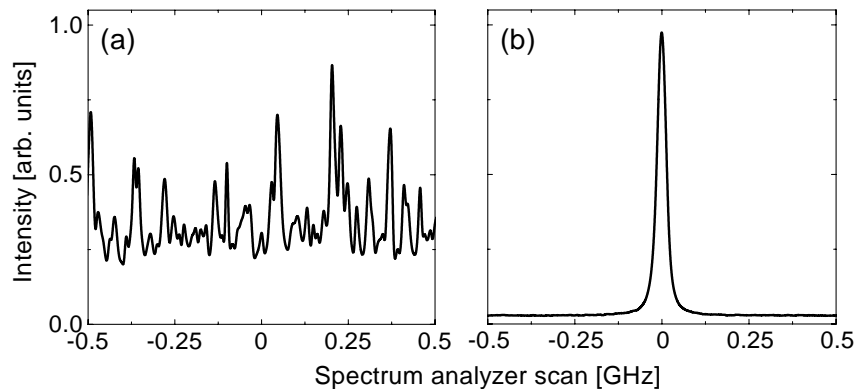


Figure 3.7: Longitudinal modes of our continuous-wave Ti:Sapph. laser measured with a 1.5 GHz optical spectrum analyzer. (a) Multi-mode operation. (b) Single-mode stabilized regime.

Electronic stabilization

The 899-21 laser is stabilized onto a fringe of a thermally-isolated reference cavity. The temperature of this cavity is kept above 40 °C to avoid possible disturbances due to room temperature fluctuations. The signals measured on two detectors – one measures the laser power and is called the normalization detector and the other one measures the light transmitted through the reference cavity – are divided in the 899-21 electronics and the result provides a measure of the laser frequency error relative to the reference cavity. The electronics then drives the thin and thick etalons, the Brewster plate and one of the mirrors that is mounted on a piezo-electric transducer (PZT). In this way short-term frequency stability is assured and high frequency noise is removed from the laser frequency. However, the reference cavity still slowly drifts and we have observed a long-term frequency change of ± 200 MHz in 10 hours. Sometimes, the thin etalon spontaneously mode-hops. The short-term stability is not better than ± 10 MHz (peak-to-peak) in 0.5 s. To get the laser frequency noise below these values, the reference cavity must be stabilized onto an absolute reference such as a dispersion signal measured on an atomic transition (see Sec. 3.2.5). This signal is then used to drive the Brewster plate mounted inside the reference.

Performance

In Fig. 3.7(a) multi-mode operation of our laser is demonstrated. Only the optical diode and the Liot filter were left inside the cavity. The spectrum was measured with a 1.5 GHz spectrum analyzer (a mirror distance 10 cm, $L = 20$ cm) and captured with a

digital oscilloscope. After inserting the thin and thick etalons and the Brewster plate and tweaking the alignment, single-frequency operation is established and the laser is locked to the reference cavity. The resulting laser spectrum is shown in Fig. 3.7(b).

In the multi-mode regime, a laser power of 1.9 W at 850 nm was measured with 10.5 W pump power. The threshold pump power for the system to lase was 2 W. The dependence of the generated power on the pump power was linear. In the single-mode stabilized regime, the threshold increased to 4.5 W and the highest ever generated power at 850 nm was 1.7 W (10.5 W pump). Routinely, however, the laser is run at about 1.5 W at the same pump power.

In the single-frequency operation, the laser wavelength is tunable from 800 nm to 900 nm. The laser linewidth is estimated to have an FWHM of certainly less than 1.13 MHz. A much broader spectrum is seen in Fig. 3.7(b) due to the convolution of the laser line with the spectrum analyzer response. Unfortunately, we do not have the means to measure the laser linewidth very accurately or to determine the response function of the analyzer. The above higher estimate is based on our measurements on the doubling cavity that are reported in the next section.

3.2.3 LBO-based doubling cavity

The infrared laser light at 850 nm must be doubled in frequency in order to get close to the ^{52}Cr resonance at around 425 nm. To this end we have built an external enhancement doubling cavity based on an LBO (lithium tri-borate) crystal.

Second harmonic generation (SHG)

An electromagnetic wave with an electric field $\mathbf{E}(\omega)$ propagating through a medium can induce a polarization $\mathbf{P}(2\omega)$ that radiates at the second harmonic of the fundamental frequency ω . $\mathbf{P}(2\omega)$ depends on the second-order nonlinear susceptibility $\chi^{(2)}(-2\omega; \omega, \omega)$ and on $\mathbf{E}(\omega)$ via

$$\mathbf{P}(2\omega) = \chi^{(2)}(-2\omega; \omega, \omega) : \mathbf{E}(\omega)\mathbf{E}(\omega). \quad (3.7)$$

$\chi^{(2)}$ is a material-dependent, third-rank tensor that has non-vanishing bulk components only in media without inversion symmetry. Furthermore, for an efficient SHG process the wave generated at 2ω must propagate in phase with the fundamental wave for a long enough distance inside the medium (phase-matching). We note that this condition actually requires the total momentum of the three photons involved in the process to be conserved. The wave-vectors must combine such that $\Delta k = k_1^{(\omega)} + k_2^{(\omega)} - k_3^{(2\omega)} = 0$. The refractive indices $n_1^{(\omega)}$, $n_2^{(\omega)}$ and $n_3^{(2\omega)}$, respectively, the three waves “see” must then satisfy the equality

$$n_1^{(\omega)} + n_2^{(\omega)} - 2n_3^{(2\omega)} = 0. \quad (3.8)$$

In anisotropic crystals this situation can be realized. The 2ω photon is always polarized in the direction that gives it the lower of the two possible refractive indices. For the photons at ω , there are two choices. They can have either the same polarization or they can have orthogonal polarizations. The former and the latter configurations are referred to as type I and type II phase-matching conditions, respectively. Which of these two types is the best to realize depends solely on the crystal. Careful control of the refractive indices is required in order to establish phase-matching.

In practice, two methods are used. The first one relies on angular tuning of the crystal and is referred to as critical phase-matching. This tuning is in the most general case of bi-axial crystals characterized by two angles: θ – the angle between the incident beam and the z -axis of the crystal; and ϕ – the angle between the incident beam and the x -axis in the xy -plane. The second method (non-critical phase-matching) is based on the fact that for some crystals the amount of birefringence is strongly temperature-dependent. Thus, the phase-matching condition can be fulfilled by tuning and accurately controlling the temperature.

SHG is not a very efficient process at low laser intensities. The SH yield $I(2\omega)$ is, far away from any resonances, proportional to the square of the fundamental intensity $I(\omega)$,

$$I(2\omega) \propto I^2(\omega). \quad (3.9)$$

Moreover, not the average intensity but the peak intensity dictates the conversion efficiency $\eta = I(2\omega)/I(\omega) \propto I(\omega)$. This fact can be best illustrated with the following example. Inserting a neutral density filter with a transmission of 50% into the fundamental beam results in a reduction of $I(2\omega)$ to 25% of its original value. However, when a mechanical chopper is used to bring the average power down to 50%, $I(2\omega)$ decays to 50%. This also means that a pulsed laser with a pulse duration of 100 fs and a repetition rate of 100 MHz is 10^5 -times more efficient than a continuous-wave (cw) laser with the same average power.

For more thorough and elaborate treatment of SHG we refer to [6, 7, 12–16].

External enhancement resonator

For an efficient SHG of a cw laser, the laser intensity and consequently the average optical power must be extremely high. There are two solutions at hand to enhance the cw light intensity. First, the intra-cavity laser light can be used.³ Secondly, an external enhancement resonator can be employed. The advantage of external doubling is that it does not require an optically active (nonlinear) crystal inside the laser cavity

³We have tried a challenging idea – to build a so-called self-frequency doubling laser based on a Cr:KTP (chromium-doped potassium titanyl phosphate). Spectroscopic properties of Cr:KTP indicated the possibility of using this material as an active medium. At the same time, it could be used as a nonlinear crystal for making SHG. However, we did not succeed. The reason is that Cr impurities drastically change the third-order nonlinearity and already at very modest cw pump powers we obtained self-phase modulation effects.

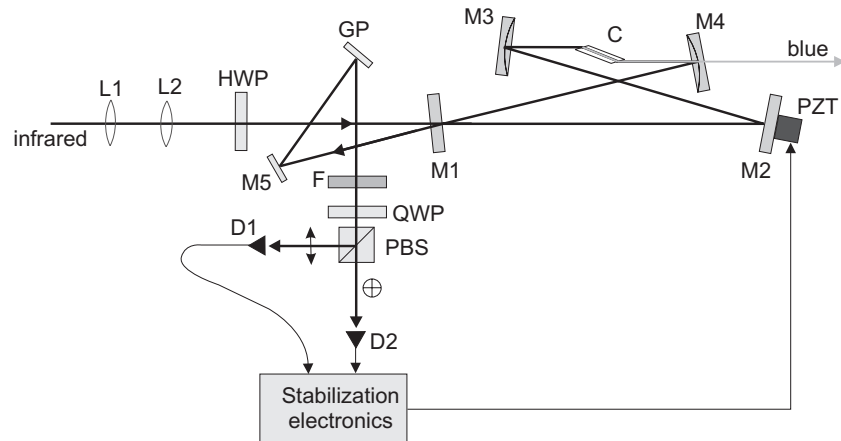


Figure 3.8: Schematic design: external enhancement doubling cavity. L1, L2 – mode-matching lenses; HWP – half-wave plate; M1 – input coupler; M2 – PZT mirror; M3, M4 – spherical mirrors; C – LBO crystal; PZT – piezo-electric transducer; GP – BK7 glass plate; M5 – folding mirror; F – neutral density filter (10%); QWP – quarter-wave plate; PBS – polarization beam splitter; D1, D2 – photodiodes.

itself and therefore does not disturb the laser performance. Several groups reported in the past on frequency doubling of a cw Ti:Sapph. laser in an external enhancement cavity [17–20].

Choice of the nonlinear crystal

There are at least four candidates for frequency doubling of 850 nm: BBO or beta-barium borate – BaB_2O_4 , KNbO_3 or potassium niobate, LBO or lithium tri-borate – LiB_3O_5 , and LiIO_3 or lithium iodate. For linear and nonlinear optical properties of these crystals, see [21, 22].

We have selected LBO because of its superior SH properties at the fundamental wavelength of 850 nm. Furthermore, LBO’s dielectric damage threshold is the highest from all known nonlinear crystals (18.9 GW/cm^2 at 1053 nm, 1.3 ns pulses). LBO can be phase-matched non-critically as both type I and type II from 900 nm to 1700 nm. At our wavelength of 850 nm, type I critical phase-matching is the most efficient with the resulting phase-matching angles $\theta = 90^\circ$ and $\phi = 26.9^\circ$. Because the crystal is to be used in a resonator, the losses due to light reflection on the surfaces must be minimized. An anti-reflection (AR) overcoat of the crystal faces is possible but there is always the danger of damage because of high cw intra-cavity powers. We

therefore use a Brewster-cut, phase-matched crystal (purchased from Casix, Inc.). Its dimensions are $4 \times 4 \times 10$ mm.

There is a problem associated with critical phase-matching. The fundamental and SH beams walk-off each other by a few tens of mrad. Also, the fact that LBO is a bi-axial crystal results in an astigmatic SH beam. This astigmatism can be corrected for, if necessary.

Schematic design

A schematic of our doubling cavity is shown in Fig. 3.8. It is a four-mirror ring resonator. The SH radiation is thus generated in the crystal in single pass. The fundamental beam is coupled into the resonator through a plane mirror M1 – an input coupler with an intensity transmission $T = 1.4\%$ at 850 nm. The next mirror M2 is also plane and is high-reflection (HR) coated for 850 nm. M2 is a relatively small mirror ($\varnothing 3$ mm, thickness 1.5 mm) mounted on a PZT (AE0203D08 piezoelectric stack, Thorlabs). The two last mirrors M3 and M4 are both spherical with a radius of curvature -10 cm. They are HR coated for 850 nm. Furthermore, M4 is a band-pass filter at around 425 nm. In this wavelength region its transmission $T > 94\%$. All mirrors were purchased from Laser Optik, GmbH.

We note that the positions and angles of all mirrors can be adjusted. M3 and M4 are mounted on differential screws rigidly connected to the cavity block and thus their alignment can be tweaked with a very high precision. The crystal is placed on a stage which allows for two angular adjustments and has all three translational degrees of freedom. Two lenses L1 and L2 (01LDX167/073 and 01LDK019/073, Melles Griot) are used for mode-matching of the fundamental beam into the doubling cavity. They are AR coated for 850 nm. The focal lengths of L1 and L2 are -5 cm and 10 cm, respectively. The separation between these lenses is roughly 6 cm and can be adjusted – L1 is mounted on a translator. The distance between L2 and M1 is roughly 17 cm. The distance between the laser and the doubling cavity is about 180 cm.

Mechanical design

To ensure mechanical stability we have designed a monolithic cavity block. In Fig. 3.9 this design is shown. The real geometry of the system and mutual distances between different components are readily obtained from this technical drawing. The monolithic block is made from high strength aluminum (BC-7, ALCOA) and is black-anodized to avoid any unwanted reflections.

Our device operates best in an air-conditioned laboratory. An estimation of thermal expansion of the cavity block indicated that temperature stability of ± 1 °C was required. The PZT cannot compensate for more than a few μm expansion. At maximum it allows for an M2 displacement of 10 μm . As the cavity elongates with

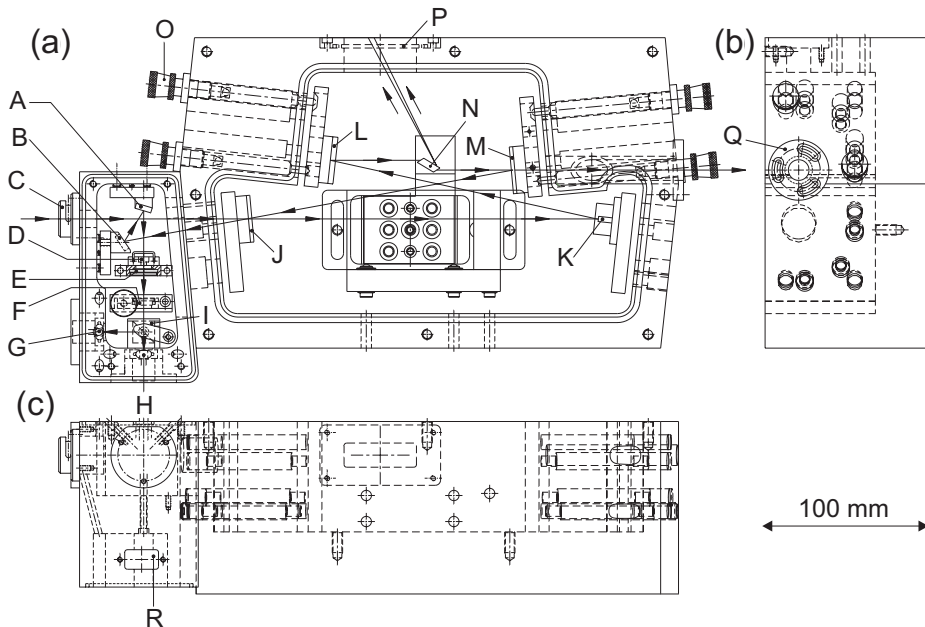


Figure 3.9: Design of the external enhancement doubling cavity. (a) Top view; (b) front view; (c) side view. A – BK7 glass plate; B – folding mirror; C – half-wave plate; D – band-pass color filter for 850 nm; E – neutral density filter (10%); F – quarter-wave plate; G, H – detectors; I – polarization beam splitter; J – cavity input coupler ($T = 1.4\%$); K – PZT-driven mirror; L, M – spherical mirrors; N – LBO crystal; O – differential screw; P – band-pass color filter for 425 nm; Q – Brewster window (BG39); R – standard ‘D’ connector.

increasing temperature, this drift must be compensated for. It is a relatively slow process and the electronic regulation scheme must take this into account.

Electronic stabilization

To lock the cavity length onto the laser frequency we implemented the Hänsch-Couillaud scheme (see Sec. 3.2.1 and [2]). To this end, a half-wave (HW) plate for the fundamental beam is mounted in front of M1. Only p -polarization is supported by the cavity because of the Brewster-cut crystal. A small non-resonant s -component is obtained by rotating the HW-plate slightly. This s -component serves as a reference for the stabilization unit. The incident beam is reflected from M1 onto an aluminum-coated mirror and then onto a glass plate with a mat back-face. The beam intensity

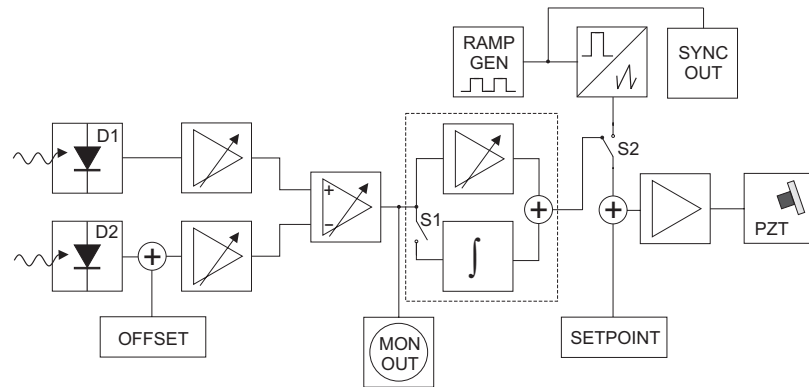


Figure 3.10: Regulating electronics for the doubling cavity. D1, D2 – photodiodes; S1, S2 – switches; OFFSET – dc-offset; MON-OUT – signal monitor; PZT – piezo-electric transducer; SET-POINT – PZT set-point (dc-voltage); RAMP-GEN – ramp generator for cavity scan; SYNC-OUT – synchronization output for the oscilloscope external trigger.

is herewith reduced to reasonably low levels. Still, a neutral density filter ($T = 10\%$) is used to reduce this intensity further. The optics for getting a dispersion signal around a cavity resonance consists of a quarter-wave (QW) plate and a polarization beam splitter (PBS). The QW-plate axis is at an angle of 45° with respect to the polarization of the infrared laser beam reflected at resonance. In this configuration, the polarization ellipticity is measured. Two detectors D1 and D2 (OSD 1-3 photodiodes, Centronic) register the signals. The position of these two photodiodes (in the plane perpendicular to the laser beam) can be adjusted. The difference between the signals detected on D1 and D2 is a measure of the ellipticity.

In Fig. 3.10 our electronic regulation scheme is schematically depicted. First, the signals measured on D1 and D2 are amplified and an offset, should it be necessary, can be introduced. Second, a difference signal is taken and again amplified. Then, the fast signal changes are processed in the proportional (P) band and slow drift in the integral (I) band of a PI-regulator. The signal is again amplified and drives the PZT-controlled mirror M2. The electronic box provides also an option for the cavity scan. It is designed such that slightly more than one FSR ($\simeq 450$ MHz as $L \simeq 67$ cm) can be scanned. In this way, the longitudinal modes of the cavity as well as the dispersion signal can be monitored.

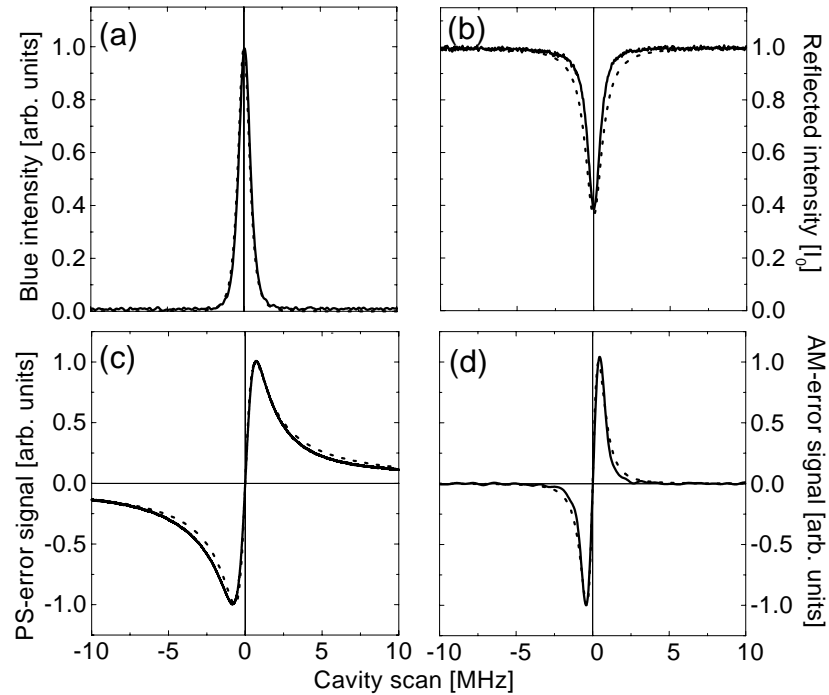


Figure 3.11: Measured (solid lines) and calculated (dotted lines) blue light generation (a), reflected intensity (b), and polarization spectroscopy error signal (c) as functions of the cavity length scan. (d) represents the AM-error signal calculated by numerical differentiation of (b). Calculated curves correspond to those from Fig. 3.5 ($R_1 = 98.6\%$, $R = 99.65\%$).

Alignment procedure

First, the infrared laser beam is aligned such that it hits M1, M2, M3 and M4 mirrors and the crystal faces roughly at the center. Then, M1 is removed and the crystal angles are adjusted for phase-matching. M1 is put back in place and the alignment is tweaked until an infrared flash appears inside the cavity. Then, the M2 mirror is swept and the blue output intensity through the M4 mirror is monitored. The mirror positions and the crystal angles are then tweaked and the beams are walked inside the cavity until reaching optimum operating conditions. Thereafter, the detection system is aligned and the dispersion signal is optimized.

Cavity performance at 850 nm

In Fig. 3.11 we show the curves measured on the doubling cavity while scanning and compare them to the simple theory from Sec. 3.2.1. The generated blue power is a measure for the intra-cavity intensity I_i . It is the conversion efficiency $\eta \propto I_i$ multiplied by I_i . Therefore, the generated blue intensity can be compared to the normalized theoretical value of I_i^2 . The input coupler has a reflectance $R_1 = 98.6\%$, but the total losses inside the resonator are unknown. These losses are due to the imperfections of mirror coating, but also due to the crystal and the SHG from it. The alignment also plays a role and can be included in other losses too. These were expressed as R . The only quantity we can determine is the fraction of light reflected at resonance. At the best ever measured output power (550 mW at 1.5 W infrared) it was about 37% of the incident power. This value actually fixes R to 99.65%. Thus, the theoretical curves presented in Fig. 3.11 correspond to those from Fig. 3.5. Now, the intra-cavity powers can be estimated on basis of Fig. 3.5(a) from which follows that, for $R_1 = 98.6\%$ and $R = 99.65\%$, $I_i \simeq 180I_0$. At a 1.5 W/850 nm pump the intra-cavity power was therefore 270 W. The generated blue power was 550 mW and, consequently, $\eta \simeq 0.2\%$.

In Fig. 3.12(a) the dependence of the generated blue power P_{SH} on the infrared pump power P_0 at 850 nm is shown. If the losses inside the cavity were independent of P_0 , P_{SH} should go as the square of P_0 ($I_i \propto I_0$). This is, however, not the case. By fitting the measured data, this dependence is evaluated to $P_{SH} = 147_{\pm 5}(P_0 + \alpha P_0^2)$, where $\alpha \simeq 1$. The question is where does the linear term originates from. First of all, as P_0 increases, the intra-cavity power P_i increases too and so does the efficiency η . At $P_0 = 1.5$ W, $\eta \simeq 0.2\%$ and this is a considerable fraction from $1 - R = 0.35\%$. Thus, increased P_0 results in increased losses. This pushes the enhancement factor down. The dependence of P_i on R at fixed R_1 is nonlinear and, therefore, P_{SH} cannot be quadratic in P_0 . Yet another reason for this behavior might be the fact that when P_i increases, the crystal temperature might increase too. This could result in a nonlinear dependence of η on P_0 . Qualitative proof for this is that, after locking the doubling cavity, it takes several minutes for the blue power to reach steady-state. For sure, both these effects are coupled.

Wavelength tunability

For spectroscopic applications we require the blue frequency to be tunable. Our doubling cavity has $FSR \simeq 450$ MHz. The PZT-driven mirror can move at maximum $\pm 5 \mu\text{m}$ (10 μm in total). It follows that the cavity can be continuously scanned with the laser for no more than ± 2.6 GHz at 850 nm. This corresponds to a change in the SH frequency of ± 5.2 GHz. In practice, only ± 3 GHz in the blue can be accomplished. In order to get larger continuous scan ranges, a Brewster-plate could be mounted into the cavity. It could then take care of slow variations, while the PZT mirror would

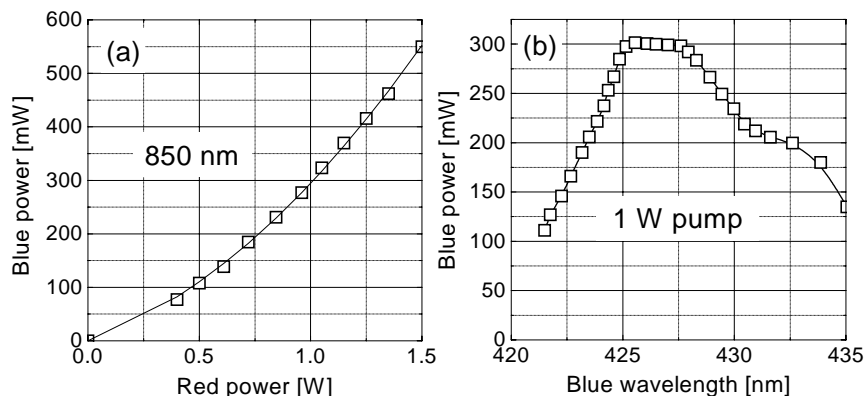


Figure 3.12: Doubling cavity power characteristics. (a) Power dependence of the generated blue light (425 nm) on the fundamental (850 nm) pump power. (b) Blue power at 1 W fundamental power as a function of the SH wavelength.

correct for higher frequencies.

If a larger wavelength range is required, the cavity can be unlocked and again re-locked. However, for wavelength changes larger than 0.2 nm in the infrared the cavity alignment must be tweaked. In a very rough approach, only the orientation of the LBO crystal and of the QW-plate in the stabilization unit can be adjusted. We did this and the measured dependence of P_{SH} on the blue wavelength is shown in Fig. 3.12(b) for $P_0 = 1$ W. An even better performance is obtained when tweaking the whole cavity alignment. We did this too but only for two wavelengths, 880 nm and 840 nm. The resulting blue powers were 260 mW and 180 mW, respectively, at a 1.0 W pump.

All blue powers mentioned above are sums of powers measured in three beams. The direct beam exiting through the output coupler M4 is about 90% of the total power. Two reflections from the crystal faces (one dominant and the other one weak) contain 10%. These reflections are due to the fact that the blue wave is *s*-polarized and, therefore, some part of it is reflected from the crystal faces. These reflected beams exit the doubling cavity through a window (made of a blue filter BG39) that is depicted in Fig. 3.9 with the letter P. The dominant reflection is used for laser stabilization onto the chromium resonance and also for monitoring the atom beam.

Frequency linewidth and power stability

For laser manipulation of chromium we require the blue frequency width to be below the width of the ^{52}Cr resonance at 425.55 nm of 5 MHz. From the cavity scan shown in Fig. 3.11(a) we estimate this to $\lesssim 0.8$ MHz at FWHM. To estimate the linewidth

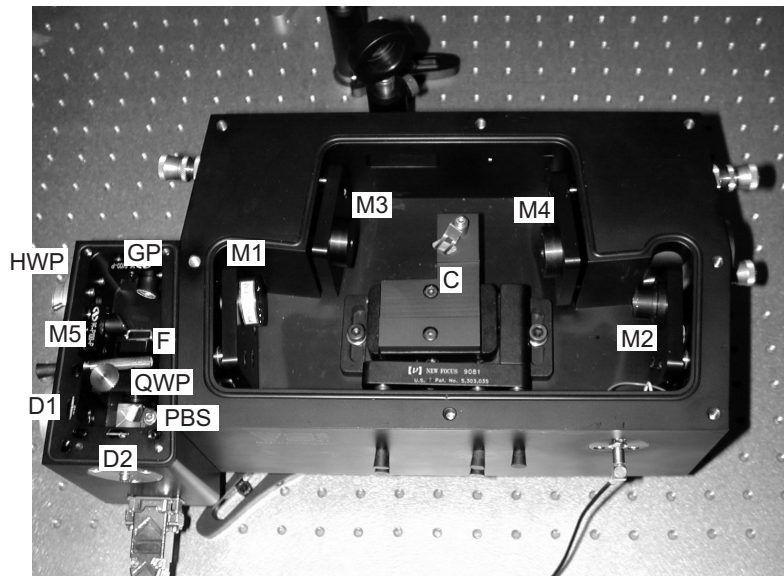


Figure 3.13: JET-cavity: experimental realization. For description of components see Fig. 3.8.

of the infrared laser beam our argument is as follows. If part of the infrared laser line was blocked by the cavity or if the laser line was as broad as the cavity resonance, the theory would not fit the experiment so well. Therefore, what is seen while scanning the cavity is dominated by the cavity itself. The laser line is therefore considerably narrower than 1.13 MHz ($\simeq \sqrt{2} \times 0.8$ MHz).

Finally, blue power stability is also a very important issue. There is always some persistent noise associated with the cavity jitter around the zero of the dispersion signal. After locking the cavity to the laser frequency, we were able to bring the power fluctuations below $\pm 0.75\%$.

Realization

Our doubling cavity is shown in Fig. 3.13. This device carries a name: JET. J stands for Jurdik, E stands for Van Etteger and T stands for Toonen – co-workers who helped with technical details and realization.

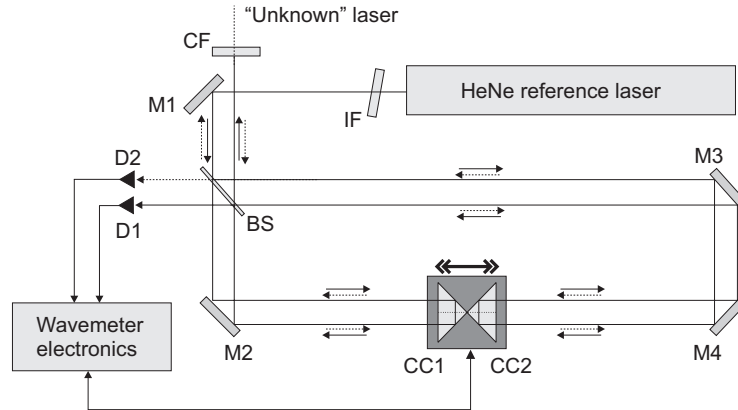


Figure 3.14: Schematic design of the wavemeter. M1, M2, M3, M4 – mirrors; CC1, CC2 – moving retro-reflectors (corner cubes); CF – color filter; IF – HeNe interference filter; BS – pellicle beam splitter; D1, D2 – detectors.

3.2.4 Michelson wavemeter

In order to locate an atomic resonance within one continuous scan of our laser system, the laser wavelength should be determined with a precision better than ± 3 GHz in the blue or ± 1.5 GHz in the infrared. 1.5 GHz at 850 nm corresponds to about 0.004 nm. To this end we have designed and built a wavemeter with an accuracy of ± 0.001 nm.

Interferometric wavelength determination

Suppose that a reference laser beam (with a wavelength λ_r) co-propagates with an “unknown” laser beam (λ_u) in an interferometer. If the interferometer arm moved a distance L , the ratio λ_u/λ_r could be determined by just counting the interference fringes. The required accuracy $\delta\lambda_u$ dictates the minimum number of fringes that must be counted and, therefore, the minimum distance the arm must move. Also, if this fringe counting technique is to be applied, the two lasers involved must have coherence lengths larger than the total arm travel.

Schematic design

A schematic of our interferometer for wavelength measurements is shown in Fig. 3.14. The reference laser is a 1 mW, single-frequency, stabilized helium-neon (HeNe) laser (Spectra Physics 117A). Its nominal frequency is 473.61254 THz (vacuum wavelength 632.99105 nm). In the frequency-stabilized regime this does not drift more than ± 3.0 MHz during 8 hours. The HeNe beam is directed into the interferometer arm

through a folding mirror M1. Then, on a pellicle beam-splitter BS it is split into two parts. The first beam is folded by a mirror M2 onto a retro-reflector – corner-cube CC1. The retro-reflected beam propagates parallel to the incoming beam (the distance between these two beams is 8 mm) and is then directed through BS onto a photodiode D1. Similarly, the second HeNe beam propagates from M3 to M4 to CC2 and is retro-reflected such that it recombines with the first retro-reflection after being partially transmitted through BS. The “unknown” laser beam counter-propagates the HeNe beam in the interferometer and, therefore, its retro-reflections recombine at the position of the D2 photodiode. Two filters in front of each laser are used to prevent beams from entering the laser cavities and causing frequency instabilities. CC1 and CC2 are rigidly connected together and move parallel to the beams. This motion gives rise to interference fringes that can be detected by D1 and D2.

Our wavemeter is in fact a Michelson interferometer. We note that similar devices (with even much higher accuracies) were built in the past. The most similar to our wavemeter is the one reported in [23].

Motion of the retro-reflectors

If we set the upper limit for λ_u to 1 μm , how much should the unit CC1-CC2 move in order to achieve an accuracy $\delta\lambda_u = \pm 0.001 \text{ nm}$ ($= \pm 1 \text{ pm}$)? The ratio of the number of fringes counted on D1 on the reference (N_r) and on D2 on the “unknown” beam (N_u) is related to the two involved wavelengths via

$$\frac{N_r}{N_u} = \frac{\lambda_u}{\lambda_r}. \quad (3.10)$$

It is therefore enough to count as many “unknown” fringes as is the wavelength λ_r , expressed in pm, that is 632991 fringes in vacuum. The number of fringes counted on the reference N_r is then λ_u measured in pm to within $\pm 1 \text{ pm}$.

Because in our interferometer the fringes arise each quarter-wavelength, it is enough for the arm to move by $L = 632991/4 \times 10^6 \text{ pm} \simeq 16 \text{ cm}$. This is the upper limit. For wavelengths shorter than 1 μm , less than 16 cm is needed. We note that, for accuracies higher than $\pm 1 \text{ pm}$, the arm would have to move proportionally more or one would be required to have a resolution better than one fringe.

The next question concerns the speed of the detection system. Intuitively, signals that are at least as fast as the frequency ν at which the fringes arise must be detected. This frequency depends on the speed of the moving arm v and on the shorter wavelength from the two λ_r and λ_u ,

$$\nu = \frac{4v}{\min\{\lambda_r, \lambda_u\}}. \quad (3.11)$$

Thus, if we set the lower limit on λ_u to 400 nm and the maximum speed of the moving arm to 20 cm/s, the frequency we must deal with is 2 MHz.

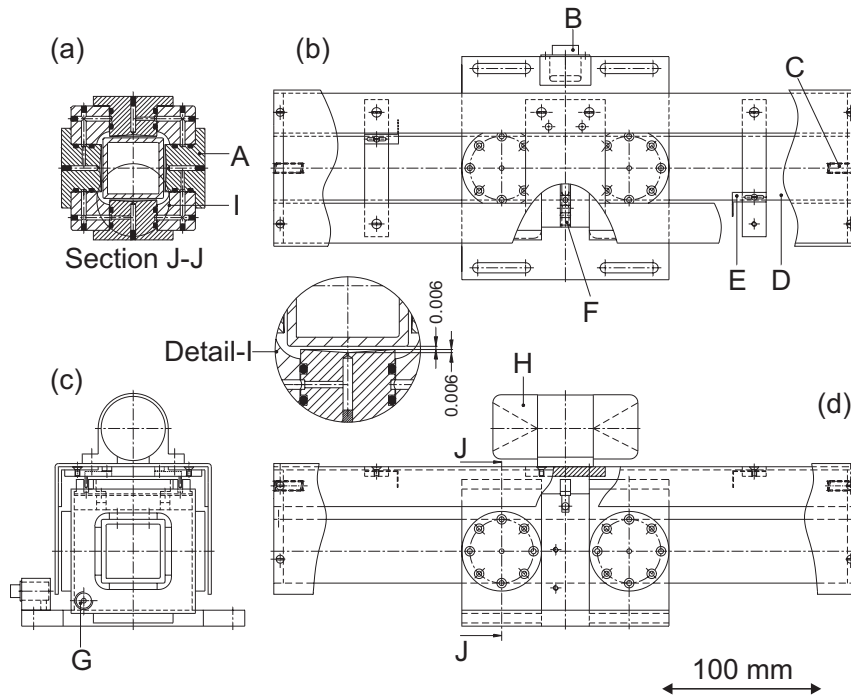


Figure 3.15: Design of the air-bearing system for moving retro-reflectors. (a) Cross-section J-J as depicted in (d); (b) top view; (c) front view; (d) side view. A – air-bearing tip; B – standard 'D' connector; C – push spring; D – stainless-steel bar; E – begin-end position indicator; F – position detector; G – compressed air input; H – corner cube holder.

Novel air-bearing unit

In order to detect undisturbed interference fringes the CC1-CC2 unit must move smoothly and parallel to the incoming beams, with the least possible noise arising from the motion. We have analyzed this problem carefully and designed a novel air-bearing system on which the moving arm is supported. Our design is shown in Fig. 3.15.

The air-bearing unit itself is mounted rigidly on the optical table. The moving part is the stainless-steel rail itself. We note that such a construction is an inverted version of ordinary air-bearings. This was done in order to avoid any straight mechanical coupling between the moving arm and the laboratory. Such would be an inlet tube for the air flow from “the top to the bottom.” Furthermore, to prevent

torque instabilities, the rail is square-shaped and the air-bearing is created on each of the rail's four sides. Also, to avoid flipping of the arm there are two such air-bearing units positioned 80 mm apart. There are thus 8 tips through which the air is pumped into the bearing. The air-cushion-tip geometry was designed according to standard models for performance optimization of air-bearing systems [24, 25]. There is only one main inlet for air. Then, the air is guided to all tips through small channels. Because all the tips are interconnected, no pronounced pressure fluctuations can appear. The inlet is connected to a dry-nitrogen source at a constant pressure of 3 bar. Our design of the air-bearing minimizes leaks into the optical path and also nitrogen losses in general.

The rail is brought to motion by a gentle push. Ideally, it moves almost frictionless at a speed of 10 to 15 cm/s. At each of the ends, one small push-spring is mounted. These springs, at the turning points, help the rail to change the direction smoothly and transfer a momentum such that the rail is kept longer in motion. With no additional tricks, the rail moves back and forth, without considerable reduction of the speed, for about 40 turns. To keep the arm in motion for longer times, a small magnet is mounted near each spring. Two solenoids are connected to the static part of the system such that the magnets can slide into them. Activation of the solenoids keeps the arm in uninterrupted motion. Interestingly, our air-bearing system can carry easily a mass of 6 kg.

Electronic detection

The intensities I_r and I_u detected on the photodiodes D1 and D2, respectively, are cosine-square-like functions of time. There can always be some dc-offset in these intensities because the BS is not necessarily a fifty-fifty beam splitter. Also, for different wavelengths the signals might look different. Therefore, our detection scheme shown in Fig. 3.16 is ac-coupled. The fringes are detected by making (binary) step-functions from I_r and I_u (Schmitt-triggers). The trigger level can be adjusted but in practice 0 V always makes it work. The steps are then counted with two binary counters: a down-counter from a preset value equal to λ_r in pm on the "unknown" channel and an up-counter on the reference. At the moment when the down-counter hits 0, the number counted on the up-counter contains the wavelength of the "unknown" laser in pm and is displayed. The counting process does not start immediately after the moving arm turns around. Some time is allowed for the mechanical system to stabilize. Counting is initialized by an indicator on each side, depending on whether the arm moves to the right or to the left (Fig. 3.15).

The electronics does not servo-control the magnetic pulses. In fact, it just passively sends current pulses to the coils. The strength of the pulse and the time delay between the pulse and the moment when the system indicates its end-position are adjustable.

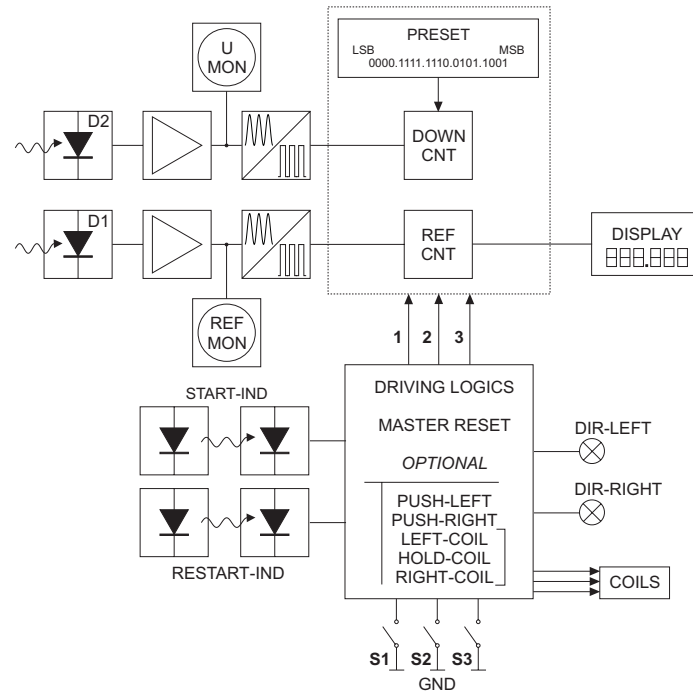


Figure 3.16: Schematic of the wavemeter electronics. D1 – detector of reference fringes; D2 – detector of “unknown” fringes; U-MON – monitor of “unknown” fringes; REF-MON – monitor of reference fringes; DOWN-CNT – binary down-counter; REF-CNT – binary up-counter; PRESET – preset wavelength of the HeNe laser of 632816 pm; START-IND and RESTART-IND – start and restart position detectors; S1 – start switch; S2 – reset switch; S3 – stop switch; 1 – start; 2 – stop; 3 – reset; DIR-LEFT and DIR-RIGHT – direction indicators.

Dispersion of air

The fact that the measurements takes place in air and not in vacuum must be taken into account. We correct for this using the empirical Cauchy formula for the refractive index of air n_{air} (see [26], pp. 10-290),

$$n_{\text{air}} = 1.000272643 + \frac{122.88}{\lambda^2} + \frac{355.5 \times 10^6}{\lambda^4}, \quad (3.12)$$

where λ is the vacuum wavelength expressed in Å. The wavelength in air is $\lambda_{\text{air}} = \lambda/n_{\text{air}}$. Eq. (3.12) best approximates the values of n_{air} at 15 °C and normal atmospheric pressure (760 mm Hg). If we tried to measure λ_u with a precision much

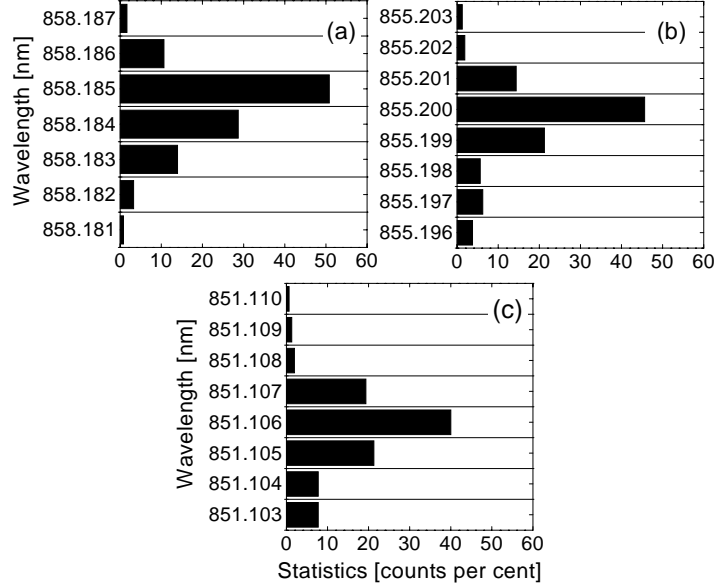


Figure 3.17: Statistics of the wavemeter counts at reference wavelengths whose second harmonic generation corresponds to three different ^{52}Cr transitions from the 7S_3 ground state to the $^7P^o$ excited states at (a) $J = 2$, (b) $J = 3$, and (c) $J = 4$. The measured wavelengths were corrected for the dispersion of air. Values expected from tabulated ^{52}Cr transitions: (a) 858.1846 nm, (b) 855.1997 nm, and (c) 851.1058 nm (see Tab. 3.1, pp. 73).

higher than $\delta\lambda_u = \pm 1$ pm, we would need to correct even for the temperature, pressure and humidity. It follows that our reference wavelength $\lambda_r^{\text{air}} = 632816$ pm. The preset wavelength in our electronics shown in Fig. 3.16 is this dispersion-corrected λ_r (expressed as a binary number 10011010011111110000).

Performance

The error-budget (that includes possible misalignment of the reference and “unknown” beams, mechanical instabilities, fluctuating refractive index in the optical path due to the moving air, wavefront distortion and intrinsic error due to the electronic detection) is dominated by the intrinsic error due to the electronic detection. An accuracy of ± 1 pm is therefore expected.

To show this, we measured the wavelength of three different transitions of the dominant chromium isotope ^{52}Cr from the ground state 7S_3 to the excited states

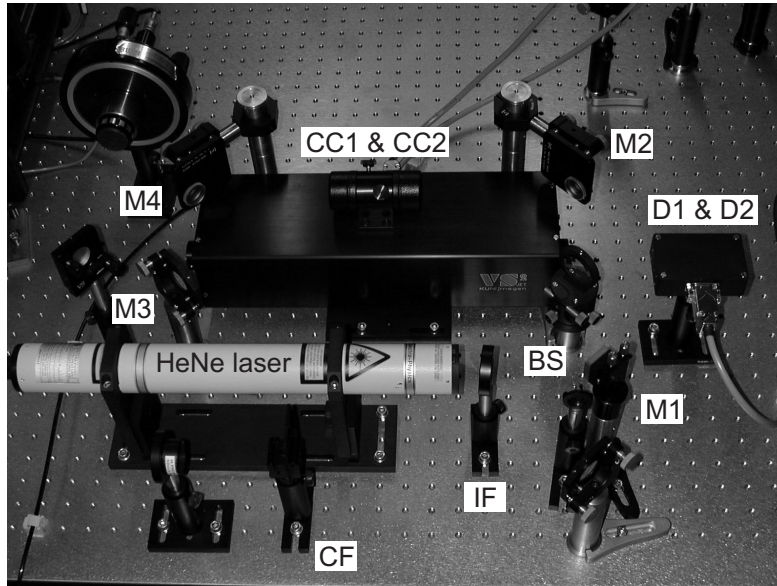


Figure 3.18: JET-wavemeter: experimental setup. For description of components see Fig. 3.14.

${}^7P_2^o$, ${}^7P_3^o$ and ${}^7P_4^o$ (see next section). The measurements were carried out 250-times for each transition in order to get a reasonable statistics. To summarize, from 750 total measurements, the correct value for λ_u was obtained 342-times (45.6%). Furthermore, $\delta\lambda_u = \pm 1$ pm was obtained in 289 cases (38.5%) and $\delta\lambda_u = \pm 2$ pm in 82 cases (11%). A bigger error was made 37-times (4.9%).

Realization

The actual realization of our JET-wavemeter is shown in Fig. 3.18.

3.2.5 Absolute stabilization

Our aim is to stabilize the laser frequency onto the ${}^7S_3 \rightarrow {}^7P_4^o$ ${}^{52}\text{Cr}$ resonance. To this end we have designed and constructed a stabilization unit based on the detection of a laser-induced fluorescence (LIF) signal from the chromium beam.

Laser spectroscopy

There are a number of methods developed in the field of laser spectroscopy of atoms that provide bi-polar signals suitable for cavity stabilization [27]. For example, a resonance can be saturated with a strong pump beam and probed with a counter-propagating weak beam (saturation spectroscopy). Exactly at resonance, the atomic vapor appears more transparent for the probe. When modulating the laser frequency a dispersion signal can be detected with a lock-in technique. In another approach, a circularly-polarized pump is used. This induces birefringence and, therefore, alters the probe polarization (polarization spectroscopy). The optical detection scheme can be adjusted such that a signal, which changes sign exactly at resonance, is registered. In principle, both these techniques could be applied for stabilizing our laser.

An alternative approach relies on the detection of a LIF signal from a fast atom beam. This beam exits for example an effusion cell held at a temperature T_0 through a small orifice. The ensemble of atoms in the beam then obeys Maxwell-Boltzmann statistics. Therefore, there is always a wide spread of atomic velocities, whether transverse or longitudinal. The atoms exiting the cell at some angle α are most likely to have certain transverse velocity and less likely to have another one. The transverse position of an atom at a given longitudinal position is thus statistically related to the atomic speed.

Whether a photon scatters on a two-level atom depends on the detuning Δ of the photon frequency ω from the atomic resonance frequency ω_0 , but also on the atomic velocity in the direction of the photon v_x . The Doppler-shifted scattering cross-section σ is given by

$$\sigma(\Delta, v_x) = \sigma_0 \frac{(\Gamma/2)^2}{(\Delta - kv_x)^2 + (\Gamma/2)^2}, \quad (3.13)$$

where σ_0 is the maximum scattering cross-section, k is the wave-vector of the photon and Γ is the natural linewidth of the atomic transition. We note that σ is maximized when $\Delta = kv_x$. If the laser frequency approaches the atomic resonance from the bottom, first the atoms counter-propagating the laser beam come to resonance ($\Delta < 0$), then those at rest in the transverse direction ($\Delta = 0$) and finally the ones moving in the direction of the laser ($\Delta > 0$). In order to fix the laser frequency at some Δ , the fluorescent spot observed on the atom beam must be stopped from drifting and jittering.

Detection scheme

In Fig. 3.19(a) the principles of our method are shown. The signal to servo-lock the laser is obtained by imaging the fluorescent spot onto a split-photodiode. An objective lens with a focal length of 20 mm is used. The distance between the lens and the axis of the atom beam is 132 mm. The image is then formed in the plane 23.6 mm behind the lens. In this plane the split-photodiode is located. It follows that

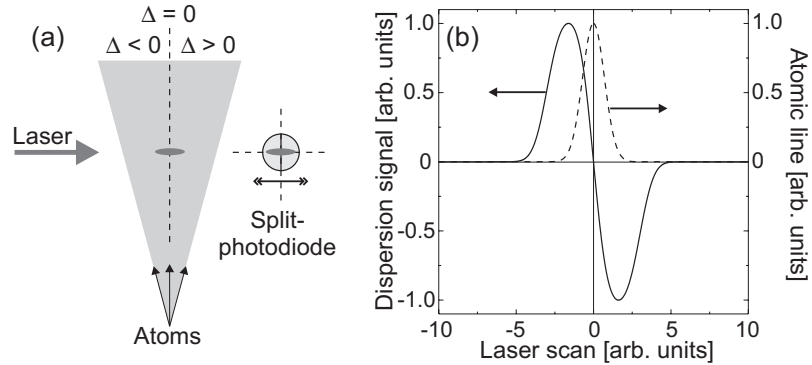


Figure 3.19: Split-photodiode technique. (a) Principles. The atom beam is illuminated in the transverse direction by a laser. The position of the fluorescent spot depends on Δ . This spot is imaged onto a split-photodiode. The measured signal is used to servo-lock the laser. (b) Calculated dispersion from a Gaussian-shaped resonance.

the image is demagnified by a factor of 5.6 with respect to the object. Whenever the laser frequency exhibits some deviations from the desired value, the difference signal between the right and the left area of the detector is non-zero. It is processed by an integrator with integration times adjustable from 0.01 s to 1 s. The length of the reference cavity is controlled by steering the galvo-driven Brewster plate inside this cavity (see Fig. 3.6).

When scanning the laser frequency, a dispersion signal similar to what is seen in Fig. 3.5(b) is detected. Note that the profile of the measured atomic line depends on several factors. First of all, Doppler broadening which is due to Eq. (3.13) plays an important role. Secondly, the higher the laser intensity or the larger the atom flux the wider the observed resonance and the higher the maximum detected intensity (although it might saturate). It follows that the total gain in our system depends on both the laser intensity and the average atom flux. Furthermore, the gain scales proportionally with the scan-range settings on the laser electronics. The best performance of the system is observed when using a 3 mW laser beam with a $1/e^2$ radius of 1.0 mm and a laser scan-range of 1 GHz.

The detection system is movable in the transverse directions in order to adjust Δ to a desired value. The correlation between the most probable longitudinal velocity v_z and the most probable transverse velocity v_x is expressed as

$$x = \frac{v_x}{v_z} z. \quad (3.14)$$

From Eqs. (3.13) and (3.14) follows that, at a given longitudinal position z , the

Transition	λ [nm]	λ_{air} [nm]	λ^f [nm]	λ_{air}^f [nm]
${}^7S_3 \rightarrow {}^7P_4^o$	425.55292	425.43359	851.10584	850.87236
${}^7S_3 \rightarrow {}^7P_3^o$	427.59986	427.47998	855.19972	854.96504
${}^7S_3 \rightarrow {}^7P_2^o$	429.09228	428.97202	858.18456	857.94912

Table 3.1: Chromium resonances. λ – *in vacuo* wavelength, λ_{air} – wavelength corrected for dispersion of air. Corresponding “fundamental” wavelengths λ^f and λ_{air}^f (to be dialed on the Ti:Sapph. laser).

fluorescent spot center is located at a transverse position x (measured from the beam axis) given by

$$x = \frac{\Delta}{2\pi} \frac{\lambda}{v_z} z, \quad (3.15)$$

where λ is the laser wavelength. Therefore, to adjust Δ to within $\delta\Delta$ the required accuracy of x positioning is δx ,

$$\delta x = \frac{\delta\Delta}{2\pi} \frac{\lambda}{v_z} z. \quad (3.16)$$

In our system, the longitudinal distance between the stabilization unit and the oven orifice $z \simeq 150$ mm. Furthermore, at $T_o = 1900$ K, the most probable longitudinal velocity of atoms $v_z \simeq 955$ m/s, provided $x/z \ll 1$. All detunings $\Delta/2\pi$ between +100 MHz and –100 MHz around the resonance at $\lambda = 425.55$ nm are thus reached when the detection unit is translated around the atom beam axis by $\Delta x \simeq \pm 7$ mm. Moreover, if $\delta\Delta/2\pi < 100$ kHz is desired, then $\delta x < 7$ μm . Our detection system is mounted on a micro-translator that allows for both a total travel of ± 8 mm and an accuracy and reproducibility of ± 4 μm . It depends also on the chromium flux how far away from the resonance the system can be held. In practice, no more than a few MHz will be needed.

Chromium spectroscopy

There are three ${}^{52}\text{Cr}$ transitions from the ground state 7S_3 we can observe with our blue laser light. They correspond to the wavelengths shown in Tab. 3.1. We replaced the split-photodiode with a $\varnothing 0.2$ mm fiber and performed spectroscopy of the chromium beam. The laser frequency was scanned around each resonance and the spectra were recorded with a digital oscilloscope. Then, the laser was stopped from scanning and a photograph of the fluorescent spot at each resonance was taken with a simple digital camera. These results are shown in Fig. 3.20. Besides the main lines, also some satellites appear in the spectra. These are actually other chromium isotopes (isotopic shift).

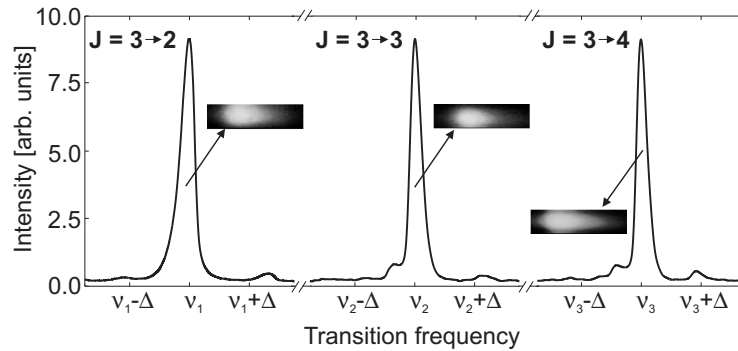


Figure 3.20: Spectroscopy of the ${}^7S_3 \rightarrow {}^7P_2^o$, ${}^7S_3 \rightarrow {}^7P_3^o$, and ${}^7S_3 \rightarrow {}^7P_4^o$ chromium transitions. $\nu_1 \simeq 698.667 \times 10^6$ MHz, $\nu_2 \simeq 701.105 \times 10^6$ MHz, $\nu_3 = 704.478 \times 10^6$ MHz (tabulated values), and $\Delta \simeq 400$ MHz (as estimated from the laser scan width). The photographs were taken with a simple digital camera focused onto the atom beam.

Laser stabilization onto the ${}^7S_3 \rightarrow {}^7P_4^o$ ${}^{52}\text{Cr}$ transition

In order to servo-lock the laser near the ${}^7S_3 \rightarrow {}^7P_4^o$ ${}^{52}\text{Cr}$ transition the laser control must be switched to external position. Then, our electronic box is used to dc-scan the laser frequency. When the image of the fluorescent spot crosses the split-photodiode (Fig. 3.21), the system is locked onto the dispersion signal. The laser frequency can be changed by just gently translating the detection optics.

The absolute resonance of the laser with the chromium transition can be found as follows. The detection laser beam is reflected on itself and the laser frequency is scanned. Two fluorescent spots that move against each other are noticed on the chromium beam. The detection unit is translated until no difference signal from the split-photodiode is detected. The retro-reflected beam is then blocked and the laser frequency is locked onto the fluorescent spot. In this case, the laser is absolutely referenced to the ${}^7S_3 \rightarrow {}^7P_4^o$ ${}^{52}\text{Cr}$ transition.

How stable the laser frequency is can be monitored on the signal from the split-photodiode. Alternatively, a spectrum analyzer can be used. Also, the split-photodiode can be replaced with a fiber and the blue frequency jitter can be detected. We have applied all three methods and concluded that the infrared laser frequency fluctuations can be suppressed below 0.25 MHz (peak-to-peak). The blue frequency still jitters ± 0.25 MHz around the resonance.

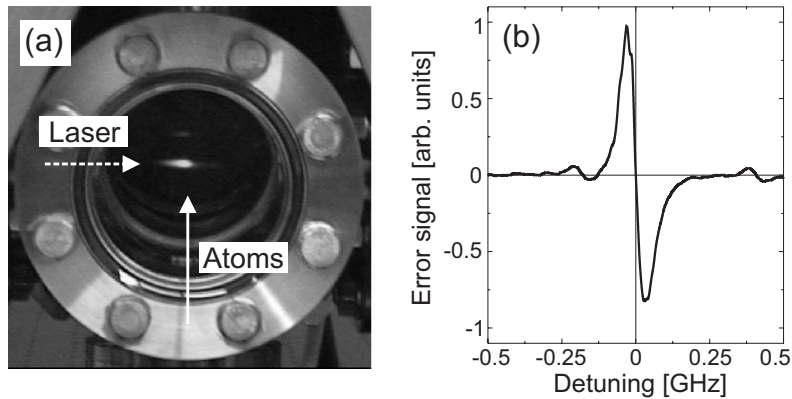


Figure 3.21: (a) Detected laser-induced fluorescence signal on the chromium beam (${}^7S_3 \rightarrow {}^7P_4^o$ transition). (b) Error-signal for laser stabilization onto the chromium resonance measured with the split-photodiode technique. The detection system is “looking” at the fluorescent spot from the side opposite to the one from which the photograph (a) was taken.

3.3 Vacuum part

In Sec. 3.3.1 the design and construction of the main frame of our vacuum system is described. Sec. 3.3.2 is devoted to our sample manipulation system and the *in vacuo* optics.

3.3.1 Main frame

Our vacuum setup is schematically shown in Fig. 3.22(a) and its actual realization is seen on the photograph in Fig. 3.22(b). The system is built vertically because of two reasons. First of all, chromium is evaporated from a high-temperature effusion cell and a vertical construction assures more stable operating conditions for this cell. Secondly, the space requirements for the basic setup are minimized in this way, providing us with the possibility of horizontal extension with UHV accessories in the near future. Our vacuum system is mounted on a frame rigidly bolted to the optical table and is centered around a $\varnothing 500$ mm hole in the table.

After the atoms exit the effusion cell, they propagate across the stabilization chamber. Then, they enter the main chamber where the actual experiments are performed. The sample and the *in vacuo* optics are mounted onto a manipulator and can be moved either in or out of the chromium beam. The last chamber, mounted on a longer extension tube, is meant for detection and analysis of the atom beam.

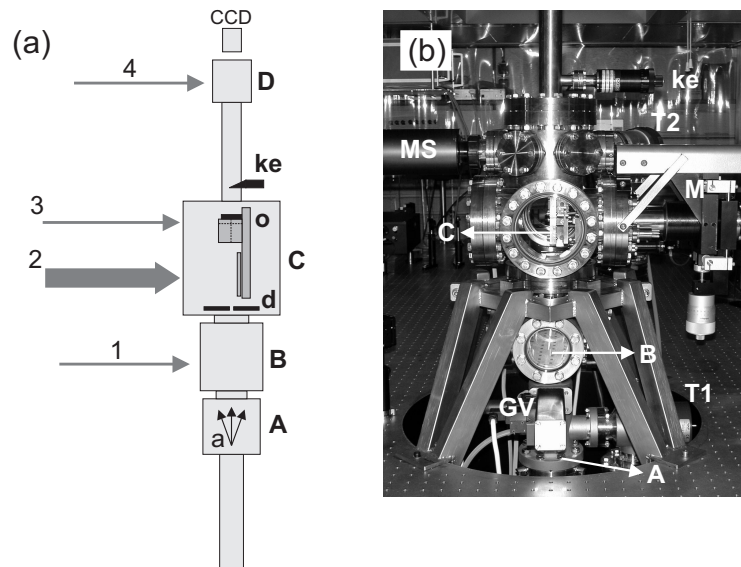


Figure 3.22: Vacuum system. (a) Schematic: A – evaporator chamber; B – stabilization chamber; C – main chamber; D – detection chamber; ke – knife-edge; d – diaphragm; o – *in vacuo* optics; a – atom beam; laser beams: 1 – stabilization, 2 – collimation, 3 – focusing, 4 – detection. (b) Realization: GV – gate valve; T1, T2 – turbo-molecular pumps; M – manipulator; MS – mass spectrometer.

Evaporator

We use a commercial high-temperature effusion cell to evaporate the chromium atoms (model HTC-40-10, CreaTec Fischer & Co.). A tantalum crucible with a volume 10 ccm and a $\varnothing 1$ mm exit aperture is filled with chromium granules with a purity 99.99%. The heating system is a self-supported tungsten wire. The temperature is monitored with a thermocouple. An electronic control unit (CU-905-S1-DC, Eurotherm Controls), that contains a dc-power supply and a PID (proportional-integral-derivative) controller, is used for heating the oven and regulating the temperature. Usually, we run the oven at 1500 °C to 1625 °C. The corresponding deposition rates measured at the sample position with a quartz-oscillator ranged from 0.024 Å/s to 0.125 Å/s ($\pm 10\%$).

In order to protect the vacuum from unwanted chromium deposition and also from the radiative heat we designed a system of four diaphragms that are mounted above the crucible. The first diaphragm is a copper cup with a $\varnothing 5$ mm aperture connected

with stainless-steel bolts onto the water-cooling jacket of the effusion cell. The next three diaphragms are molybdenum discs (with a $\varnothing 3$ mm aperture) separated from each other by 15 mm. These discs are supported by stainless-steel rods connected to the copper cup. It should be mentioned that the shielding unit did not close even after operating the oven for more than 700 hours.

The evaporator chamber is pumped with a turbo-molecular pump (EXT70H, Edwards) connected to the chamber via a UHV angle valve with pneumatic actuator (Series 28.3, VAT Vakuumentille). This pump is backed by a rotary vane pump (RV3, Edwards). Even though the pumping speed of the turbo-molecular pump itself is 70 l/s, the combined resistance of the valve and the connecting tubes reduces this speed to about 20 l/s. After a modest bake-out at 100 °C for 24 hours, the base pressure in the oven at room temperature was below 1×10^{-8} mbar, as measured with an active inverted magnetron gauge (AIM-SL-NW25, Edwards). Interestingly, with the pump pumping on itself, we cannot reach much better pressures than that. When operating the oven at 1625 °C, the base pressure increases to about 10^{-7} mbar.

The atom beam orientation can be tweaked by adjusting three differential screws of the UHV bellows with which the oven is connected to the stabilization chamber. The evaporator chamber can be isolated from the rest of the vacuum system by closing the UHV gate valve (Series 01, VAT Vakuumentille) mounted between the oven and the stabilization chamber.

Stabilization chamber

The intermediate chamber between the oven and the main chamber of the system is used for stabilization of the laser onto the chromium resonance. There are four viewports (DN63CF) in two orthogonal directions. These viewports are AR coated for 425 nm. The laser beam is directed across the chromium beam as shown in Fig. 3.21(a). The stabilization unit detects the LIF signal from the direction opposite to the one from which the photograph in Fig. 3.21(a) was taken. It is connected to three stainless-steel rods ($\varnothing 20$ mm) that are welded onto the flange. The stabilization chamber is pumped by both the oven and main chamber pumps, provided the gate valve is open.

Main chamber

The heart of our system is the main chamber. At the moment, there are three viewports (DN100CF) on this chamber. All of them are AR coated for 425 nm. On the fourth DN100CF flange the manipulator is mounted. Furthermore, six DN35CF flanges can be used for mounting small vacuum accessories. Three of them are currently in use for an active inverted magnetron gauge (AIM-SL-NW25, Edwards), a mass spectrometer (ANAVAC-2, VG-Gas Analysis) and a turbo-molecular pump (EXT70H, Edwards), respectively. The pump is connected to the system via a UHV

angle valve with pneumatic actuator (Series 28.3, VAT Vakuumventille) and is backed by the same rotary vane pump as the oven pump. In the near future, however, a vacuum ionization pump (VacIon Plus 150 Diode, Varian Vacuum Technologies) will be mounted on one of the DN100CF flanges to test whether UHV conditions can be reached in the main chamber.

A differential pumping scheme of the system is implemented. To this end, a diaphragm unit is mounted between the stabilization and main chambers. On the top of this unit a groove is made such that a thin stainless-steel plate with a narrow slit can be slid in. For experiments reported in the following, a square-shaped (1.5×1.5 mm) slit was used to pre-collimate the atom beam mechanically. Also, a shutter is connected to the diaphragm unit. When needed, this shutter can block the atom beam from reaching the sample.

The pressures that can be reached in the main chamber are routinely lower than those in the evaporator chamber. For example, at an oven temperature of 1625 °C the base pressure in the main chamber is still about 3×10^{-8} mbar. In the case that the vapor pressure of chromium as well as the oven degassing turn out to be the limiting factors for achieving UHV conditions in the main chamber, a nitrogen-cooled trap can be mounted between the oven and the stabilization chamber.

Detection chamber

The last chamber of our vacuum system is used for analysis and detection of the chromium beam. A relatively long extension tube between the main and detection chambers is used because it facilitates the detection scheme. There are four DN35CF viewports in two orthogonal directions. All of them are AR coated for 425 nm. At the top of the system, there is a DN35CF flange which can also be used for a viewport and consequently for detection of the atom beam. For experiments carried out in a one-dimensional geometry, however, the top viewport is not necessary.

A knife-edge mounted on a linear translator can be slid into the chromium beam. The distance between the knife-edge and the laser beam in the top chamber is about 560 mm. The relative density of atoms in the shadow of the knife-edge is a measure for the atom beam divergence (see Sec. 4.2.1).

3.3.2 *In vacuo* optics and manipulator

Laser-focused atomic deposition requires careful control mechanism of the sample position and alignment with respect to the focusing laser beam. Moreover, the focusing beam itself must be parallel to the laser beam used to collimate the atom beam to within a small fraction of a mrad. To this end we have designed and constructed a sample manipulation system with *in vacuo* optics connected to it.

Schematically, our system is shown in Fig. 3.23(a). The required degrees of freedom of the unit are three translations along x , y and z , and two rotations around y

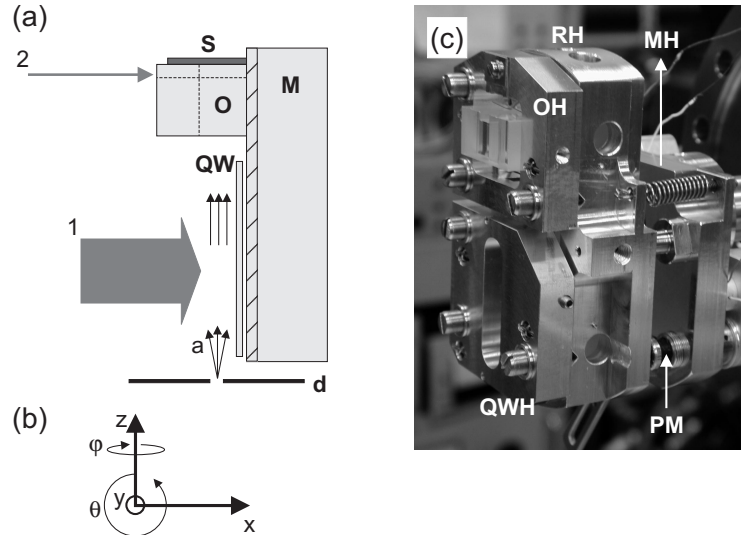


Figure 3.23: *In vacuo* optics. (a) Schematic: M – mirror; QW – quarter-wave plate; O – glass oblong; S – sample; a – atom beam; laser beams: 1 – cooling and 2 – focusing. (b) Required degrees of freedom. (c) Realization: MH – main holder; RH – mirror holder; OH – oblong holder; QWH – quarter-wave plate holder; PM – pico-motor.

and z , respectively [see Fig. 3.23(b)]. The actual realization of the system is shown in Fig. 3.23(c).

The mirror is a zerodur substrate coated with enhanced aluminum. Its dimensions ($x \times y \times z$) are $17 \times 25 \times 77$ mm. A glass oblong ($12 \times 25 \times 12$ mm) serves as a sample holder. It was cut from a prism with the right angle specified to within $\delta\alpha = \pm 0.015$ mrad (± 3 arcsec). We use the high quality optical faces of the oblong as a reference for angular adjustments of the sample with respect to the mirror. The sample is resting against the top face of the oblong. The atom beam is along z and the laser SW along x . Two grooves – one for the atoms (5×5 mm) and the other one for the laser (5×2 mm) – were cut into the oblong. A quarter-wave (QW) plate ($1 \times 10 \times 40$ mm) with the slow axis along the long side of the mirror is located about 1 mm from the mirror at the position where an optical molasses will be created. Using this plate, a polarization gradient (such as $\text{lin}\perp\text{lin}$ or $\sigma^+ - \sigma^-$) molasses scheme can be created.

The main parts of the optics holder are made from high strength aluminum (QC-7, ALCOA). Onto the mirror holder, the QW-plate and glass oblong holders are mounted. Three point adjustment of the two latter holders is allowed for. The

mirror holder is then mounted on the main holder. Two vacuum-compatible pico-motors (8301-V, New Focus) are used to adjust the two rotational degrees of freedom. The complete unit is rigidly fixed onto a hollow stainless-steel tube ($\varnothing 20$ mm, wall thickness 1.5 mm, length 254 mm). This tube is welded onto a DN35CF flange and mounted onto a manipulator (152-372A, Mitutoyo) with translational degrees of freedom along x (total range 50 mm, accuracy $25 \mu\text{m}$), y (25 mm, $2.5 \mu\text{m}$) and z (25 mm, $2.5 \mu\text{m}$). The electrical connection to the pico-motors is made on the main manipulator flange (DN100CF) via a DN16CF electrical feedthrough. On the same flange, there is also a DN16CF rotational feedthrough onto which a small hook is bolted. This hook connects to the shutter on the diaphragm unit between the main and stabilization chambers.

It should be stressed that all materials used for making the *in vacuo* optics and sample manipulation device, which in fact consists of more than 100 small parts and pieces, were carefully selected for the highest possible system stability. The unit is also expected to comply with UHV requirements. Moreover, whenever it was possible, we avoided use of materials which could be magnetized. Such materials could disturb the polarization gradient molasses in our future experiments.

3.4 Conclusions

We have constructed a system for laser-manipulated chromium deposition. We designed, developed and built a single-frequency Ti:Sapph. laser, an external enhancement doubling cavity based on an LBO crystal, a Michelson wavemeter, a unit for absolute stabilization of the laser frequency and a vacuum system.

Our doubling cavity provides conversion efficiencies up to 36.7% at an SH wavelength of 425 nm. The blue power exhibits fluctuations of only 0.75% (peak-to-peak). After locking the laser to the ${}^7S_3 \rightarrow {}^7P_4^o$ ${}^{52}\text{Cr}$ resonance, the blue frequency jitter was suppressed to ± 0.25 MHz (peak-to-peak). The performance of our laser system therefore complies with the criteria we required for laser-manipulated chromium deposition.

We consider the extreme efficiencies obtained with our JET-cavity and also the air-bearing unit of our JET-wavemeter to be the major (original) results of our development work.

Finally, we note that our laser system is not restricted to only one atomic species. At this moment, we have the possibility of changing the infrared wavelengths from 800 nm to 900 nm and the blue wavelengths from about 420 nm to 440 nm. Also, the system can be upgraded in a relatively straightforward way to cover almost the whole visible spectrum. Either the optics (laser and cavity mirrors) and the LBO crystal can be replaced, or the laser itself can be upgraded to its dye version.

References

- [1] R.L. Barger, M.S. Sorem, J.L. Hall. Frequency stabilization of a cw dye laser. *Appl. Phys. Lett.*, 22:573–575, 1973.
- [2] T.W. Hänsch and B. Couillaud. Laser frequency stabilization by polarization spectroscopy of a reflecting reference cavity. *Opt. Commun.*, 35:441–444, 1980.
- [3] A.D. White. Frequency stabilization of gas lasers. *IEEE J. Quant. Electron.*, QE-1:349–357, 1965.
- [4] R.V. Pound. Electronic stabilization of microwave oscillators. *Rev. Sci. Instrum.*, 17:490–505, 1946.
- [5] R.W.P. Drewer, J.L. Hall, F.V. Kowalski, J. Hough, G.M. Ford, A.J. Munley, and H. Ward. Laser phase and frequency stabilization using an optical resonator. *Appl. Phys. B*, 31:97–105, 1983.
- [6] B.E.A. Saleh and M.C. Teich. *Fundamentals of Photonics*. John Wiley & Sons, New York, 1991.
- [7] A. Yariv. *Quantum Electronics*. John Wiley & Sons, New York, 1989.
- [8] W. Koechner. *Solid-State Laser Engineering*. Springer-Verlag, Berlin, 1999.
- [9] J.T. Verdeyen. *Laser Electronics*. Prentice-Hall, Englewood Cliffs, New Jersey, 1989.
- [10] P.W. Milonni and J.H. Eberly. *Lasers*. John Wiley & Sons, New York, 1988.
- [11] A. Gerrard and J.M. Burch. *Introduction to Matrix Methods in Optics*. Dover, New York, 1994.
- [12] Y.R. Shen. *The Principles of Nonlinear Optics*. John Wiley & Sons, New York, 1984.
- [13] R.W. Boyd. *Nonlinear Optics*. Academic Press, San Diego, CA, 1992.
- [14] D.L. Mills. *Nonlinear Optics: Basic Concepts*. Springer-Verlag, Heidelberg, 1991.
- [15] P.N. Butcher and D. Cotter. *The Elements of Nonlinear Optics*. Cambridge University Press, Cambridge, 1990.
- [16] A. Yariv and P. Yeh. *Optical Waves in Crystals*. John Wiley & Sons, New York, 1984.

-
- [17] C.S. Adams and A.I. Ferguson. Tunable narrow linewidth ultra-violet light generation by frequency doubling of a ring Ti:sapphire laser using lithium tri-borate in an external enhancement cavity. *Opt. Commun.*, 90:89–94, 1992.
- [18] S. Bourzeix, M.D. Plimmer, F. Nez, L. Julien, and F. Biraben. Efficient frequency doubling of a continuous wave titanium:sapphire laser in an external enhancement cavity. *Opt. Commun.*, 99:89–94, 1993.
- [19] H. Tsuchida. Frequency doubling of a tunable Ti:sapphire laser with KNbO_3 in external cavity. *Jpn. J. Appl. Phys.*, 33:6190–6194, 1994.
- [20] S. Bourzeix, B. de Beauvoir, F. Nez, F. de Tomasi, L. Julien, and F. Biraben. Ultra-violet light generation by two frequency doubling steps of a cw titanium-sapphire laser. *Opt. Commun.*, 133:239–244, 1997.
- [21] V.G. Dmitriev, G.G. Gurzadyan, D.N. Nikogosyan. *Handbook of Nonlinear Optical Crystals*. Springer-Verlag, Berlin, 1991.
- [22] Product list of Casix, Inc. at <http://www.casix.com>.
- [23] P.J. Fox, R.E. Scholten, M.R. Walkiewicz, and R.E. Drullinger. A reliable, compact, and low-cost Michelson wavemeter for laser wavelength measurements. *Am. J. Phys.*, 67:624–630, 1999.
- [24] J.L.M. Hagen. Aerostatische lagers. *Bedrijfsmechanisatie-Kern Contactblad*, 29:51–59, 1980.
- [25] R. Snoeys and F. Al-Bender. Ontwikkeling van verbeterde aerostatische lagers. *De Constructeur*, 9:70–78, 1989.
- [26] D.R. Lide, editor. *Handbook of Chemistry and Physics*. CRC Press, Boca Raton, 1991.
- [27] W. Demtröder. *Laser Spectroscopy*. Springer-Verlag, Berlin, 1981.

Laser-focused atomic deposition

In this chapter we show that laser-focused chromium deposition allows for fabrication of nanostructures with a width below 100 nm. Careful analysis of measured structures revealed a strong influence of surface growth effects on the achievable resolution.

First, our optical setup for laser manipulation of atoms is described. Thereafter we demonstrate laser manipulation of a chromium beam at the ${}^7S_3 \rightarrow {}^7P_4^o$ ${}^{52}\text{Cr}$ resonance. Finally, we present our deposition experiments with laser-focused chromium atoms.

4.1 Optics for manipulation of atoms

Schematic design

To prepare the laser beams for the experiments, we use an optical arrangement as schematically shown in Fig. 4.1. Because the center of the viewport of the main vacuum chamber [Fig. 3.22(b)] and thus the center of the *in vacuo* optics [Fig. 3.23(b)] are at a height of 330 mm above the optical table, the optical setup is built on a 600×450 mm/45 mm-thick honeycomb breadboard supported by four $\varnothing 25$ mm/230 mm-long stainless-steel rods. The laser beam is adjusted at a height of 55 mm above the breadboard (the molasses height) using a periscope PS1. Then, it passes a half-wave plate HWP and a polarization beam splitter PBS. This configuration allows for adjustment of the laser power in the focusing beam by changing the HWP angle.

Our laser system is held at a frequency that results in optimal performance of the molasses. Therefore, the SW focusing laser beam is shifted in frequency using a 200 MHz acousto-optical frequency shifter.

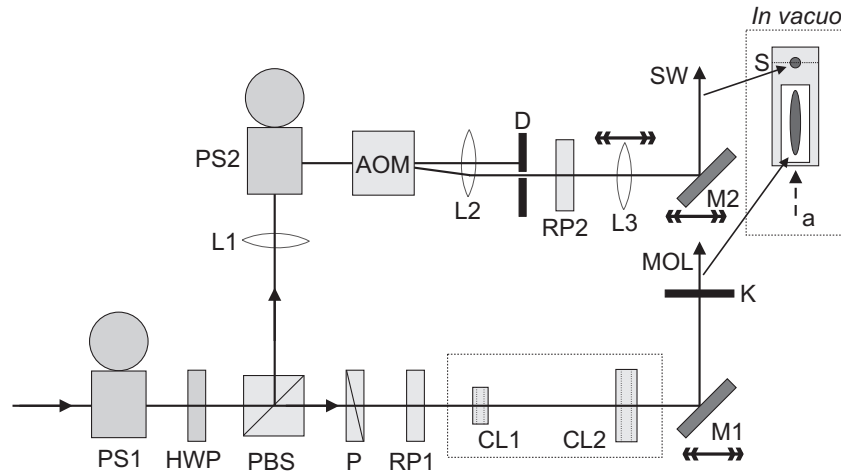


Figure 4.1: Schematic of the optical setup for transverse laser collimation and focusing of atoms. PS1, PS2 – periscopes; HWP – half-wave plate; PBS – polarization beam splitter; P – polarizer; RP1, RP2 – retardation plates (either half-wave or quarter-wave plates); CL1, CL2 – cylindrical lenses (cylindrical beam expander); M1, M2 – mirrors; K – knives for fine adjustment of the molasses (vertical) beam size; L1, L2, L3 – spherical lenses; AOM – acousto-optical modulator; D – diaphragm. Laser beams: SW – standing-wave; MOL – molasses. *In vacuo*: A – atoms; S – substrate surface.

Optical molasses beam

The laser power in the molasses beam is set by a polarizer P and its polarization state is adjusted using a retardation plate RP1. RP1 can be either a half- or a quarter-wave plate, depending on whether a Sisyphus or a cork-screw polarization gradient scheme will be desired. Then, the beam is expanded in the vertical direction by an expander consisting of two cylindrical lenses OC1 and OC2, respectively, with focal lengths of -12.7 mm and 150 mm. The expansion factor is about 12 and the horizontal and vertical $1/e^2$ full intensity widths of the laser beam are 4 mm and 30 mm, respectively.¹ Then, the beam is folded onto the *in vacuo* optics by a mirror M1 ($\varnothing 50$ mm) mounted on a translation stage. Finally, the beam is retro-reflected after passing the *in vacuo* quarter-wave plate. The vertical span of the molasses can

¹The blue beam exiting the doubling cavity is collimated by a 350 mm positive lens. In front of the cylindrical expander this beam is astigmatic and its $1/e^2$ horizontal and vertical full widths are 4 mm and 2.5 mm, respectively. This astigmatism is not corrected for yet because it does not crucially disturb our experiments. Should a correction be desirable in the future, we have designed, but not yet implemented, a prism corrector which will result in a beam with astigmatism less than 2%.

be adjusted by two knife-edges K.

Focusing laser beam

The SW focusing laser beam is reflected from PBS. It is then focused by a 200 mm positive lens L1 through a periscope P2 (a height of 112 mm above the breadboard) onto an acousto-optical modulator AOM (Brimrose, TEM-200-50). The AOM shifter is mounted on a stage with x , y and z translational and θ and ϕ rotational degrees of freedom. This construction allows for careful adjustment of the AOM in order to optimize its diffraction efficiency. Our AOM is optimized for an operation at either +200 MHz or -200 MHz (80% diffraction efficiency) and exhibits a 3 dB modulation bandwidth of 50 MHz. After the laser beam passes the modulator, it is re-collimated by a 125 mm lens L2. The first order diffracted beam is then selected by a diaphragm D. The polarization of the focusing beam is set by a retardation plate RP2 which can be either a half- or a quarter-wave plate. A 400 mm lens L3 is used to focus the beam onto the *in vacuo* mirror through a mirror M2. Both L3 and M2 are mounted on a translation stage. The SW laser field is created by reflecting the beam on itself.

4.2 Laser manipulation of chromium atoms

In Sec. 4.2.1 we demonstrate laser collimation of a chromium beam in a one-dimensional optical molasses. In Sec. 4.2.2 we discuss the effect of a laser SW tuned 200 MHz above the chromium resonance.

4.2.1 One-dimensional optical molasses

We use the ${}^7S_3 \rightarrow {}^7P_4$ ${}^{52}\text{Cr}$ resonance at 425.55 nm. Because the mass of a chromium atom is 52 amu, the recoil velocity $v_r \simeq 1.8$ cm/s. The natural linewidth $\Gamma/2\pi \simeq 5$ MHz (corresponding to a lifetime of 200 ns) then implies an atomic acceleration of 9×10^4 m/s². This acceleration is the maximum possible one, assuming a completely saturated atomic transition. In practice the acceleration is less.

Our chromium beam is evaporated from a high temperature effusion cell held at about 1900 K (the most probable atomic velocity of 780 m/s). This beam is mechanically pre-collimated in the transverse direction to a divergence of about 4 mrad. Then, a one-dimensional molasses with a span of only a few cm reduces (in principle) the transverse velocity spread of atoms down to the recoil limit. For detailed analysis of optical molasses and their limitations we refer to [1–9].

Velocity distributions, angular distribution and atom flux

In order to quantify the performance of a one-dimensional molasses either the transverse velocity distribution $P(v_x)$ or the angular distribution of atoms $P(\alpha)$ must

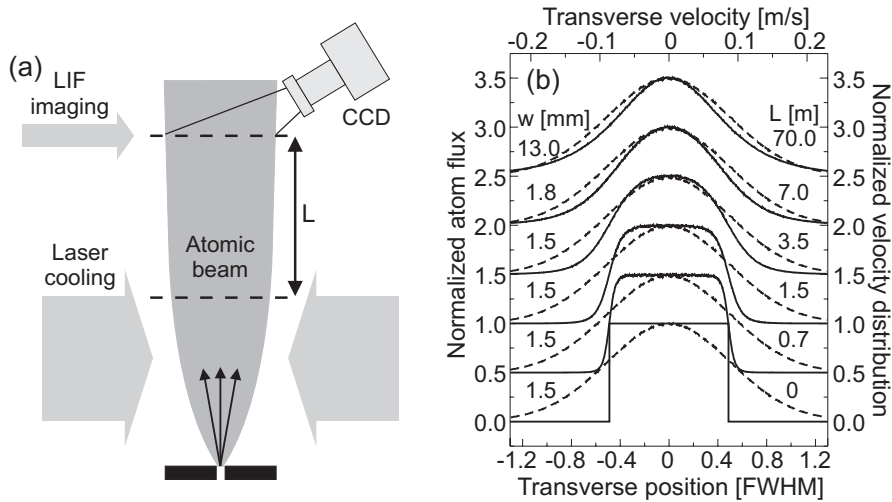


Figure 4.2: Atom flux measurement. (a) Schematic principles. (b) Model calculations. The curves are for convenience offset by 0.5 for subsequent distances L between the “source” and the LIF beam. Transverse velocity distribution (dashed lines) and the atom flux (solid lines) are shown. For more details, see text.

be determined. We note that $P(\alpha)$ depends on $P(v_x)$ and also on the longitudinal velocity distribution $P(v_z)$. In general, however, knowing either two of these three distribution does not allow to determine the third one. This is because transverse and longitudinal velocities might be correlated even after the atoms exit the molasses.

The narrower $P(v_x)$ [$P(\alpha)$] the narrower the atom flux distribution $f(x)$ at a large distance L from the molasses. Therefore, the laser parameters can be adjusted to optimize the molasses performance by measuring $f(x)$ in the detection chamber of our vacuum system. We use laser-induced fluorescence (LIF) and detect $f(x)$ with a charged-coupled device (CCD) camera [Fig. 4.2(a)]. Assuming atoms collimated to or below the Doppler limit, the profile of the measured fluorescence image corresponds to $f(x)$.

Even though $P(v_x)$ correlates with $f(x)$ to some extent, the functional form of both distributions is different. This is because $f(x)$ correlates also with $P(v_z)$. To demonstrate this we performed computer modeling of $f(x)$ for different distances L . The atoms emerge randomly from a 1.5 mm opening with all positions being equally likely. Furthermore, the velocities v_x and v_z are assumed to be non-correlated and are generated following Gaussian and Maxwell-Boltzmann statistics with corresponding temperatures $T_c = 37 \mu\text{K}$ and $T_o = 1900 \text{ K}$, respectively. Our results are shown in

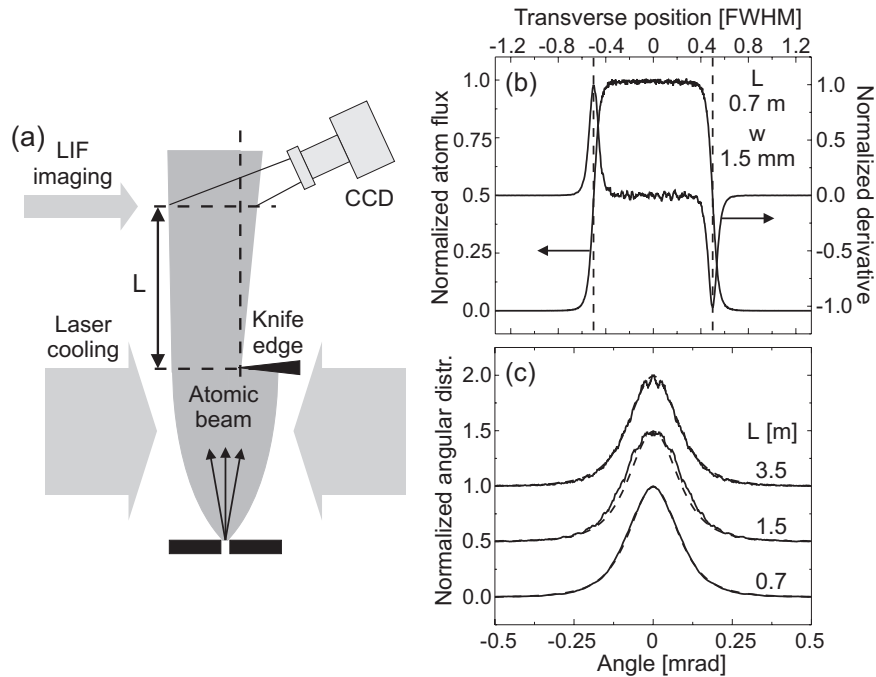


Figure 4.3: Knife-edge technique. (a) Schematic principles. (b) and (c) Model calculations. (b) Atom flux at $L = 0.7$ m [see Fig. 4.2(b)] and its numerical derivative with respect to the transverse position. (c) Reconstructed angular distribution (solid lines) and expected theoretical distribution (dashed lines). The curves are for convenience offset by 0.5 for subsequent distances L between the “knife-edge” and the probe beam. For more details, see text.

Fig. 4.2(b). We see that $f(x)$ approximates $P(v_x)$ relatively well only at distances L which are too long to meet experimental requirements.

Knife-edge technique

To quantify our molasses we implemented the knife-edge technique proposed by Scholten *et al.* [10]. This technique is schematically illustrated in Fig. 4.3(a). It relies on detecting the atoms in the shadow of a sharp object – a knife-edge. The distance between the knife-edge and the molasses exit plane should be as short as possible. This is because the transverse atomic positions and velocities must be non-correlated in order to obtain results valid across the whole atom beam. Correlation

between x and v_x becomes stronger the longer the propagation distance of atoms.

The knife-edge technique enables us to determine only $P(\alpha)$. The reconstruction procedure relies on the fact that $P(\alpha)$ is related to the atom beam profile $f(x)$ in the shadow of the knife-edge via [10]

$$P(\alpha) \propto L \frac{df(x)}{dx}, \quad (4.1)$$

where L is the distance between the knife-edge and the detection plane.

Now, we use the profiles from Fig. 4.2(b) and demonstrate reconstruction of $P(\alpha)$. Either of the two edges of the opening from which the atoms exit forms a knife-edge. Following Eq. (4.1) we first differentiate $f(x)$ with respect to x . The result for $L = 0.7$ m is shown in Fig. 4.3(b). Secondly, the left half of the positive peak (or the right half of the negative peak) is symmetrized and the x -axis is re-scaled by a factor of L . The resulting $P(\alpha)$ is shown in Fig. 4.3(c) for $L = 0.7, 1.5$ and 3.5 m. It is compared with the dependence (dashed lines)

$$P(\alpha) \propto \frac{\alpha_0^4}{[4(\sqrt{2}-1)\alpha^2 + \alpha_0^2]^2}, \quad (4.2)$$

expected under the assumption of uncorrelated transverse and longitudinal velocities which respectively follow the Gaussian and Maxwell-Boltzmann statistics [10]. In our case, the FWHM divergence angle $\alpha_0 \simeq 0.18$ mrad [see also Eq. (2.11)].

Angular resolution of the detection unit

In our vacuum system (Fig. 3.22) the distance between the knife-edge and the detection laser beam is 560 ± 2 mm. The distance between the knife-edge and the exit plane of the molasses is about 150 mm. Now, for the knife-edge technique to be applicable to our experiments we must assume that the laser cooling is uniform over a small region of space at the center of the molasses. The width of this region is given by the width of the atom flux distribution at the detector area times the demagnifying factor $150/560 \simeq 0.27$.

The fluorescent beam image is taken with a CCD camera (TM565, PULNiX). This camera has a dynamical range of 8 bits and an array of 512×512 pixels. The closest distance between the atom beam center and the camera objective at which the beam image still appears sharp is 85 mm. The resulting spatial resolution is then $30 \mu\text{m}$ per pixel. This calibration implies that the angular resolution of our detection unit is ± 0.10 mrad. It should also be mentioned that the $1/e^2$ full intensity widths of the probe laser beam along and across the atom beam are 4 mm and 2.5 mm, respectively. This fact also negatively influences our measurements because of the depth of field of our imaging optics. The error budget is nevertheless dominated by the poor angular resolution.

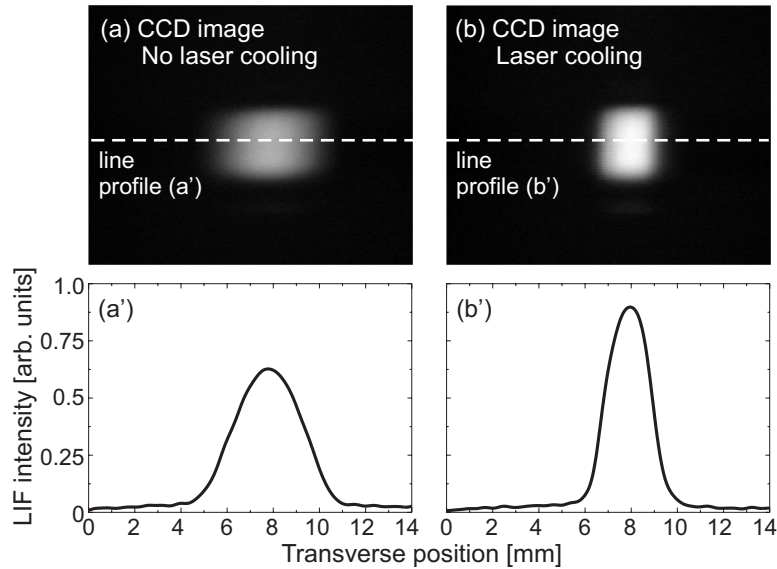


Figure 4.4: Laser collimation of a chromium beam – first observation in Nijmegen (March 28, 2000). CCD detected LIF image of the chromium beam: (a) no laser collimation applied and (b) laser collimation applied. (a') and (b') show the line profiles measured at the position of the dashed lines in (a) and (b), respectively.

Molasses alignment

The laser beam is directed onto the *in vacuo* optics and reflected on itself. The atom beam profile as taken by the CCD camera is monitored. Then, the laser frequency is tuned by gently translating the stabilization unit. As this frequency gets in the vicinity of the atomic resonance, the atom beam profile is disturbed. Thereafter, the molasses alignment and the laser frequency are optimized to obtain the narrowest possible atom beam profile.² We note that the polarization of the incoming and reflected beams are kept parallel because at the moment we apply only the simplest Doppler scheme.³

²In the following we do not measure the detuning of the laser frequency from the atomic resonance. Nevertheless, we can estimate that the molasses are optimized for a detuning ranging from -5 MHz to -2.5 MHz.

³Polarization gradient methods require degenerate magnetic sublevels in the atomic ground state hence even the Earth's magnetic field must be compensated for. However, to date we have not accounted for this. Videlicet, Anderson *et al.* [11] reported about their chromium experiment: “As

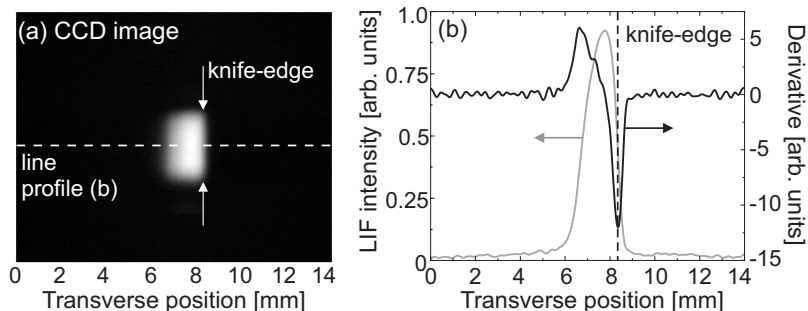


Figure 4.5: Knife-edge measurement. (a) CCD detected LIF image of the collimated chromium beam [Fig. 4.4(b)] part of which was blocked with the knife-edge. (b) Line profile (grey line) and its derivative (black line). The FWHM beam divergence evaluates to 0.65 ± 0.10 mrad.

Laser collimation of a chromium beam

In Figs. 4.4(a) and (a') we show the chromium beam image and the beam profile, respectively, with no laser molasses applied. Our first observation of laser collimation of a chromium beam is presented in Figs. 4.4(b) and (b'). The molasses contained a power of 50 mW and had a vertical span adjusted to 25 mm ($1/e^2$ intensity full width). The compression factor – the ratio between the FWHM widths of the “hot” and the “cold” atom beam – evaluates to about 2.7.

In order to determine the FWHM divergence α_0 of the chromium beam we performed a knife-edge measurement. The result is shown in Fig. 4.5(a). The distance between the knife-edge and the atom beam center (in the plane of the knife-edge) was $350 \pm 30 \mu\text{m}$. The obtained profile shown in Fig. 4.5(b) was numerically differentiated averaging across 7 points. Twice the half-width at half-minimum of the negative peak (in the knife-edge shadow) of this derivative corresponds to $\alpha_0 = 0.65 \pm 0.10$ mrad. In the approximation of Eq. (2.11) this results in a transverse beam temperature $T_c = 485 \pm 150 \mu\text{K}$. The Doppler limit for chromium atoms is $120 \mu\text{K}$ as follows from Eq. (1.5).

From the first experiment presented in Figs. 4.4 and 4.5 our alignment procedure improved. The CCD camera is now connected to a computer and the beam divergence

there are some assumptions that go into deriving the transverse velocity spread from the observed angular width of the atom beam, we have taken the additional experimental step of varying the amount of collimation and observing the feature width of the deposited lines. No variation of the feature width was seen over a range of collimations from 0.16 mrad to 0.37 mrad.” Because at present the conditions in our experiment are similar to those in [11] and because we also attempt to grow chromium structures, the step of going towards the Sisyphus molasses is not necessary.

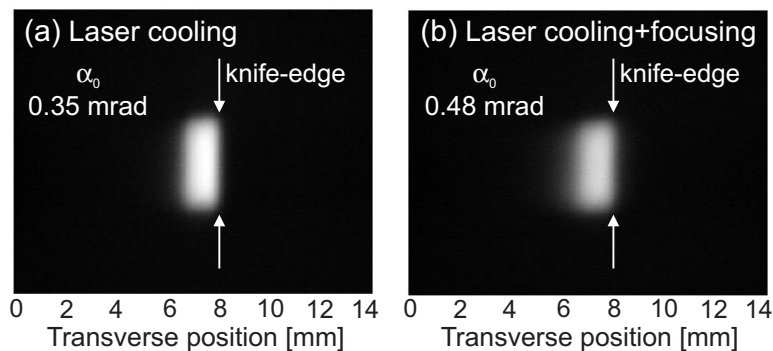


Figure 4.6: Observation of channeling of a chromium beam. The knife-edge was slid into the beam. LIF images: (a) Laser-collimated chromium beam ($\alpha_0 = 0.35 \pm 0.10$ mrad). (b) Channeling in a laser standing wave ($\Delta/2\pi \simeq 200$ MHz, $P = 50$ mW, $\alpha_0 = 0.48 \pm 0.10$ mrad).

is evaluated in real time. We routinely reach FWHM beam divergences down to 0.35 ± 0.10 mrad. We note that the best laser collimation angles ever observed with a chromium beam were 0.16 ± 0.02 mrad [10, 11].

4.2.2 Channeling of atoms in a laser standing wave

The transverse velocity distribution $P(v_x)$ and the angular distribution $P(\alpha)$ are considerably altered when a laser-collimated atom beam crosses a laser SW tuned near the atomic resonance. Because the atom flux $f(x)$ correlates with $P(v_x)$ [$P(\alpha)$], we use the atom beam image to align the SW beam.

Standing wave alignment

The focusing laser beam detuned by 200 MHz from the molasses frequency is folded via the M2 mirror (Fig. 4.1) onto the *in vacuo* mirror and is reflected on itself. The lens L3 is translated in order to place the SW beam focus (a $1/e^2$ radius along the atom beam propagation direction z of about $100 \mu\text{m}$) onto the *in vacuo* mirror. The position of M2 is adjusted such that the SW beam crosses the atom beam. Thereafter, the alignment of the SW is tweaked until the largest symmetric distortion of the atom flux profile is seen in the detection chamber.

Observation of channeling of a chromium beam

Fig. 4.6(a) shows a chromium beam laser-collimated to $\alpha_0 = 0.35 \pm 0.10$ mrad. The molasses contained a power of 40 mW and had a vertical span of 25 mm. We exposed the chromium beam to a 50 mW laser SW with $\Delta/2\pi \simeq 200$ MHz. The beam profile became distorted as demonstrated in Fig. 4.6(b). The average beam divergence increased to $\alpha_0 = 0.48 \pm 0.10$ mrad. We note that because of the size of the probe laser beam, the camera averages about 2.5 mm across the chromium beam. Therefore, the measured divergence does not exactly correspond to the divergence of the atoms channeled through the SW beam.

4.3 Chromium nanostructures

In this section we show that chromium atoms focused in a laser SW can be used to grow high-resolution nanostructures. In Sec. 4.3.1 the results obtained in Nijmegen are presented. Sec. 4.3.2 deals with experiments carried out at the National Institute of Standards and Technology (NIST) in Gaithersburg (MD, USA).⁴

4.3.1 Work carried out in Nijmegen

Alignment procedure

The substrate is fixed onto the glass oblong (sample holder) of the manipulator with two phosphor-bronze springs [Fig. 3.23(b)]. These springs push the sample against the oblong face. The substrate is placed onto the sample holder *ex vacuo* because there is no sample transfer system yet. The oblong is aligned with respect to the *in vacuo* mirror by illuminating it with a laser beam at normal incidence. The resulting reflections (from the mirror and the oblong) must overlap. The substrate is then perpendicular to the mirror surface to within ± 0.1 mrad. The manipulator is thereafter carefully bolted onto the flange and the vacuum system is pumped down.

With the manipulator in the shadow of the last collimating diaphragm, the molasses and the SW laser beam are aligned. The SW beam passes through the groove in the glass oblong beneath the substrate. The manipulator is then moved towards the atoms until the oblong front face touches the chromium beam. The shutter between the stabilization and main chambers is closed. From this moment the atom beam is not seen in the detection chamber anymore.⁵ The manipulator is further translated into a position where the atom beam can freely pass through the vertical groove in

⁴I have spent two summers in 1998 and 2000 with Dr. J.J. McClelland (NIST physicist). During my first stay we explored the growth phenomena in laser-focused chromium deposition. Also, we worked on some topics related to metrology applications of laser-focused nanostructures.

⁵Further alignment of the *in vacuo* optics might be necessary. To this end laser beams reflected from the *in vacuo* optics are used.

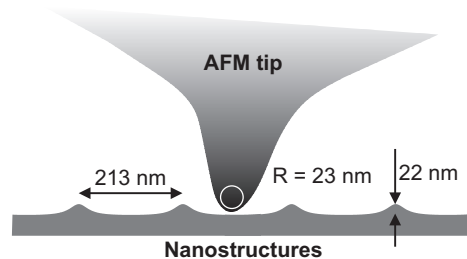


Figure 4.7: Schematic illustration of an AFM measurement on laser-focused chromium nanostructures.

the oblong. Thereafter, the vertical position of the *in vacuo* optics is adjusted for the SW focusing beam to be cut by the substrate surface at the center (or at any other desired location). The shutter is open for the time of deposition.

AFM imaging of laser-focused nanolines

To image our samples we use an atomic force microscope (AFM) operating at ambient conditions (Dimension 3100 AFM, Digital Instruments). The AFM resolution is limited by the tip and also by the sample under investigation. In Fig. 4.7 a situation is sketched that might be seen as a typical representation of our AFM measurements on laser-focused nanostructures. The tip apex itself is an object with a radius of curvature up to several tens of nm. Therefore, the image can differ from the real structures.

If only the tip geometry played a role, the tip effects could be removed using standard geometrical algorithms for surface reconstruction, such as dilation (both the tip and the structure shape are known), erosion (only one shape is known) and blind reconstruction (neither shape is known) [12]. However, there is an intricate set of forces an AFM measurement can be influenced by. In addition, conducting experiments at ambient conditions, water vapor condensates in the tip-surface gap. Therefore, even after applying a reconstruction procedure, there might be some artifacts present in the image. We must be aware of these artifacts, even though in the following no treatment to the images (acquired in Nijmegen) is done.

First experiment: chromium lines on $\text{SiO}_2/\text{Si}(100)$

Our first sample was grown onto a standard silicon wafer [$\text{SiO}_2/\text{Si}(100)$] with dimensions 15×8 mm/0.4 mm-thick. The base pressure in the main vacuum chamber was 4×10^{-8} mbar. The molasses laser beam contained a power of 40 mW and had a span of 25 mm. The resulting FWHM divergence of the chromium beam was

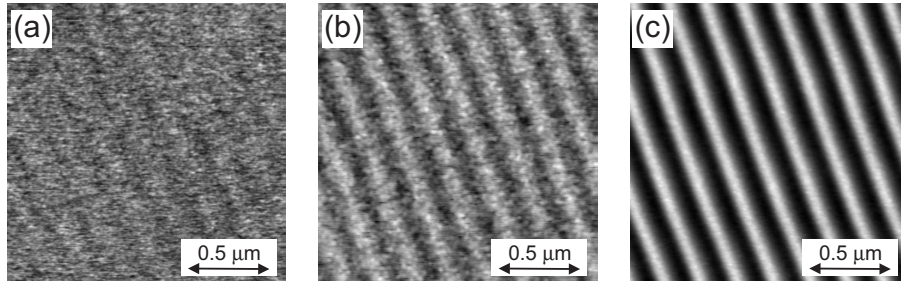


Figure 4.8: AFM scans of laser-focused chromium on $\text{SiO}_2/\text{Si}(100)$: the first experiment in Nijmegen (May 3, 2000). y – position along the lines (laser beam center: $y \simeq 0$). z – AFM vertical range. (a) $y = 190 \mu\text{m}$, $z = 10 \text{ nm}$. (b) $y = 140 \mu\text{m}$, $z = 20 \text{ nm}$. (c) $y = 0 \mu\text{m}$, $z = 30 \text{ nm}$. Laser SW: $P = 60 \text{ mW}$, $W_0 \simeq 100 \mu\text{m}$, $\Delta/2\pi \simeq 200 \text{ MHz}$. Atomic beam: $T_o \simeq 1900 \text{ K}$, $\alpha_0 = 0.35 \pm 0.10 \text{ mrad}$. Geometry: Laser beam cut at the center by the substrate. Deposition time: 20 minutes.

$0.35 \pm 0.10 \text{ mrad}$. The SW focusing beam was detuned from the chromium resonance by $\Delta/2\pi \simeq 200 \text{ MHz}$. It contained a power of 60 mW and was focused to a $1/e^2$ radius (along z) of about $100 \mu\text{m}$. We note that higher focusing powers result in a strong channeling effect and, therefore, in a less critical substrate positioning. The SW laser beam was cut by the substrate roughly at its center. The effusion cell was operated at 1900 K. The deposition took 20 minutes.

Three $2 \times 2 \mu\text{m}$ AFM scans, corresponding to three different y -positions along the lines, are shown in Fig. 4.8. Already at a distance $y = 190 \mu\text{m}$ [Fig. 4.8(a)] from the laser beam center (located at $y \simeq 0$) the surface is periodically modulated with a spatial period of 213 nm. The surface morphology is granular. The density of grains is higher at the SW nodes and lower at the SW antinodes. At $y = 140 \mu\text{m}$ [Fig. 4.8(b)] the surface modulation is more pronounced. The AFM scan acquired at the laser beam center is shown in Fig. 4.8(c). The lines are apparently continuous and the surface does not appear granular. The grating is very regular with no apparent defects.

In Fig. 4.9 the FWHM width w and the modulation depth h (peak-to-valley distance) versus y are shown. We note that w is subjected to more scatter than h . This is because w is more sensitive to tip effects than h . At $y \simeq -25 \mu\text{m}$ the noise in w increased considerably, most likely due to a host particle picked up by the tip. The smallest w measured on the sample is below 100 nm and the largest h is about 20 nm. Furthermore, the line pattern persists for almost 0.4 mm along y . We note that in the x -direction (perpendicular to the lines) the nanostructures are present across the

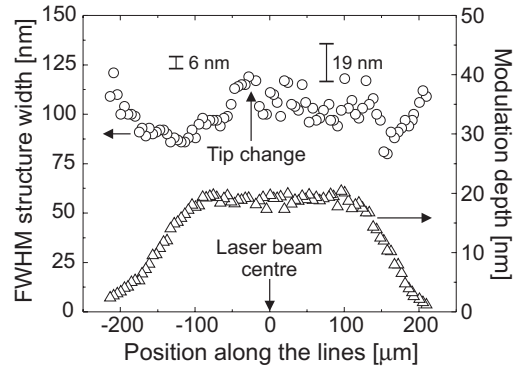


Figure 4.9: Chromium lines on $\text{SiO}_2/\text{Si}(100)$. Measured FWHM width (circles) and modulation depth (triangles) vs. y . Error bars of FWHM width are estimated from the maximum distance between the next following points within intervals that appear flat.

whole 1.5×1.5 mm chromium patch.

A three-dimensional plot of the AFM data from Fig. 4.8(c) is shown in Fig. 4.10(a). Furthermore, in Fig. 4.10(b) a profile (black line) is presented that was obtained by averaging 250 nm along the lines. It is seen that the structure is smooth, periodic, with no pronounced difference from line to line. Such a parallelism is expected because of the intrinsic properties of the laser-focusing process. We note that the uniform background level is undetermined. The average chromium film thickness must be measured before any estimation can be made.

Using the semiclassical model of a SW atom lens developed in Sec. 2.1, much narrower nanolines than observed were expected. In Fig. 4.10(b) the modeled profile (grey line) is shown. We set the calculation parameters to: the laser power $P = 60$ mW, the $1/e^2$ laser beam radius $W_0 = 100$ μm , the detuning $\Delta/2\pi = 200$ MHz, the oven temperature $T_o = 1900$ K and the FWHM chromium beam divergence $\alpha_0 = 0.45$ mrad (corresponding to the worst possible situation in our experiment). The theoretical profile exhibits a width of 35 nm, a factor of 2.9 better than observed in the experiment.

It is interesting to note that the laser parameters and the actual alignment can be controlled very well in our experiment. In spite of this fact the experimental and theoretical results differ considerably. Therefore, growth of our structures must be influenced also by other than only atom-photon interaction processes. Observation of grain formation on the surface indicates that surface growth and diffusion phenomena play a crucial role.

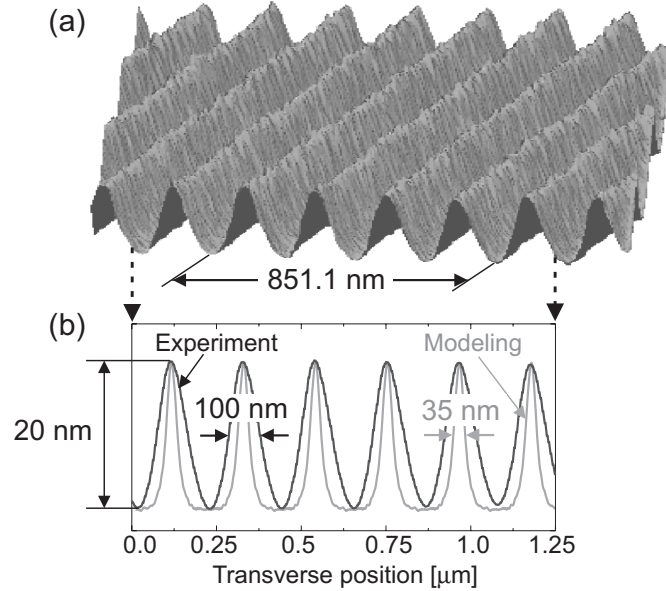


Figure 4.10: (a) Three-dimensional plot of chromium nanostructures from Fig. 4.8(c). (b) Black line – nanostructure profile averaged 250 nm along the lines. Grey line – modeled shape ($P = 60$ mW, $W_0 = 100$ μm , $\Delta/2\pi = 200$ MHz, $T_o = 1900$ K, $\alpha_0 = 0.45$ mrad). The absolute background level is undetermined.

Chromium lines on ITO

In order to illustrate the general trends observed in our experiments, in Fig. 4.11 we show chromium nanolines grown on an ITO (indium-tin-oxide) substrate. The base pressure in the main vacuum chamber was 5×10^{-8} mbar. A 40 mW molasses with a span of 25 mm collimated the chromium beam to $\alpha_0 = 0.35 \pm 0.10$ mrad. The laser SW parameters were adjusted to $P = 14$ mW, $\Delta/2\pi \simeq 200$ MHz and $W_0 \simeq 100$ μm (along z). The substrate was aligned to cut the SW at the center. The effusion cell was operated at 1900 K. The deposition time was 22 minutes.

In Figs. 4.11(a) and (b) ($y = 180$ μm and $y = 140$ μm , respectively) granular morphology of the lines (in the tail of the laser beam intensity) is demonstrated. The grains collapse into apparently continuous lines at a position $y \simeq 80$ μm as presented in Fig. 4.11(c). Such a continuous pattern persists up to $y \simeq -80$ μm .

In Fig. 4.12 the FWHM structure width w and the modulation depth h versus y are shown. We note that the dependence of w on y is “flatter” than in Fig. 4.9. This is a consequence of lower SW laser power in the ITO experiment compared with

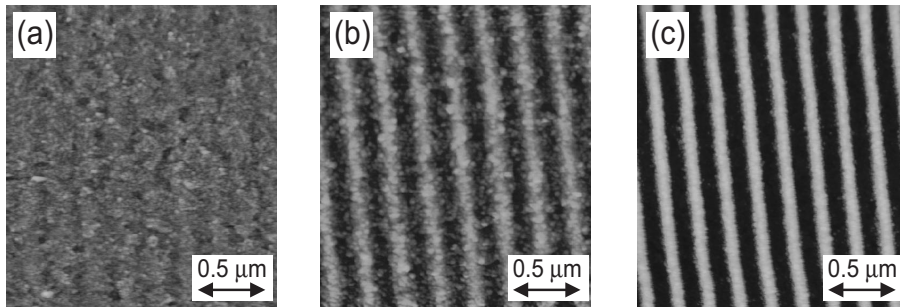


Figure 4.11: Chromium lines on ITO as observed by AFM. Line profiles at different positions along the lines y measured relative to the estimated position of the laser beam center. (a) $y = 180 \mu\text{m}$ and the vertical range $z = 20 \text{ nm}$. (b) $y = 140 \mu\text{m}$, $z = 20.8 \text{ nm}$. (c) $y = 80 \mu\text{m}$, $z = 29 \text{ nm}$.

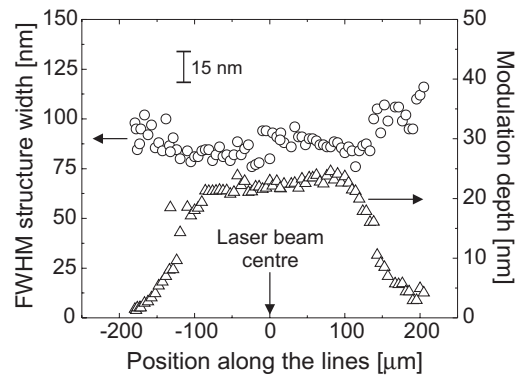


Figure 4.12: Chromium lines on ITO. Measured FWHM width (circles) and modulation depth (triangles) vs. y . Error bar of FWHM width is estimated from the maximum distance between the next following points within intervals that appear flat.

the first experiment. When using high laser powers the narrowest atom flux can be observed away from the SW center along y (see discussion in Sec. 2.1.4). Furthermore, we see from Fig. 4.12 that the y -interval within which the lines are apparently present is shorter than in Fig. 4.9. This can again be explained with a lower SW laser power, that is with an overall lower focusing intensity. We note that the smallest w seen in our ITO experiment is about 75 nm and the largest h is 25 nm.

We modeled the structure profile for the parameter settings of the ITO experiment ($P = 14$ mW, $W_0 = 100$ μm , $\Delta/2\pi = 200$ MHz, $T_o = 1900$ K and $\alpha_0 = 0.45$ mrad). The laser-focused atom flux exhibited an FWHM width of 30 nm. Nevertheless, the narrowest width seen in Fig. 4.12 is a factor of 2.5 larger.

Conclusions

The first experiments with laser-focused chromium deposition carried out in Nijmegen were intended in the first place to test the performance of our system. In this section we presented results of only two first deposition runs. However, the general trends observed on the first two samples were seen on all samples we have grown. In total, six depositions were carried out and the obtained results were consistent. Our system is capable of reproducible fabrication of laser-focused chromium nanolines that exhibit a resolution below 100 nm.

We have shown that the ultimate abilities of our technique are dictated not only by the ultimate properties of a SW atom lens but also by surface growth phenomena. In order to perform more systematic studies, our samples must be grown in a controlled UHV environment. At present, we are undertaking important steps to achieve this goal in the near future.

4.3.2 Work carried out at NIST (Gaithersburg, MD, USA)

NIST facility and deposition experiment

The vacuum system consisted of a commercial high-temperature effusion cell, a laser stabilization chamber, a main chamber and a detection chamber. The main chamber and the effusion cell were ion-pumped. The system was built horizontally on an optical table. The pressure in the main chamber, while depositions were in progress, was typically 10^{-8} mbar. The oven was operated at 1800–1900 K.

The sample holder was mounted on a commercial vacuum manipulator providing x , y and z translations, as well as rotation and tilt. The *in vacuo* optics included a mirror, a quarter-wave plate and an oblong (as a sample holder). The oblong side facing the mirror was coated for 56% reflection for 425 nm. Together with the mirror, it formed an interferometer. The sample position with respect to the mirror was actively stabilized by servo-locking the length of the interferometer.

Laser light at 425 nm was produced using a commercial ring dye (stilbene-3) laser (Coherent 899-21) pumped with a 4 W ultra-violet argon-ion laser (Spectra Physics 2045). Approximately 300 mW at 425 nm was available for the experiment. The laser frequency was stabilized onto the ${}^7S_3 \rightarrow {}^7P_4^o$ ${}^{52}\text{Cr}$ transition using the split-photodiode technique.

The laser was oscillating at the frequency of the SW focusing beam about 495 MHz above the chromium transition. The molasses, the stabilization and the detection laser beams were frequency down-shifted using a 500 MHz acousto-optical modulator. The $1/e^2$ intensity full widths of the molasses beam were adjusted to approximately 2×15 mm. Three orthogonal pairs of Helmholtz coils were used to bring the magnetic field in the laser-atom interaction region to $0 \pm 2 \mu\text{T}$. A one-dimensional Sisyphus (lin \perp lin) molasses was applied. The atom beam divergence was measured with the knife-edge technique. The distance between the molasses and the knife-edge was approximately 120 mm and the distance between the knife-edge and the detection laser beam was 660 mm. The FWHM divergence angle of the chromium beam was evaluated to 0.16 ± 0.02 mrad. The SW laser beam was focused to a $1/e^2$ beam radius of 60 μm . It contained a power of 20 mW and was cut by the substrate at the center.

Chromium lines were grown onto polished Si(100) substrates with a native oxide layer. The deposition time was varied in order to study the optimum experimental conditions to obtain the narrowest possible structure width. The NIST group reported on these deposition runs in [11].

For more detailed description of the NIST facility and experiment, see [10, 11].

Surface growth studies

Our modeling results presented in Chap. 2 indicate that any changes of the structure profile with increasing deposition time can be attributed to surface growth phenomena, provided the SW focusing conditions do not drastically change with increasing film thickness. Here, we analyze the evolution of experimental profiles with the chromium layer growing thicker using a phenomenological model. Such an analysis allows us to gain a somewhat deeper insight into the role of surface growth effects in laser-focused nanofabrication. The ultimate aim is a better understanding of the growth behavior of laser-focused chromium.

Experiment

The samples used in this study were the same as those investigated by Anderson *et al.* [11]. The average surface coverage as well as the absolute background level (the substrate-to-valley height) were determined by respectively etching the chromium film in the regions covered and uncovered by the SW laser beam. The vertical distance between the chromium and the substrate surface was determined.

The grown structures were analyzed with a tapping-mode AFM operating at ambient conditions (Dimension 3000, Digital Instruments). To account for tip effects, the average AFM line profiles were eroded using an algorithm developed by Villarrubia [12]. A tip model was obtained by imaging a sharp grating that consisted of triangular silicon features with a nominal width of less than 10 nm. We again note that a geometrical approach to surface reconstruction is only an approximation. Therefore, either the raw or the eroded data are only an approximation to the real situation. The erosion procedure leads most likely to underestimation of the structure width.

In Fig. 4.13(a) the average, eroded structure profiles are shown for six different chromium coverages of 1.9, 3.3, 4.8, 8.0, 15.4 and 23.0 nm, respectively. For thicker films the FWHM structure width increases quite dramatically with increasing chromium film thickness (see also [11]). The experimental profiles are much broader and exhibit a smaller contrast than the calculated atom flux that corresponds to our experimental arrangement [see Fig. 2.9]. For example, the sample with an average coverage of 3.3 nm is characterized by an FWHM width $w \simeq 30$ nm, a modulation depth $h \simeq 3$ nm and a contrast $\zeta \simeq 1.2$. For the sample with an average coverage of 23.0 nm, these quantities change dramatically to $w \simeq 66$ nm, $h \simeq 37$ nm and $\zeta \simeq 3.3$. In contrast, our atom-optical calculations revealed an FWHM of only 13 nm and a contrast of 7.

Description of the phenomenological model

In the limiting case of diffusion dominated growth, the partial differential equation which describes the growth is of the Edwards-Wilkinson type [13]. Supposing a one-dimensional focusing geometry with the laser-focused atom flux denoted by $f(x)$, the surface height $h(x, t)$ is driven by the diffusion equation written as

$$\frac{\partial h(x, t)}{\partial t} = f(x) + \sum_{i=1}^{\infty} A_i \frac{\partial^{2i} h(x, t)}{\partial x^{2i}}, \quad (4.3)$$

where t is the time and A_i is the i -th order diffusion coefficient. The presence of only even partial derivatives with respect to x is a consequence of the intrinsic symmetry of the problem. The solution to Eq. (4.3) is readily found in the Fourier space. The Fourier cosine coefficients of the height $h_k(t)$ are given by

$$h_k(t) = \frac{f_k}{C_k} [\exp(C_k t) - 1], \quad (4.4)$$

where

$$C_k = \sum_{i=1}^{\infty} (-1)^i A_i k^{2i}. \quad (4.5)$$

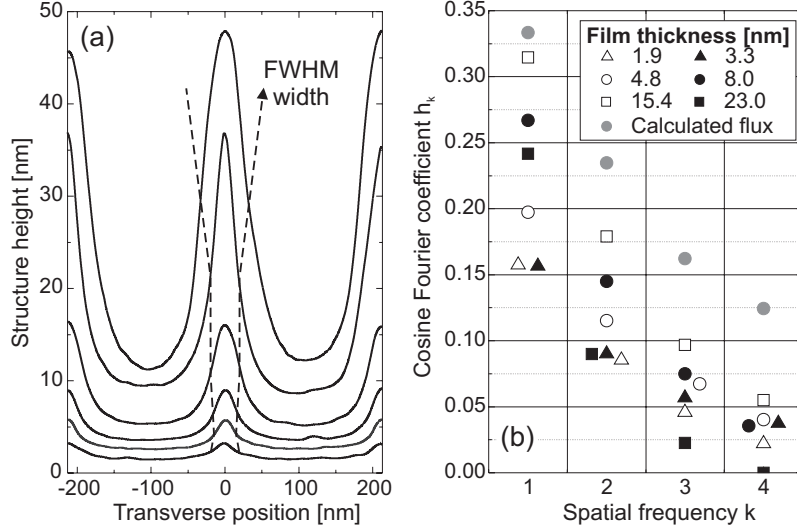


Figure 4.13: Analysis of chromium samples grown at NIST. (a) Average line profiles for increasing thickness of chromium (1.9, 3.3, 4.8, 8.0, 15.4 and 23.0 nm). The FWHM structure width increases at higher chromium coverages. (b) Fourier analysis of shapes shown in (a) – first four cosine coefficients h_k are shown. The shapes were normalized such that the dc-term $h_0 \equiv 1$ (corresponding to an average “thickness” of 0.5). Calculated flux – see Fig. 2.9.

Here, f_k is the k -th Fourier cosine coefficient of the laser-focused atom flux. We note that $h_k(t) \rightarrow f_k$ as $t \rightarrow 0$. Moreover, it is in principle possible to extract the diffusion coefficients from experimental profiles provided the linear diffusion theory applies.⁶

Analysis of experimental profiles

We studied the evolution of the Fourier cosine coefficients of the experimental profiles for increasing surface coverage (equivalent to an increasing deposition time). Variation of these coefficients with time can be attributed to surface growth phenomena. Such an analysis permits us to make a distinction between a linear (diffusion dominated) nanostructure growth [Eqs. (4.3) to (4.5)] and a growth with nonlinearities.

The results of Fourier analysis of the shapes from Fig. 4.13(a) and also of the

⁶As an example, the TDS atomistic model (Sec. 2.2.1) is well described with the above equations (we checked for this explicitly). However, the BD models (Sec. 2.2.2) require an additional nonlinear term $\propto [\partial_x h(x, t)]^2$ to be added to the left hand side of Eq. (4.3), herewith hindering an analytical solution.

calculated atom flux are shown in Fig. 4.13(b). All profiles were normalized such that the dc-term $h_0 \equiv 1$. The Fourier coefficients of the structure height h_k (for a given k) strongly depend on the amount of deposited material. Furthermore, h_k is not a monotonic function of the average chromium thickness for all k 's. This indicates that the linear diffusion theory is not applicable to these data. The growth regime is thus nonlinear. Furthermore, the semiclassical atom flux has Fourier coefficients permanently larger than the experimental shapes. Even the lowest spatial frequencies are greatly influenced by phenomena associated with the nanostructure growth.

Taking into account the relatively poor vacuum conditions in our experiments, the structure growth is most likely influenced by incorporation of impurities. Processes like oxidation, carbonization, etc. can dramatically alter the growth regime. Moreover, as the overlayer thickness grows, the growth description might cross-over from one differential equation to another one [13]. This happens even with simple algorithms used to model surface growth. All these effects complicate our data analysis to an unsolvable extent. *Future investigations must therefore aim at UHV growth to assure clearer experimental conditions.*

Laser-focused chromium nanostructures as a metrology standard

Our approach to laser-focused chromium deposition requires a laser frequency strictly referenced to the ${}^7S_3 \rightarrow {}^7P_4$ ${}^{52}\text{Cr}$ transition. The vacuum wavelength of this transition is $\lambda = 425.55292$ nm [14]. Furthermore, the alignment requirements for the substrate, the laser beams and the atom beam are very strict. The total error budget for the period of laser-focused chromium lines was recently estimated by McClelland [15]. He concluded that the distance between the chromium lines fabricated using the NIST facility is determined to within 41 ppm (parts-per-million). This suggests that our chromium lines can be utilized in surface metrology for lateral calibration of scanning probe microscopes.

We fabricated 19 (1.0×0.4 mm) patches of laser-focused chromium onto a $8.4 \times 10.1/3$ μm -thick $\text{SiO}_2/\text{Si}(100)$ substrate. This sample is currently under investigation in the Quantum Metrology Group of the NIST Atomic Physics Division. The aim is to determine the period of the chromium lines by means of X-ray diffraction. The stringent conditions these measurements require for the precision we need prevented us from performing them as up to this day. The efforts are still ongoing. We are convinced that the (average) period of laser-focused chromium nanostructures (fabricated either at NIST or in Nijmegen) is 212.776(9) nm.

4.4 Conclusions

In this chapter we have demonstrated laser collimation, channeling and sub-100 nm focusing of a chromium beam. We have shown that laser-focused deposition is ca-

pable of growth of high-resolution nanostructures. Furthermore, we have provided strong evidence that the nanostructure profile is influenced not only by atom-photon interaction processes but also by surface growth phenomena. Our future work will concentrate on achieving UHV conditions. This will make analysis of experimental data more transparent. Our aim is to combine atom optics with surface science, hopefully leading to new and exciting research directions in physics.

References

- [1] S. Chu and C. Wieman, editors. Laser cooling and trapping of atoms. *J. Opt. Soc. Am.*, B6:2020-2278, 1989.
- [2] C. Cohen-Tannoudji and W.D. Phillips. New mechanisms for laser cooling. *Physics Today*, 43:33–40, 1990.
- [3] A. Aspect, R. Kaiser, N. Vansteenkiste, and C.I. Westbrook. Laser manipulation of neutral atoms. *Phys. Scripta*, T58:69–77, 1995.
- [4] C.C. Bradley and R.G. Hulet. Laser cooling and trapping of neutral atoms. In F.B. Dunning and R.G. Hulet, editors, *Experimental Methods in the Physical Sciences*, volume 29B, chapter 8, pages 129–144. Academic Press, San Diego, 1996.
- [5] S. Chu. The manipulation of neutral particles. *Rev. Mod. Phys.*, 70:685–706, 1998.
- [6] C. Cohen-Tannoudji. Manipulating atoms with photons. *Rev. Mod. Phys.*, 70:707–720, 1998.
- [7] W.D. Phillips. Laser cooling and trapping of neutral atoms. *Rev. Mod. Phys.*, 70:721–742, 1998.
- [8] H.J. Metcalf and P. van der Straten. *Laser Cooling and Trapping*. Springer-Verlag, Berlin, 1999.
- [9] V.I. Balykin, V.G. Minogin, and V.S. Letokhov. Electromagnetic trapping of cold atoms. *Rep. Prog. Phys.*, 63:1429–1510, 2000.
- [10] R.E. Scholten, R. Gupta, J.J. McClelland, and R.J. Celotta. Laser collimation of a chromium beam. *Phys. Rev. A*, 55:1331–1338, 1997.
- [11] W.R. Anderson, C.C. Bradley, J.J. McClelland, and R.J. Celotta. Minimizing feature width in atom optically fabricated nanostructures. *Phys. Rev. A*, 59:2476–2485, 1999.

-
- [12] J.S. Villarrubia. Algorithms for scanned probe microscope: Image simulation, surface reconstruction, and tip estimation. *Res. Natl. Inst. Stand. Technol.*, 102:425–454, 1997.
 - [13] A.L. Barabási and H.E. Stanley. *Fractal Concepts in Surface Growth, 1st Edition*. Cambridge University Press, Cambridge, 1995.
 - [14] National Institute of Standards and Technology. NIST Atomic Spectra Database. <http://physics.nist.gov/AtData/display.ksh>.
 - [15] J.J. McClelland. Error budget for chromium lines fabricated by laser-focused atomic deposition. Unpublished.

Summary

In the frame of this thesis we have developed an experimental facility for laser-focused atomic deposition and have demonstrated the fabrication of chromium nanostructures via atom optics. This technique makes use of light forces which act on the atoms in a near-resonant laser field. A laser-collimated chromium beam is deposited onto a substrate through a laser standing wave. Such an arrangement results in focusing of the atoms in each of the crests or troughs of the laser intensity, respectively depending on whether the laser frequency is tuned below or above the chromium resonance. In both cases, the resulting pattern on the substrate surface is a grating consisting of periodic lines with a pitch of that of the standing wave period. However, the shape of these lines strongly depends on the focusing properties of the standing wave and on surface growth phenomena.

In Chap. 2 we have first analyzed the ultimate abilities of laser-focused atomic deposition as dictated by the focusing properties of a laser standing wave atom lens. The algorithm we have applied to model the process was based on a semiclassical approximation. The Newton equation for the atoms moving in the optical potential was integrated to obtain classical atomic trajectories. The roles of the laser and atom beam parameters were investigated in detail. We have shown that in order to realize high-resolution, high-contrast focusing an extremely high degree of collimation of the atom beam is of crucial importance. Moreover, for a given experimental geometry and a fixed detuning of the laser frequency from the atomic transition the laser power must be adjusted carefully to obtain the narrowest possible features. We have demonstrated that it should be possible to focus a thermal chromium beam to a focal distribution exhibiting a width close to 10 nm. However, after the atoms are deposited onto the substrate surface, the nanostructure profile can be considerably broadened by surface growth effects. To elucidate the underlying physical processes that govern the shape of a laser-focused nanostructure, we have subsequently modeled its growth by applying three different atomistic models of adsorption and diffusion of adatoms on surfaces. We have shown that theoretical predictions of the structure profile depend sensitively on the model used to describe the growth, the parameters chosen within the model and also the amount of deposited material.

The development of our facility for laser-manipulated atomic deposition is reported on in Chap. 3. This facility consists of two main parts – the optical and the vacuum system. We have designed and built a single-frequency laser system intended for manipulation of chromium atoms at the ${}^7S_3 \rightarrow {}^7P_4^o$ ${}^{52}\text{Cr}$ resonance at 425.55 nm. It consists of a titanium-doped sapphire (Ti:Sapph.) laser that produces single-frequency output in the near-infrared region of the optical spectrum at around 850 nm. The infrared laser beam is subsequently doubled in frequency in an external enhancement resonator based on a lithium tri-borate crystal (LBO). At the best performance of the doubling cavity, we were able to produce 550 mW at 425 nm using

a 1.5 W/850 nm pump, corresponding to a conversion efficiency of almost 37%. We have also designed and set up a Michelson wavemeter with an accuracy of 0.001 nm. The moving arm of our wavemeter is based on a novel air-bearing unit that was especially designed for the purpose of high mechanical stability. The split-photodiode technique we use to lock the laser near the chromium resonance was also described. This technique allowed us to suppress the jitter of the blue laser frequency to 0.5 MHz (peak-to-peak) level. Later in the same chapter, we have described our vacuum system and also the *in vacuo* optics (to which the sample holder is connected) and the manipulator.

In Chap. 4 we have tested the performance of our system. Firstly, a chromium beam was collimated to 0.35 mrad applying the simplest laser cooling scheme based on the Doppler effect. Secondly, conservative channeling of atoms in a laser standing wave tuned 200 MHz above the atomic transition was observed. Subsequently, we have deposited chromium onto Si(100) and indium-tin-oxide (ITO) substrates for about 20 minutes. A 1.5×0.4 mm surface area was covered with periodic nanostructures that exhibited a width down to 75 nm at a modulation depth (peak-to-valley height) up to 25 nm. Finally, we have reported on the results obtained in collaboration with the NIST group (Gaithersburg, MD, USA) using their experimental facility. In order to reveal the role of surface growth phenomena in laser-focused atomic deposition, we have studied the nanostructure evolution with increasing chromium film thickness. Although our results prove that surface growth effects crucially limit the ultimate abilities of our technique, the relatively poor vacuum conditions during the experiments prevented us from performing a thorough quantitative analysis.

Our future investigations will therefore aim at assuring an ultra-high vacuum environment. This will help us to gain a deep insight into the processes involved, thereby allowing to push laser-focused nanofabrication to its ultimate limits.

Samenvatting

In dit proefschrift wordt de ontwikkeling van een experimentele opstelling beschreven welke gebruikt wordt voor laser gestuurde atoom depositie. Met behulp van deze opstelling worden nanostructuren van chroom gefabriceerd via atoom optica. De krachten die uitgeoefend worden door licht op atomen in een laser stralings veld (waarvan de frequentie is afgestemd in de naaste omgeving van een atomaire overgang) liggen ten grondslag aan deze methode. Een via laser koeling gecollimeerde bundel chroom atomen passeert een staande laser golf en wordt vervolgens gedeponeed op een substraat. Door de laser frequentie boven of onder de atomaire overgang af te stemmen, worden de atomen in een dergelijke laser configuratie gedwongen (oftewel gefocusseerd) in respectievelijk de pieken of dalen van de lichtintensiteit. In beide gevallen is het resulterende patroon op het substraat oppervlak een tralie bestaande uit lijnen met een onderlinge afstand gelijk aan de periode van de staande golf. Echter de vorm van deze lijnen wordt bepaald door zowel de focuserings eigenschappen van de staande golf als door de oppervlakte groei processen.

In het tweede hoofdstuk hebben we eerst de focuserings eigenschappen van een staande laser golf als atoom-lens geanalyseerd met als doel de beperkingen van deze atoom-lens te achterhalen op laser gefocusseerde atoom depositie. Het algoritme dat is toegepast om het focuserings proces te modelleren is gebaseerd op een semi-klassieke benadering. De Newton-vergelijking voor de beweging van atomen in een optische potentiaal is numeriek opgelost om de klassieke atomaire banen te verkrijgen. De rol van de parameters van de laser- en atoom bundel is in detail onderzocht. Hieruit blijkt dat een goed gecollimeerde atoom bundel van essentieel belang is om een hoge resolutie, hoog contrast focusering te realiseren. Bovendien moet het laser vermogen zorgvuldig in overeenstemming met de experimentele geometrie en de laser frequentie verstemming (ten opzichte van de atomaire overgang) gebracht worden om de best haalbare resolutie te bereiken. Uit onze berekeningen blijkt dat het mogelijk zou moeten zijn een thermische bundel chroom atomen tot op 10 nm breedte te focuseren. Na het neerslaan van atomen op het substraat oppervlak verbreden de structuren echter aanzienlijk ten gevolge van oppervlakte diffusie en groei. Om een dieper inzicht te verkrijgen in de fysische processen die de vorm van een laser gefocusseerde nanostructuur beïnvloeden, hebben we vervolgens de groei van een dergelijke structuur gemodelleerd. Hierbij wordt gebruik gemaakt van drie verschillende atomaire modellen van adsorptie en diffusie van atomen op oppervlakken. Uit deze studie volgt dat theoretische voorspellingen van het profiel van de structuren sterk afhangen van het gebruikte model, de gekozen parameters binnen het model en de dikte van de chroom laag.

Op de ontwikkeling en bouw van onze apparatuur voor laser gestuurde atoom depositie is ingegaan in het derde hoofdstuk. Deze apparatuur bestaat uit twee hoofdonderdelen – het optische en het vacuüm gedeelte. We hebben een laser systeem (dat een enkele licht frequentie produceert) ontworpen en gebouwd voor de manipulatie

van chroom atomen op de ${}^7S_3 \rightarrow {}^7P_4^o$ ${}^{52}\text{Cr}$ overgang bij een golflengte van 425.55 nm. Dit systeem bestaat uit een titaan-gedoopte saffier laser welke infrarood licht rond 850 nm produceert. Deze infrarode laser bundel wordt vervolgens in frequentie verdubbeld in een externe resonator (die als een licht versterker werkt) door gebruik te maken van een optisch nietlineair kristal lithium tri-boraat (LBO). Het grootste uitgangsvermogen verkregen bij 425 nm was 550 mW, met een pompvermogen van 1.5 W/850 nm. Dit komt overeen met een conversie efficiëntie van bijna 37%. Tevens is er een golflengtemeter (gebaseerd op het principe van de Michelson interferometer) ontworpen en gebouwd. Het oplossend vermogen hiervan is 0.001 nm. Het bewegende gedeelte van deze golflengtemeter bestaat uit een nieuw soort luchtlagering, die speciaal ontworpen is om aan de strenge mechanische stabiliteitseisen te kunnen voldoen. De split-fotodiode techniek die toegepast is om de laser frequentie te koppelen aan de atoom resonantie is ook beschreven. Met behulp van deze techniek hebben we de laser frequentie binnen 0.5 MHz stabiel kunnen houden. In hetzelfde hoofdstuk zijn ook ons vacuüm systeem en de *in vacuo* optica (waarmee de sample houder verbonden is) en de manipulator beschreven.

In het vierde hoofdstuk hebben we een uitgebreide test van onze experimentele opstelling beschreven. Eerst is er een chroom bundel gecollimeerd tot 0.35 mrad met behulp van het eenvoudigste laser koeling mechanisme (gebaseerd op het Doppler effect). Vervolgens is het effect van een staande laser golf op de atomen waargenomen (ook “conservative channeling” genoemd). De frequentie van dit licht is 200 MHz verschoven boven de chroom overgang. Dergelijke gefocusseerde atomen zijn daarna neergeslagen op Si(100) en indium-tin-oxide (ITO) substraten gedurende ongeveer 20 minuten. De aldus gevormde nanostructuren bestaan uit een lijntjes patroon met een onderlinge afstand van 212.8 nm en bedekken een gebied van 1.5×0.4 mm. De breedte van de lijntjes bedraagt minimaal 75 nm bij een modulatie diepte (hoogte tussen pieken en dalen) tot 25 nm. Tenslotte wordt er verslag gedaan van de resultaten die verkregen zijn in samenwerking met de McClelland’s groep op het National Institute of Standards and Technology (in Gaithersburg, MD, USA), waarbij gebruik gemaakt is van hun experimentele opstelling. Om de rol van oppervlakte groei processen in laser gefocusseerde atoom depositie aan het licht te brengen, hebben we de evolutie van de chroom nanostructuren met toenemende dikte (oftewel toenemende depositie tijd) onderzocht. Alhoewel de verkregen resultaten laten zien dat de oppervlakte groei processen een doorslaggevende invloed hebben op de haalbare resolutie van deze techniek, wordt een uitgebreide kwantitatieve analyse helaas verhinderd door het relatief slechte vacuüm.

Ons toekomstige onderzoek zal zich om die reden richten op de groei van laser gefocusseerde nanostructuren in aanzienlijk betere (ultra-hoog) vacuüm condities. Dit zal het mogelijk maken om een breder inzicht te verkrijgen in de relevante processen en zodoende laser gefocusseerde nanofabricage tot aan de fundamentele grenzen te brengen.

Dankwoord

De volgende mensen hebben op een of andere manier aan mijn proefschrift bijgedragen.

Bijzondere dank gaat naar mijn collega's die zo diep bij het onderzoek beschreven in dit werk betrokken zijn geweest en die er onvervangbare wetenschappelijke en technische bijdrage aan hebben geleverd. Met name aan:

Albert van Etteger voor zijn ervaring en waardevolle kennis van optica;

Tonnie Toonen voor zijn enthousiasme en bekwaamheid in mechanica;

Jan Hermsen voor zijn diepe inzicht in vacuüm en bekwaamheid in mechanica;

Ran van Dongen en Peter Dolron voor hun bijdrage aan al de elektronische systemen waar zo veel gebruik van is gemaakt;

Jabez McClelland voor zijn ondersteuning en diepe inzicht in laser manipulatie van atomen die hij zo genereus aan mij wist over te dragen;

Curtis Bradley voor al die discussies over laser gefocusseerde nanofabricage;

Oleg Shklyarevskii voor zijn vruchtbare medewerking en geduld;

Andrei Petukhov voor zijn verbazingwekkend gevoel voor fysica;

Herman van Kempen, Theo Rasing en Leo Meerts voor de mogelijkheid en het vertrouwen dat ze aan mij hebben gegeven om aan een in Nijmegen volkomen nieuw onderwerp te werken.

Ook wil ik van deze gelegenheid gebruik maken om mijn dank te uiten aan:

Instrumentmakerij, met name aan **Ramon van Stijn**, voor de professionele uitvoering van al mijn mechanische wensen;

Riki Gommers, Wilma Vink en Marilou van Bremen die altijd zeer behulpzaam zijn geweest;

Julius Hohlfeld, Aidan Quinn, Anthony Keen, Klaas Jelle Veenstra, Maarten Bischoff, Olaf Gielkens, Niels van Wijk en Florian Bentivegna voor hun enthousiasme en discussies niet alleen over fysica.

Vanzelfsprekend gaat mijn grootste dank uit naar **mijn moeder, oma, Zuzana, Edith en Jenny** die altijd heel dichtbij mij staan en die ontzettend veel geduld met mij hebben.

Erich Jurdík,

Nijmegen, maart 2001

Curriculum vitae

Erich Jurdík
geboren op 13 april 1974
in Bratislava, Tsjechoslowakije

1988-1992	Metodova Gymnasium te Bratislava.
1992-1996	Studie natuurkunde aan de Comenius Universiteit te Bratislava. 'Master of Science' diploma. Afstudeeronderwerp: 'Electron transport in solids for quantitative surface analysis.'
1994-1997	Studie technische natuurkunde aan de Technische Universiteit te Wenen, Oostenrijk.
1997-2001	In dienst van de Stichting FOM als Onderzoeker in Opleiding. Promotiewerk aan de Katholieke Universiteit Nijmegen, in de Vakgroep Experimentele Vaste-Stoffysica 2 onder leiding van Prof. dr. H. van Kempen en Prof. dr. Th. Rasing.
juni-augustus 1998	Guest researcher op het National Institute of Standards and Technology in Gaithersburg, Maryland, USA.
juni-augustus 2000	Guest researcher op het National Institute of Standards and Technology in Gaithersburg, Maryland, USA.